2018

Spin Transport in Silicon Nanowires with an Intrinsic Axial Doping Gradient

Konstantinos Kountouriotis

FLORIDA STATE UNIVERSITY

COLLEGE OF ARTS AND SCIENCES

SPIN TRANSPORT

IN SILICON NANOWIRES WITH AN INTRINSIC AXIAL DOPING GRADIENT

By

KONSTANTINOS KOUNTOURIOTIS

A Dissertation submitted to the
Department of Physics
in partial fulfillment of the
requirements for the degree of
Doctor of Philosophy

2018

Konstantinos Kountouriotis defended this dissertation on May 23, 2018.
The members of the supervisory committee were:

Peng Xiong

Professor Directing Dissertation

Steven Lenhert

University Representative

Stephen Hill

Committee Member

Volker Crede

Committee Member

Pedro Schlottmann

Committee Member

The Graduate School has verified and approved the above-named committee members, and certifies that the dissertation has been approved in accordance with university requirements.

ACKNOWLEDGMENTS

I would like to thank a lot of people for the continuous support during my PhD career, to whom I offer my deepest, and sincerest gratitude. First, I want to thank my advisor, Professor Peng Xiong, for the incredible opportunity, patience, and guidance, that helped me progress to an independent researcher. His valuable advice, insight, and positive criticism was keeping me on track at all times.

I would also like to thank Professor Stephan von Molnàr, who acted as a co-advisor, and was always available to discuss my research challenges, and was always supportive. I want to express my gratitude to Professor David Van Winkle, and to many research groups which have offered collaborations for the projects in which I participated, Professor Jianhua Zhao, Professor Mei Zhang, and Professor Biwu Ma.

I am also grateful to my group members and friends, who have been very helpful and have provided guidance, as well as their expertise throughout my graduate studies. Dr. Jennifer Misuraca, Dr. Gratiela Stoian, Dr. Liuqi Yu, Dr. Joon-Il Kim, Dr. Dong Pan, Dr. Tim Keiper, Dr. Jorge Barreda, Dr. Longqian Hu, Danielle Simmons, Tianhan Liu, Jacob Hudis and Terence Fisher.

Progress on my experiments would have been limited without the support from the technical staff in the Physics department during my graduate career. A lot of people helped me overcome unexpected equipment issues and improve my technical skills. I owe my sincere gratitude to Dr. Eric Lochner, Kurt Koetz, Jim Valentine, Bob Smith, Ian Winger, Randall Smith and Joe Ryan.

Last but not least, I want to deeply thank my family and friends in Greece. Their support throughout my journey in the United States has been indescribable, and has definitely contributed to my effort in completing my PhD.

TABLE OF CONTENTS

LIST OF TABLES

LIST OF FIGURES

ABSTRACT

This dissertation is focused on electrical spin injection and detection at nanoscale dimensions that semiconductor nanowires offer. Semiconductor spintronics is the natural extension of metallic spintronics for applications in semiconductor industry. After the tremendous impact of the giant magnetoresistance effect (GMR) in hard disk read heads, semiconductor spintronics has been thought as the key ingredient for the realization of spin field-effect transistors (Spin-FETs). The advantages of spintronic devices would include non-volatility, enhanced data processing speeds, decreased electric power consumption and possible facilitation of quantum computation.

The primary goal of this research is to study spin dynamics and spin-polarized transport in semiconductor nanowire (NW) channels, specifically in phosphorus (P) doped silicon (Si) nanowires (NWs). The interest in one-dimensional (1D) nanoscopic devices is driven by the rich spin-dependent physics quantum confinement engenders, and the eventual miniaturization of the spintronic devices down to nanoscales. One of the most important aspects to achieve efficient spin injection from a ferromagnet (FM) into a semiconductor (SC) is the interface between the two materials. This study is focused primarily on this effect at nanoscale and how it can be tuned.

In this work, we peform systematic spin transport measurements on a unique type of P-doped Si NWs which exhibit an inherent doping gradient along the axial direction. On a single NW, we place a series of FM electrodes, which form contacts that evolve from Ohmic-like to Schottky barriers of increasing heights and widths due to the pronounced doping gradient. This facilitates rigorous investigation of the dependence of the spin signal on the nature of the FM/SC interface. The advantage of using a single NW to study the afformentioned effects is that possible complications during the fabrication process are minimized compared to experiments that use multiple different devices to perform such experiments.

2-terminal (2T), nonlocal 4-terminal (4T) and 3-terminal (3T) spin valve (SV) measurements using different combinations of FM electrodes on the same Si NWs were performed. In addition, 3T and nonlocal 4T Hanle measurements were attempted. Distinct correlations between the spin signals and the injector and detector interfacial properties are evident in the collected data. These results were possible due to the unique inhomogeneous doping profile of our Si NWs.

The most notable result of this study is a distinct correlation revealed in the spin valve measurements between the spin signals and the FM/Si NW injector interfacial properties. Specifically, we observe a decreasing injected current spin polarization due to diminishing contribution of the d-electrons. The necessary tunneling contact for efficient spin injection and its properties are being investigated and analyzed. The results demonstrate that there is an optimal window of interface resistance parameters for maximum injected current spin polarization. In addition, they suggest a new approach for maximizing the spin signals by making devices with asymmetric interfaces. To the best of our knowledge, this is the first report of electrical spin injection in SC channels with asymmetric interfaces.

CHAPTER 1

INTRODUCTION

The field of microelectronics, which has been a branch of physics and later on of electrical engineering, has arguably led to the most important technological breakthroughs in today's society. Who cannot appreciate the importance and advantages of personal electronic devices, and how much they have influenced our everyday lives in every aspect (science, education, medicine, economics, etc.)? Historically, electronics began to evolve in the late 19th century when the English physicist Sir Joseph John Thomson identified the existence of the electron and the American physicist Robert A. Millikan succesfully measured its electric charge in 1909.

A few decades later, there was a tremendous breakthrough which revolutionized the field of electronics and provided the most important building block of the semiconductor industry. That was the invention of the point-contact transistor by John Bardeen, Walter Brattain, and William Shockley at Bell Labs in 1947 [1, 2] who shared the Nobel prize in physics in 1956. The transistor paved the way for smaller devices that can be used to manipulate electrical signals. Transistors are semiconductor devices which have electrical properties that can be varied over a wide range by the addition of minuscule quantities of other elements ("doping").

Another breakthrough in electronics was the invention of the integrated circuit by Jack Kilbly at Texas Instruments in 1958 [3]. Jack Kilbly was awarded the Nobel prize in physics for this discovery in 2000. This invention was a method of integrating large number of electronic circuits on one small flat piece ("chip") of semiconductor material, and it was the begining of the miniaturization of electronic devices.

A more recent invention in 1960, which has become the foundation of charge-based electronic devices, is the field-effect-transistor (FET) [4]. It was followed by the complimentary metal-oxide-semiconductor (CMOS) technology, for constructing integrated circuits [5]. The FET is a transistor that uses an electric field to modulate the electrical behavior of the conducting channel, where electrons and/or holes flow. Figure 1.1 shows examples of a traditional planar FET and a modern 3D tri-gate FinFET. An example of the CMOS logic circuit is the typical design of a CMOS inverter,

which is a device that combines pairs of p-type and n-type metal oxide semiconductor field effect transistors (MOSFETs) for logic functions. These innovations set the stage for the ongoing effects to produce even smaller chips with higher density of such electronic elements.

Indeed, as Gordon Moore predicted in 1965, the number of transistors in a dense integrated circuit follows an exponential growth with time, doubling approximately every 2 years [6]. Figure 1.2 depicts the Moore's law graph from 1971 to 2011. This trend has continued over the past few decades, but in the past decade there have been persistent and growing concerns about the indefinite continuation of Moore's law as we move towards the sub 10 nm scales. If Moore's law is to come to an end, then new approaches are needed for future development of electronics. One possible solution is to utilize spin-based electronics, potentially a new paradigm for microelectronics. Spin-based technology is possible due to another scientific breakthrough of the 20th century, **quantum mechanics**, and the existence of an intrinsic degree of freedom of electrons, called **spin**.

The emergence of quantum mechanics brought significant changes on how we interpret physical systems in the microscopic limits, and semiconductor systems are no different. One of the most important discoveries was the fact that elementary particles have an intrisic property called angular momentum, or "spin", and associated with this a magnetic moment. Wolfgang Pauli was the first to propose this idea. Electrons are elementary particles with spin $S = 1/2$. The main focus of this dissertation is in the area of "spintronics". Spintronics is an important field of research with broad potential applications in emerging technologies. The basic concept of spintronics is the manipulation of spin polarized currents, in contrast to conventional electronics where the spin degree of freedom of the electron is ignored. Devices utilizing both the electron charge and the spin degree of freedom of electrons could have novel functionalities and offer solutions to some of the fundamental shortcomings of conventional microelectronics.

The continuous miniaturization of the devices have a physical limit, which is governed by the quantum mechanical nature of particles, and in the nanoscale dimensions can alter the behavior of functional devices in remarkable ways. Of course, taking advantage of the quantum mechanical properties can lead to new fascinating technologies, which is the main purpose of today's nanotechnology research. Quantum effects become apparent when the sample size, grain size, or domain size becomes comparable with a specific physical length scale such as the electron mean free path, coherence length of phonons, etc.

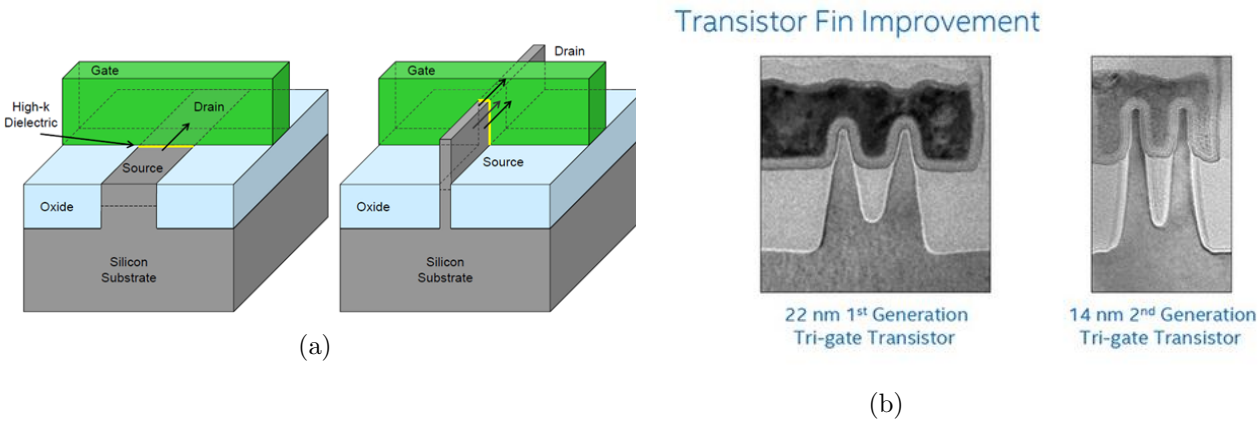

Figure 1.1: (a) Traditional planar FET (left) and modern 3D FinFET tri-gate (right). (b) 22 nm 1^{st} generation and 14 nm 2^{nd} generation tri-gate transistor from Intel.

Nanotechnology emerges from the exploitation of new physical properties, phenomena, processes and functionalities that matter exhibits at sizes between 1 $nm - 100$ nm. Almost all the properties of a physical system are affected by quantum effects, including thermodynamic, electrical, magnetic, mechanical, optical and transport properties. Research on semiconductors and magnetic materials (thin-films) at the nanoscale are experiencing astonishing growth with significant impact on new technologies. Spin devices are examples of such applications and they can be realized in bulk semiconductors [7, 8, 9, 10, 11], two-dimensional (2D) electron systems [12, 13, 14, 15, 16] and in one-dimensional (1D) or quasi 1D dimensional nanowires [17, 18, 19, 20, 21, 22].

This dissertation is focused on electrical spin transport experiments in phosphorus-doped (P-doped) Si NWs which exhibit an inherent axial doping gradient along the axial direction. The uniqueness of this system is that there is a variation in the doping profile mostly on the surface of the NW along the axial direction, which enables the formation of contacts that evolve from Ohmic-like to Schottky barriers of increasing heights and widths along the length of the NWs. The ferromagnet/semiconductor (FM/SC) interface plays a most important role for realizing efficient spin injection between a FM and a SC as it has been demonstrated both theoretically [23, 24] and experimentally [10, 11, 14]. The realization of evolving contacts *on a single NW* facilitates a reliable and thorough study of the dependence of spin injection on the FM/SC interfacial properties, while avoiding complications associated with using different samples that have different growth parameters. For example, in devices which utilize oxide tunnel barriers as contacts (FM/oxide/SC),

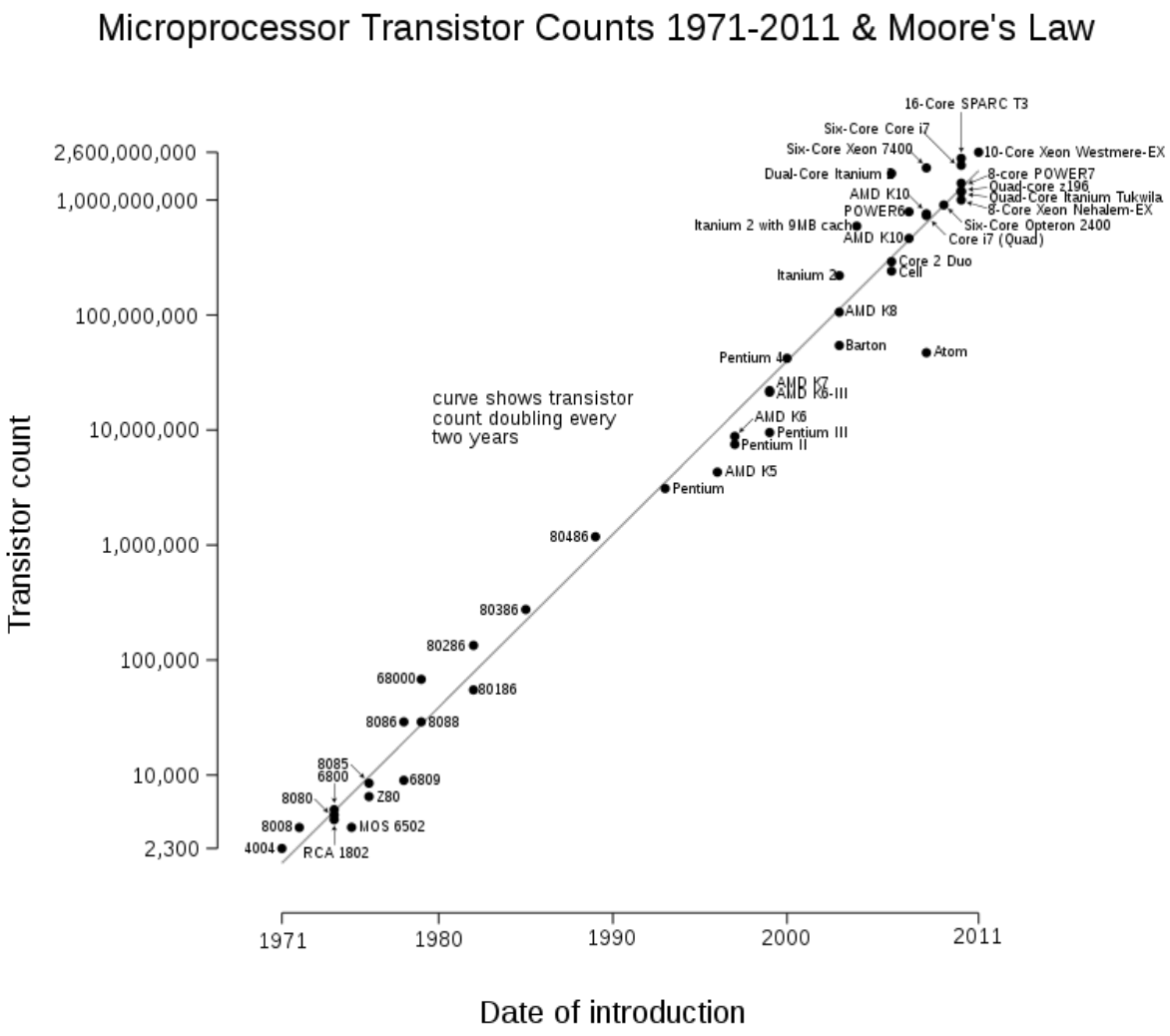

Figure 1.2: A plot of CPU transistor counts versus dates of introduction, showing the exponential growth with transistor count doubling every two years. Source: wikipedia/Transistor count.

different growth parameters can lead to different location and density of localized states, which can significantly affect the spin signals and render the analysis more complex [25, 26, 17]. In this work, spin measurements were performed in the local two-terminal (2T), nonlocal four-terminal (4T), and local three-terminal (3T) lateral spin valve configurations at 5 K [27, 28]. Hanle effect measurements were also attempted [11]. A distinct correlation between the FM/Si NW junction

resistance of the injector electrode and the spin polarization of the current was revealed. This correlation is associated with the differently and oppositely spin polarization of the $3d$ and $4sp$ electron states, both of which are contributing to the total spin polarization of the current.

This thesis is organized as follows. Chapter 2 will focus on the basic concepts of semiconductor and metallic spintronics and the main motivation of this research, which is spin transport in Si nanowires with axial doping gradient. In Chapter 3, the experimental methods and techniques for the spin transport experiments will be described in detail. Chapter 4 is dedicated to the electrical characterization, and the spin transport results in Si NWs with axial doping gradient. Finally, in Chapter 5 the thesis and the main experimental results will be briefly summarized.

CHAPTER 2

SPINTRONICS

2.1 Introduction

2.1.1 Origin and Motivation of Spintronics

The past few decades of research and development in solid-state semiconductor physics and microelectronics have witnessed rapid development and evolution of semiconductor devices. Despite the focus on miniaturization of semiconductor devices toward nanoscale, a principal quantum mechanical property of the electron had been neglected for electronic applications. This property is the spin degree of freedom of electrons. Spin is an intrinsic fundamental property of electrons. It has long been the basis for storing information, but underused for processing information. Spintronics is an area of research that studies the spin degree of freedom of electrons and how it can be utilized in electrical transport or optical devices. The main goal is to encode and process information not only by using the electron's charge degree of freedom, but at the same time its spin state. The advantages of spintronic devices would include non-volatility, faster intrinsic switching speeds, enhanced data processing speed, decreased electric power consumption, and possibly facilitation of quantum computation.

The electron spin states offer the opportunity to store and manipulate phase coherent spin states over space and time. Modern spintronics originated from the discovery of giant magnetoresistance effect (GMR) by Fert and Grünberg in 1988 [29, 30]. This discovery produced highly sensitive magnetic sensors, which today are the major components in the read heads of magnetic hard disks. In today's technology we can already appreciate the dramatic increase in the density of data that can be stored per square inch on a magnetic disk, which has approached 1.2 TB/in^2 by using materials with perpendicular magnetic anisotropy (PMA).

In 1990 Datta and Das proposed a spin modulator device which can be thought as a spin field-effect transistor [31]. This type of device could be used as a spin based logic device by changing its resistance state from high to low by manipulating the electron spin states via an externally applied electric field (electric gate). A schematic of such a device is shown in Figure 2.1(a). This is possible

in materials, such as 2DEGs in narrow-gap semiconductors, where the spin-orbit interaction gives rise to the Rashba term in the effective Hamiltonian, and acts as an effective momentum dependent magnetic field. Ferromagnetic contacts are used to preferentially inject and detect spins of a specific orientation, and the Rashba field induces coherent spin precession. The strength of the Rashba field (spin-orbit coefficient) can be tuned by the external electric field. A more straightforward scheme for such a device is the spin metal-oxide-silicon field-effect transistor (spin MOSFET) proposed by Sugahara and Tanaka in 2005 [32]. This device would act as a spin valve while being a conventional FET.

Moreover, the spintronic logic devices rely on spin coherence in semiconductor structures, hence optimization of electron spin lifetimes, transport of spin-polarized carriers across relevant length scales and hetero-interfaces, and the manipulation of both electron and nuclear spins on sufficiently fast time scales. In a broad sense, spintronics is a study of spin-dependent phenomena in solids, in particular metals, semiconductors and semiconductor heterostructures. The main focus of such studies is to characterize electrical, optical, and magnetic properties of materials due to the presence of equilibrium and nonequilibrium spin populations, and the corresponding spin dynamics. Such studies provide important insights about the nature of spin-dependent interactions, such as spin-orbit coupling, hyperfine interaction, and spin exchange coupling in solids. They also promote further understanding of the microscopic processes responsible for spin relaxation and spin dephasing, microscopic mechanisms of magnetic long-range order in semiconductor systems, topological aspects of mesoscopic spin-polarized current flow in low-dimensional semiconductor systems, and the important role of the electronic band structure in spin-polarized tunneling.

For example, there are two interesting and important experimental discoveries in the field of spintronics: (1) The (direct) spin Hall effect, which was proposed by D'yakonov and Perel (1971) [33], who suggested that passing an electrical current through a conductor will result in a spin accumulation at the edges of the conductor transverse to the current flow, due to asymmetric spin-dependent scattering of impurities (Mott scattering) even in the absence of an applied magnetic field. The effect is illustrated in Figure 2.1(b). The experimental discovery was reported by Kato in 2004 [34], and Wunderlich in 2005 [35]. Due to similar arguments, an inverse effect exists in which a pure spin current passing through a channel is converted into an electrical voltage in the transverse direction [33]. (2) The spin galvanic effect, where a spin-polarized electron gas can drive an electrical

current without the need of an external electric field. This effect was reported by Ganichev in 2001 [36]. Microscopically, this effect originates in systems where the spin-orbit interaction lifts the degeneracy for the spin-up and spin-down subbands in momentum space, and due to an inherent asymmetry in the spin-flip scattering events between the two subbands, an electrical current flows along the scattered direction. A schematic representation of the microscopic picture is shown in Figure 2.1(c).

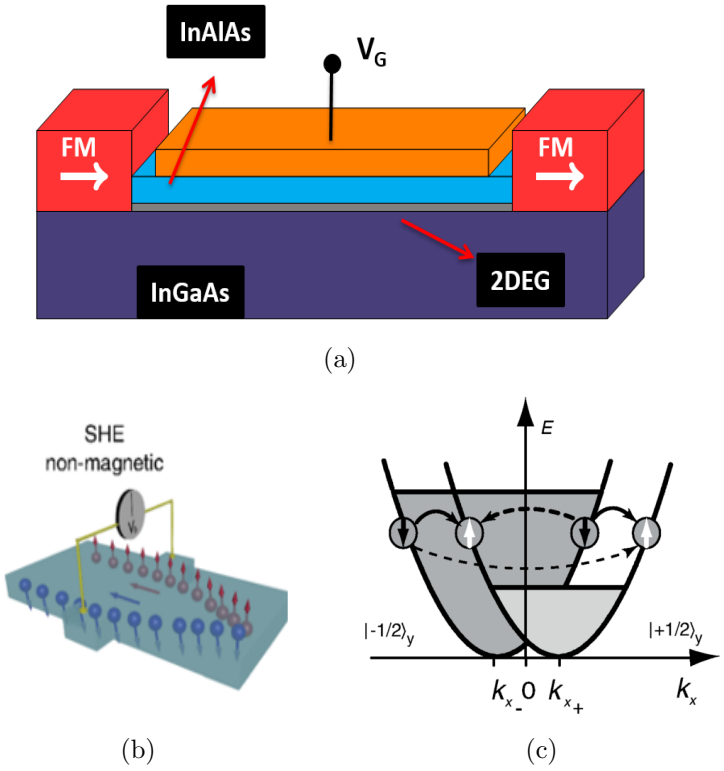

Figure 2.1: (a) Schematic of the spin modulator device proposed by Datta and Das. Adapted from reference [31]. (b) An illustration of the spin Hall effect, an unpolarized longitudinal charge current generates a transverse pure spin current [37]. (c) Illustration of the microscopic origin of the spin galvanic effect. When one spin subband has a higher occupation number, asymmetric spin-flip scattering results in a current along that direction [38].

2.1.2 Semiconductor Spintronics

While metal-based spintronics have already been used in computer industry (e.g., as hard disk read heads), semiconductor spintronics is yet to demonstrate its full potential. Semiconductors have the following advantages for making spintronic devices which are inaccessible to metal-based

spintronic structures: i) the mean-free path is long which leads to long coherence length, ii) the density of carriers is relatively small so that the behavior can be looked as that of a single particle, iii) the quality of semiconductor single crystals can be made to be almost perfect, iv) the band gap can be tuned over a significant range, v) the carrier concetrations and transport characteristics can be readily controlled via doping, gate voltages, and band offsets, vi) semiconductor device technology is mature and the process of making integrated devices well established.

The essential requirements for realizing spin-based semiconductor devices are the following:

1. Efficient electrical injection of spin-polarized current from a spin-polarized material into a semiconductor channel.
2. Relatively long spin diffusion lengths and spin lifetimes within the semiconductor material.
3. Sufficient control and manipulation of the spin ensemble to achieve the desired functionality.
4. Efficient electrical detection of the spin-polarized current (output of the system).

A straightforward way to efficiently inject spin polarized carriers into a semiconductor channel is the use of "diluted ferromagnetic semiconductors" as spin injectors. Indeed, a lot of spin transport experiments have been conducted by using compounds such as GaMnAs [39, 40]. Ferromagnetic semiconductors are ideal materials for spin transport experiments because their spin polarization can be as high as 90% and the conductivities are similar to those of conventional doped semiconductors. The biggest disadvantage of this approach is that the Curie temperatures can only go as high as 200K which is not adequate for everyday electronic applications. Raising the Curie temperature for dilute magnetic semiconductors is an active research topic.

Nevertheless, hybrid structures of a conventional FM metal can be used for efficient spin injection into a semiconductor despite the so-called "conductivity mismatch" problem, which will be addressed in more detail in the upcoming sections. Ferromagnetic transition metals offer reasonable spin polarizations at the Fermi level E_F, around $\sim 30\% - 40\%$ [41]. Some of the advantages of such hybrid structures include high Curie temperatures, low coercive fields, and fast magnetization switching. Also, molecular beam epitaxy (MBE) techniques produce atomically sharp FM/SC interfaces. In addition, a FM contact supports nonvolatile operation due to the intrinsic magnetic anisotropy, and a FM metallization process could be easily incorporated in existing processing protocols currently used by the semiconductor industry.

2.2 Spin Injection Theory

The first question we have to answer is what do we mean by spin injection and spin current propagation, and how we can mathematically describe such effects. The most intuitive way of thinking about spin currents would be to try making an analogy with materials that have a spontaneous magnetization, such as ferromagnetic materials. One important quantity for the description of such phenomena, is the spin polarization. Spin polarization is defined as [41]

$$P = \frac{N_{\uparrow}(E_F) - N_{\downarrow}(E_F)}{N_{\uparrow}(E_F) + N_{\downarrow}(E_F)} \tag{2.1}$$

where $N_{\uparrow}(E_F)$ and $N_{\downarrow}(E_F)$ are the density of majority and minority spins at the Fermi level. It can also be described as the difference between the density of states of the two spin subbands, in which case it is called density spin polarization. Similarly, because the current is proportional to the density of states, and in general spin is conserved (when spin-orbit coupling and spin-flip scattering are negligible) we can define the current spin polarization as

$$P_j = \frac{j_{\uparrow} - j_{\downarrow}}{j_{\uparrow} + j_{\downarrow}} = \frac{j_s}{j} \tag{2.2}$$

Many materials in their FM state have a pronouced spin polarization ($\sim 30-40\%$), and for half-metals (e.g. CrO_2) it can be 100%. In these materials, as it was explained by Mott (1936) [42], the conductivity can be expressed as the superposition of two independent and unequal parts for the two different spin projections, and their relation stays fixed during electrical transport. That means that most scattering events do not result in a spin flip inside the polarized material. However, having an intrinsic spin polarization is not a sufficient condition for spintronic applications by itself, often the generation and manipulation of a nonequilibrium spin population in a nonmagnetic material is needed. In most materials the spin subbands are equally occupied, and as a result the spin polarization is zero. For spintronic applications both types of materials are used. When two disimilar materials are brought in contact, one with and one without spin polarization, and a current flow is maintained, a state of *nonequilibrium* spin polarization is created at the interface. This happens because the current of electrons is spin polarized inside the FM conductor and nonpolarized inside the nonmagnetic conductor (N)/semiconductor. At the interface, there must be a transfer of current between the spin up channel to the spin down channel due to the nonequilibrium state. Eventually, after the process of spin flips, a steady state is reached to balance the ingoing

and outgoing spin fluxes. It is this state of *nonequilibrium spin polarization*, also called *spin accumulation*, that drives much of the field of spintronics, and specifically how it flows/decays and how it can be manipulated. Due to spin diffusion, the spin accumulation is not localized at the interface but extends to both sides within a specific characteristic length, which is material dependent. The characteristic length is defined as the spin diffusion length, λ_N, and the associated time is called the spin diffusion time τ_s. The relation between these two quantities is $\lambda_N = \sqrt{D_s \tau_s}$, where D_s is the spin diffusion constant. Nonequilibrium spin polarization can result from electrical transport [11][10], optical pumping [43, 44], or resonance [45].

The ultimate goal during the process of spin injection would be to coherently manipulate and control the injected spins. An external magnetic field is the most direct way to achieve such control, by inducing spin precession. Spin-orbit coupling, as it will be discussed in the following sections, can also induce an effective magnetic field, and provide a different way of spin manipulation. The transfer of phase coherent spins for long distances and times, which can be used in transferring and processing information, is the main purpose of studying spin injection and spin relaxation processes.

As mentioned earlier, the topic of spin injection became an active area of research after the discovery of GMR by Albert Fert's group [29] and independently by Peter Grünberg's group [30] in 1988. This effect involves heterostructures made out of alternating ferromagnetic and nonmagnetic materials. One magnetic layer is free to be magnetized in different directions, while the other one can be free or have its magnetization pinned to one direction. Upon switching the relative orientation between parallel and antiparallel, there is a change from a low resistance state to a high resistance state. Specifically, when the layers have parallel magnetizations, spin dependent scattering is minimized for one of the two spin subbands, whereas when the layers are in the antiparallel configuration, spin dependent scattering is maximized for both spin subbands. This structure allows the realization of low resistance and high resistance states. A schematic representation is shown in Figure 2.2. Sandwich structures of Fe/Cr/Fe by Grünberg's group produced a GMR effect around 10% at 5 K [46], but in that case neither of the two FM layers was pinned. Dieny's spin valve devices, with one pinned layer, produced a GMR of 5% at room temperature [47]. The GMR effect lead to the production of computer disk drives with smaller dimensions and much larger storage densities (Dieny, *et al* at IBM 1992 [48]). In 1994, another breakthrough occured with the discovery

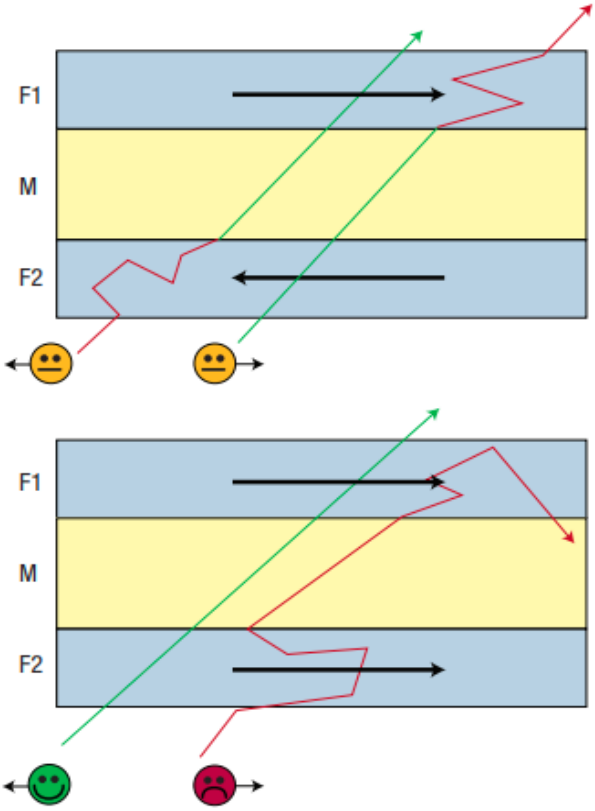

Figure 2.2: Schematic representation of the spin valve GMR effect. When the two magnetic layers are magnetized in the same direction, the spins of one of the subbands can travel through the nonmagnetic layer nearly unscattered, resulting in a low resistance state. In the case that the two magnetic layers are magnetized in opposite directions, both spin directions undergo collisions, resulting in a high resistance state. Figure is adapted from Chappert [52].

of tunnel magnetoresistance (TMR) [49] [50], where the intermediate layer was replaced with an insulating layer, and that significantly increased the magnetoresistance ratio even up to 220% [51].

The GMR and TMR effects manifest in large values of magnetoresistance due to spin dependent scattering at the interface, rather than spin manipulation, and are called "non-coherent". New possible functionalities arising from injecting, controlling, and detecting spin coherent states is the main focus of semiconductor spintronics. Although, the first spin transport experiments were done in metallic systems, the theoretical models proposed are generic.

Nonequilibrium spin accumulation in metals was first measured by Johnson and Silsbee in permalloy/aluminum structures in 1985 [53, 54]. These spin injection experiments provided direct proof that a spin polarized current crossing an FM/N interface would stay polarized for some

distance, which was theoretically proposed by Aronov [55]. In addition, Silsbee predicted that the nonequilibrium spin population (spin accumulation) would diffuse in the channel with a specific characteristic spin diffusion length, and generate an electric voltage at a different FM/N interface in the channel. They suggested that the amplitude and sign of the voltage would depend on the relative orientation of the magnetizations of the two FM, $F1$ and $F2$. This experiment was the first to demonstrate an electrical signal modulation with respect to magetization orientation in FM/N/FM structures, and set the foundations for the "nonlocal spin transport" experiments that are performed until today. In nonlocal spin transport measurements, the measured signal is a result of the spin accumulation diffusing in the channel isotropically from the injection point, and there is no contribution from the charge current. It is a more reliable experimental way of extracting spin information without having contributions from spurious effects such as the magneto-Coulomb effect [56], local Hall effects [57], and anisotropic magnetoresistance effects that can result in similar resistance modulation. In addition, Johnson and Silsbee showed the modulation of the spins by the Hanle effect, which is presented in greater detail later in this thesis, proving that the magnetoresistance signal is indeed a pure spin signal. The same type of experiments were realized in a SC in 2007, specifically in GaAs [11].

Here Johnson's pedagogical three-terminal geometry that describes the spin injection process is presented. A schematic representation of such a device, along with simplified density of states diagrams (using half-metal FM) that describe the transport model of spin injection, spin accumulation, and spin detection are shown in Figure 2.3. When a current is driven from one ferromagnetic electrode $F1$ into a nonmagnetic layer N a fraction of the FM's magnetization is also transfered. The spin polarized current can be expressed as [58]:

$$I_M = \frac{g_\uparrow - g_\downarrow}{g_\uparrow + g_\downarrow} \frac{\mu_B I}{e} \tag{2.3}$$

where μ_B is the Bohr magneton, and $g_\uparrow$, $g_\downarrow$ are the up and down spin subband conductances. It is worth mentioning that this corresponds to a one-dimensional model. In principle the spin polarized current is described by a second rank tensor, because there are three parameters for the spatial coordinate and three projections for the spin. Within the nonmagnetic region N of thickness $d < \lambda_N = \sqrt{D_s \tau_s}$, and volume $V = Ad$, the nonequilibrium magnetization (spin accumulation) is:

$$\tilde{M} = \frac{I_M \tau_s}{V} \sim N(E_F)(E_{F,N\uparrow} - E_{F,N\downarrow}) \tag{2.4}$$

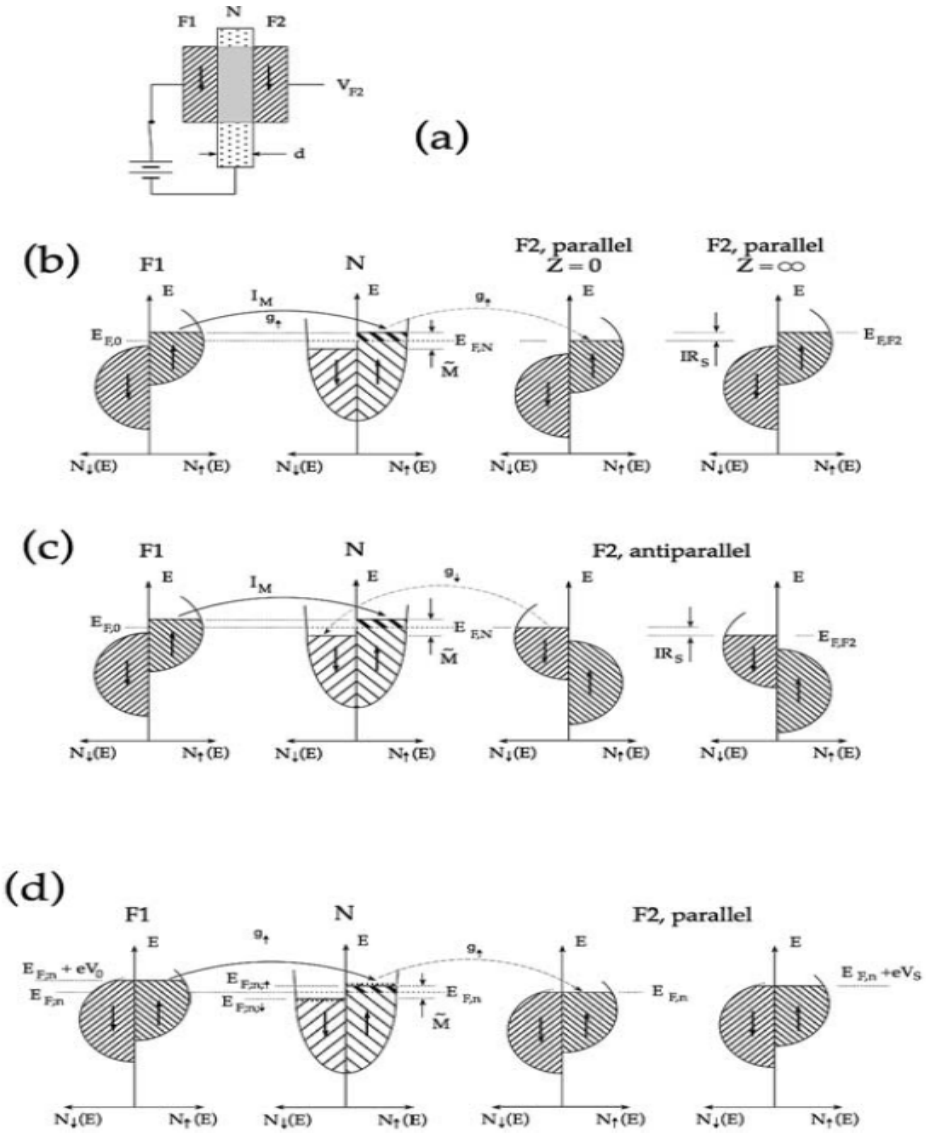

Figure 2.3: (a) Sketch of a three-terminal device for spin injection and nonlocal detection. (b)-(d) Schematic density of states diagrams that describe the transport model for spin injection, accumulation, and detection for both cases of parallel and antiparallel magnetization, as well as zero and infinite impedance of $F1$ and $F2$. Figure adapted from Dyakonov [58].

A second FM $F2$ acts as the spin detector. When $F2$ is connected to ground through a low impedance current meter, a spin polarized current is passing through the interface due to the induced spin splitting in the channel. This current is bipolar, and the sign depends on the relative orientation of the magnetizations of the two FMs. Looking at the density of states diagrams,

the detector Fermi level will line up with the channel spin up or down subband depending on its magnetization state. The current is positive $I_d \sim N(E_F)(E_{F,N\uparrow} - E_{F,N})$ when both FMs have their magnetizations parallel to each other, and negative $I_d \sim N(E_F)(E_{F,N} - E_{F,N\downarrow})$ in the antiparallel configuration. Experimentally, it is customary to connect $F2$ with a high impedance voltmeter, and measure the electromotive force (*emf*) that drives the electric current (Silsbee-Johnson spin-charge coupling). Similarly, the *emf* voltage, also called an open-circuit voltage, is bipolar

$$V_{F2} = V_s = \pm \frac{\eta_2 \mu_B}{e} \frac{\tilde{M}}{\chi} \tag{2.5}$$

where η_2 is the spin polarization of $F2$, and $\mu_B \tilde{M}/\chi$ is the effective Zeeman energy of a spin-polarized electron in the presence of the effective field of all the others nonequilibrium spins, and χ is the susceptibility. Combining equations 2.3, 2.4, and 2.5 yield the expression for the transresistance [59]:

$$R_s = \frac{\eta_1 \eta_2}{\chi} \frac{\mu_B^2}{e^2} \frac{\tau_s}{V} = \eta_1 \eta_2 \frac{\rho L_s^2}{V} \tag{2.6}$$

where a free-electron expression for susceptibility, $\chi = \mu_B^2 N(E_F) = \mu_B^2 3n/2E_F$, and the general form of Einstein's relation for the resistivity $\rho = 1/(e^2 D(\partial n/\partial \mu)) \approx 1/(e^2 D(3n/2E_F))$, where μ is the chemical potential, have been used. Experimentally, the open circuit transresistance is measured between the parallel and antiparallel configurations, which gives the magnetoresistance signal $\Delta R_s = R_{\uparrow\uparrow} - R_{\uparrow\downarrow} = 2R_s$. In the case where the channel is longer than the spin diffusion length, $d \gg \lambda_N$ the spin accumulation decays exponentially away from the $F1/N$ interface, and the equation becomes:

$$R_s = \eta_1 \eta_2 \frac{\rho \lambda_N^2}{V} e^{-d/\lambda_N} \tag{2.7}$$

It is worth mentioning a few distinct differences between the spin accumulation and the GMR signals; the latter are associated with spin dependent interfacial scattering. First, the detected signals due to the spin accumulation can be truly negative, for the antiparallel configuration, whereas GMR signals are always positive, and only the magnitude is modulated. Second, the spin accumulation signals can be destroyed in the presence of an external magnetic field applied perpendicular to the plane of the spin polarization (Hanle effect). Lastly, the spin accumulation signals are inversely proportional to the volume of the channel, which is an important motivation for fabricating devices with nanoscale dimensions.

2.3 Spin Drift-Diffusion Model

In this section, the drift-diffusion model that describes the motion of spin-polarized electrons in the presence of a magnetic field is briefly described. This model is what defines spin transport within a channel. The spin drift-diffusion model is an extension of the random walk motion that describes drift-diffusive transport of electrons in a disordered solid, in the presence of an electric field. The difference is that the system is composed of electron spins in the presence of an external magnetic field. The equation describing a spin undergoing precession is:

$$\frac{ds}{dt} = s \times \omega \tag{2.8}$$

where $\omega = g\mu_B B/\hbar$ is the Larmor frequency. After some time of precession τ, where $\tau \ll 1/\omega$, the equation that describes the evolution of the spin is:

$$s(t+\tau) = s(t) + s(t) \times \omega\tau. \tag{2.9}$$

The product of the Larmor frequency and the time of precession τ gives the phase change of a precessing spin. Considering a random walk motion, with step size l over a time step τ, predicts that the spin at some point x at time $t+\tau$ will be given by

$$s(x,t+\tau) = P_+ \left[s(x-l,t) + s(x-l,t) \times \omega\tau - s(x-l,t)\frac{\tau}{\tau_s} \right] \tag{2.10}$$

$$+P_- \left[s(x+l,t) + s(x+l,t) \times \omega\tau - s(x+l,t)\frac{\tau}{\tau_s} \right], \tag{2.11}$$

This equation is the total spin at point x due to the spins at positions $x+l$ and $x-l$, at time t, each rotated about ω over the time step τ and decreased by the fraction of τ/τ_S due to spin relaxation. The probabilities for an electron to jump right or left are P_+ and P_- respectively (see Figure 2.4). Taylor expanding the left-hand side around t, and the right hand side around x gives the drift-diffusion equation for spin dynamics,

$$\frac{\partial s}{\partial t} = s \times \omega + D_s \nabla^2 s + \mu E \nabla s - \frac{s - s_0}{\tau_s}. \tag{2.12}$$

The terms on the right-hand side of the equation describe spin precession, spin diffusion, spin drift, and spin relaxation respectively. In addition, the generalized spin current is $J_s = -\mu E s - D_s \nabla s$, and the continuity equation takes the form

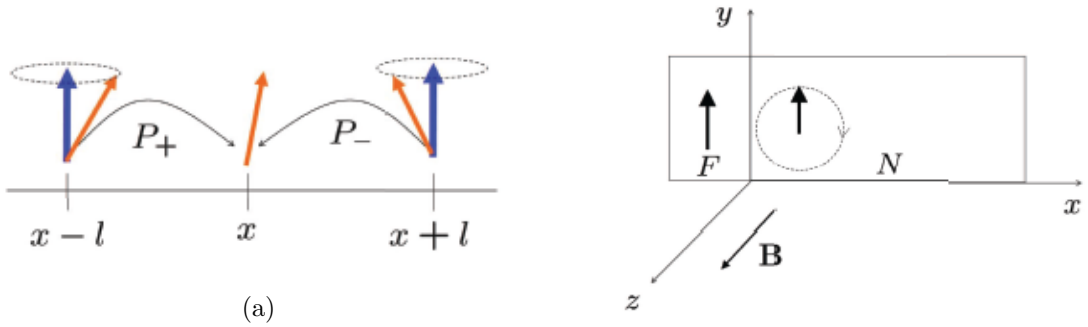

(a) (b)

Figure 2.4: (a) Spin precession and random walk. (b) Spin injection and precession geometry. An applied magnetic field in the z direction causes spin precession of the injected spins in the nonmagnetic (N) region. Figures adapted from reference [60].

$$\frac{\partial s}{\partial t} + \nabla J_s = s \times \omega - \frac{s}{\tau_s}. \tag{2.13}$$

The most general solution of this 1D equation for a spin with initial condition $s(x,0) = s_0$ and a magnetic field pointing along the z-direction (precession in the xy plane) is

$$s_x(x_1, x_2, B, t) = \frac{s_0}{\sqrt{4\pi D_s \tau_s}} e^{-(x_2 - x_1 - v_d t)^2/4D_s t} e^{-t/\tau_s} sin(\omega t) \tag{2.14}$$

The steady state condition is acquired after integration over the contact dimensions x_1, x_2 and over all possible transport times t. The behavior for the total spin density in materials, $S = n_\uparrow - n_\downarrow$ follows similar dynamics.

2.4 Conductivity Mismatch

One crucial aspect for efficient spin injection in all types of materials, but especially in SCs, is the interface formed between the FM and the material acting as the spin transport channel. It was quickly realized that spin injection into SCs is not trivial. Direct spin injection from FM metals to SCs has shown low efficiency due to the *conductivity mismatch*, only 0.1-1% as shown by Hammar et al. (1999) [61]. Conductivity mismatch refers to the very large difference in conductivity between a FM metal and a SC. The spin-up and spin-down subbands in a SC are equally populated resulting in zero spin polarization. Even though a FM has a higher density of states for one of the spin

subbands, because of the limited conductivity of the SC for both spin channels, equal number of spin-up and spin-down carriers will be injected inside the SC, and as a result the spin polarization of the injected current is zero.

Schmidt et al. (2000) [23] calculated the spin polarization of the injected current from a FM into a SC as a function of the polarization of the FM by solving the spin transport equations at the interface, and concluded that in order to achieve high injection efficiency one of two criteria needs to be satisfied: (1) The conductivities of the FM and the SC have to match (which is impossible); or (2) a fully spin-polarized ferromagnet. However, even in the case of a 90% polarized FM Schmidt et al. showed that the magnetoresistace signal $\Delta R/R_{parallel}$ is smaller than 10^{-7}, thus very difficult to be experimentally detected.

Rashba [62], Fert and Jaffres [24], as well as Smith and Silver [63] proposed that the conductivity mismatch problem can be solved by inserting a spin dependent and large enough interface resistance, such as a tunnel barrier. The tunnel barrier induces a discontinuity of the chemical potentials at the interface, which partially restores the spin polarization of the current. This was shown experimentally by Hanbicki et al. (2002), who fabricated a Fe/AlGaAs/GaAs semiconductor LED structure, and realized spin injection with an efficiency of 30%. Furthermore, the tunneling process is nearly temperature independent, and can be modulated by adjusting the tunnel barrier width and height for Schottky barriers (doping modulation) or by controlling the thickness for oxide layers. Consequently, the spin polarization of the current can be (partially) tuned.

The theoretical model describing the spin transport equations at the FM/SC interface is a linear-response model including the behavior of the electrochemical potentials for up and down spin channels; at the FM/SC interface there is a splitting of the electrochemical potentials for spin-up and spin-down electrons. This theory is based on the assumption that spin-scattering occurs on a much slower timescale than other scattering processes. Under this assumption, Ohm's law and the diffusion equation are written for two independent electrochemical potentials $\mu_\uparrow$ and $\mu_\downarrow$, which do not have to be equal. Specifically, the equations are:

$$\frac{\partial \mu_{\uparrow,\downarrow}}{\partial x} = -\frac{e j_{\uparrow,\downarrow}}{\sigma_{\uparrow,\downarrow}}, \tag{2.15}$$

$$\frac{\mu_\uparrow - \mu_\downarrow}{\tau_s} = \frac{D\partial^2(\mu_\uparrow - \mu_\downarrow)}{\partial x^2} \tag{2.16}$$

where $j_\uparrow, j_\downarrow$ and $\sigma_\uparrow, \sigma_\downarrow$ are the current densities and conductivities for the two spin subbands respectively, D is the spin diffusion constant, and τ_s is the spin relaxation time. The total current is expressed as $j = j_\uparrow + j_\downarrow$. The resistivities are written as

$$\rho_{\uparrow(\downarrow)} = 2[1 - (+)\beta]\rho_F^* \tag{2.17}$$

for the the spin $\uparrow$ ($\downarrow$) channel in the FM, where β indicates the spin asymmetry and ρ_F^* the resistivity of the bulk metal, and

$$\rho_{\uparrow(\downarrow)} = 2\rho_N^* \tag{2.18}$$

for the resistivity of the nonmagnetic SC, where ρ_N^* is the resistivity of the bulk nonmagnetic SC. Combining these equations gives the expression for the variation of the electrochemical potentials for each subband, $\Delta\mu_{\uparrow(\downarrow)} = \mu_{\uparrow(\downarrow)}(x = x_0^+) - \mu_{\uparrow(\downarrow)}(x = x_0^-) = r_{\uparrow(\downarrow)} j_{\uparrow(\downarrow)}$ (x_0^+, x_0^- are the positions immediately to the right and left side at the interface, respectively), with respect to the distance from the interface x. The spin dependent interface resistance is defined as $r_{\uparrow(\downarrow)} = 2r_b^*[1 - (+)\gamma]$, where r_b^* is the interface resistance area product, and γ the spin asymmetry (polarization) coefficient at the interface. The equation for the variation of the electrochemical potentials is:

$$\frac{\partial^2 \Delta\mu_{\uparrow(\downarrow)}}{\partial x^2} = \frac{\Delta\mu_{\uparrow(\downarrow)}}{L_s^2} \tag{2.19}$$

The associated boundary conditions are the continuity of the current densities $j_\uparrow$ and $j_\downarrow$, and the discontinuity of the chemical potentials for the two spin subbands $\mu_\uparrow$ and $\mu_\downarrow$ adjacent to the interface at $x = x_0$. Solving this boundary condition problem gives rise to the dependence of the spin polarization of the current on the interface resistance. The final result is:

$$P_j = \left(\frac{j_\uparrow - j_\downarrow}{j}\right) = \frac{\beta r_F + \gamma r_b^*}{r_F + r_N + r_b^*}. \tag{2.20}$$

where r_F, r_N are the spin resistivities of the FM and SC respectively, which are defined as:

$$r_F = \rho_F^* \times \lambda_N^F, \tag{2.21}$$

$$r_N = \rho_N^* \times \lambda_N^{SC} \tag{2.22}$$

where λ_N^F and λ_N^{SC} are the spin diffusion lengths for the FM and the SC, respectively. This is a powerful expression which captures the basic physical picture for the spin injection process. If we set $r_b^* = 0$ this equation becomes:

$$P_j = \frac{\beta}{1 + r_N/r_F}. \tag{2.23}$$

When $r_N \sim r_F$ the current spin polarization is only moderately reduced from the FM's value β. However, when $r_N \gg r_F$, the spin polarization of the current becomes negligible. When $r_b^* \neq 0$, even for $r_N \gg r_F$, the spin polarization remains significant under the condition $r_b^* > r_N$. Figure 2.5 (a) shows the variation of the chemical potential for a FM/nonmagnetic metal interface without interface resistance (Co/Cu) and the corresponding spin accumulation (inset). In this case there is no discontinuity of the chemical potentials at the interface, and the current remains spin polarized since there is no conductivity mismatch. Figure 2.5 (b), (c) show calculated results of how the interface resistance affects the spin accumulation and the spin polarization of the current at a FM/SC interface with and without interface resistace r_b^* according to Equation 2.20.

As it is clear from Figures 2.5 (b), (c), the chemical potential discontinuity, and the interface resistance r_b^* are both prerequisites for efficient spin injection at a FM/SC interface. The physical picture explaining this dependence is the following. In the absence of interface resistance, the Fermi energy splitting due to spin accumulation ($\Delta\mu$) has the same value on both sides of the interface, and it decays exponentially with decay lengths λ_N^F and λ_N^{SC}. The variation of the current spin polarization in the FM and SC is proportional to the variation of the chemical potentials in the corresponding regions. The variations of the spin accumulation $\Delta\mu$ are proportional to the corresponding total number of spin flips in the FM and SC regions. If $\Delta\mu$ is continuous, the total number of spin-flips in the FM is proportional to $1/r_F$, and for the SC it is proportional to $1/r_N$. Since $r_F \ll r_N$, there are many more spin-flips in the FM region than in the SC region. Thus, the current is almost completely depolarized when it passes through the interface. Introducing an interface resistance results in a more balanced number of spin-flips in the two regions. Due to the spin dependent interface resistance, $\Delta\mu$ is discontinuous at the interface, which leads to a much higher $\Delta\mu$ in the SC than in the FM; therefore, spin polarized current can be passed from the FM to the SC. A tunnel barrier has spin dependent resistance because of the difference in Fermi wave vectors for the two spin types within the contact material [65].

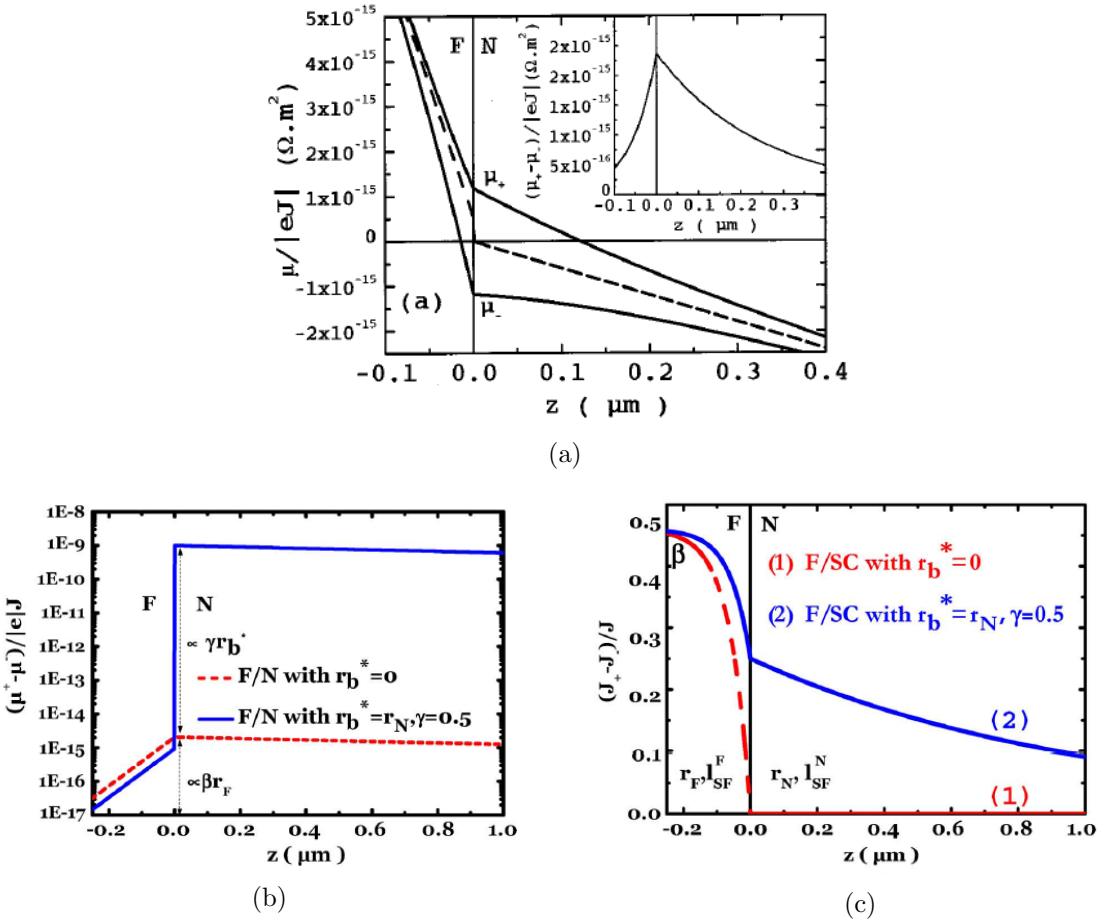

Figure 2.5: (a) Variation of the electrochemical potentials as a function of the distance perpendicular to the interface at a FM/nonmagnetic metal interface without interface resistance (Co/Cu). The inset is the spin accumulation $\Delta\mu = \mu_+ - \mu_-$ [24]. (b) Calculated spin accumulation for Co/GaAs interface with and without interface resistance. (c) Calculated current spin polarization for Co/GaAs interface with and without interface resistance [64].

Over the years, there have been a lot of theoretical and experimental studies on the effect of the interfacial properties on spin injection. These studies involve both Ohmic and tunnel contacts. In the case of tunnel contacts, thin oxide barriers [66, 10, 67, 68], Schottky barriers [8, 69, 70, 71, 11, 14], and graphene barriers [72] have been explored.

Lastly, it is important to point out that the geometry of a spin device does affect the magnetoresistance signal, $\Delta R/R_P = (R_P - R_{AP})/R_P$, that can be achieved due to spin injection. For a FM/N/FM structure in the spin valve geometry shown in Figure 2.6 (a), the expression for ΔR can be expressed as [24]:

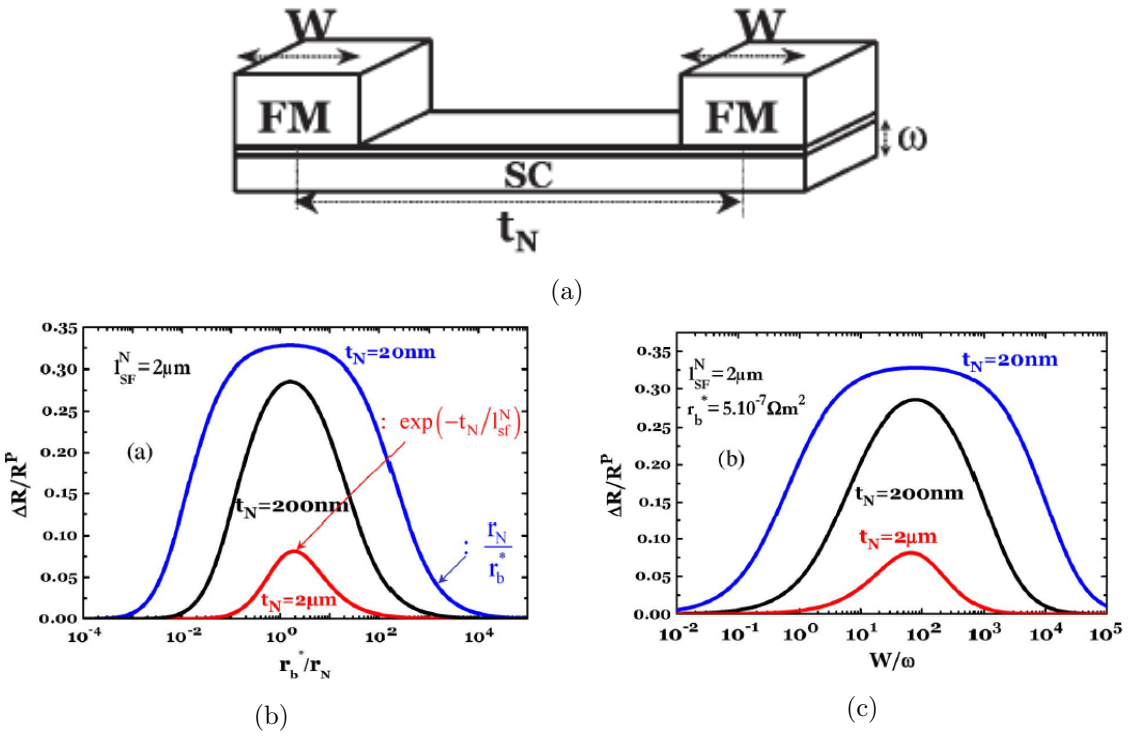

Figure 2.6: (a) Spin valve geometry for a FM/N/FM structure. (b) $\Delta R/R^P$ for a FM/I/N/I/FM structure as a function of the normalized tunnel resistance for different values of the channel length t_N and the spin diffusion length l^N_{sf}. (c) $\Delta R/R^P$ as a function of the contact width to channel thickness ratio W/ω for different values of channel length and fixed interface resistance $r^\star_b = 5 \times 10^{-7}\ \Omega \cdot m^2$ [64]

$$\Delta R = \frac{2(\beta r_F + \gamma r_b^*)^2}{(r_b^* + r_F)cosh(\frac{t_N}{\lambda_N}) + \frac{r_N}{2}\left[1 + \left(\frac{r_b^*}{r_N}\right)^2\right] sinh(\frac{t_N}{\lambda_N})}. \tag{2.24}$$

This equation sets the boundaries for the magnetoresistance signal. A large magnetoresistance requires correlated values of the tunnel resistance r_b^* and channel thickness t_N, and the range for the interface resistance in order to achieve such values is $r_N(t_N/\lambda_N) < r_b^* < r_N(\lambda_N/t_N)$. For $r_b^* \ll r_N(t_N/\lambda_N)$, the discontinuities in the electrochemical potentials introduced by the interface resistance are too small to generate a high enough splitting and the current is depolarized (conductivity mismatch regime). However, there is a regime where the interface resistance is too large $r_b^* \gg r_N(\lambda_N/t_N)$, and the splitting in the electrochemical potentials has saturated and the magnetoresistance drops to zero. Physically, in that regime the spins dwell in the channel longer than the

spin relaxation time, and as a result depolarize. In other words, the spin injection rate is smaller than the spin relaxation rate in the SC channel.

In conclusion, there is a window of the interface resistance that results in significant magnetoresistance signals. The lower limit of the window, $r_b^* > r_N(t_N/\lambda_N)$, is the condition for realizing spin injection from a FM to a SC; while the upper limit of the window, $r_b^* < r_N(\lambda_N/t_N)$, is the condition for conservation of the spin accumulation in the SC channel. Figure 2.6 (b) shows the dependence of the magnetoresistance signal with respect to different interface resistance values for different channel lengths, and Figure 2.6 (c) shows the magnetoresistance dependence on the contact width to channel thickness ratio (W/ω) for different values of channel length (t_N) and fixed interface resistance (r_b^*).

2.5 Spin-Orbit Coupling in Semiconductors

The most fundamental spin-dependent interaction in nonmagnetic SCs is spin-orbit coupling (SOC). SOC is a relativistic effect that plays a major role in various spin relaxation mechanisms. The reason being that there is a finite probability for an electron to approach a nucleus and strongly interact with the very strong electric field produced by the nuclear charge $+Ze$ at the center. Due to relativistic effects, it is known that in the electron's rest frame, because of the presence of the nuclear electric field, the electron will also experience a magnetic field $B = (1/c^2)E \times v$, which is parallel to the orbital angular momentum L. The Hamiltonian describing this interaction is $H_B = -\mu \cdot B$. This interaction is the spin-orbit interaction (SOI), which gives an $L \cdot S$ term in the total Hamiltonian of the system (the spin-orbit term arises naturally from the Dirac equation). Due to SOI, the degeneracy of the energy levels is split (valence band and conduction band in the case of a semiconductor). The following derivation is a simple quantitative description of SOI using semi-classical electrodynamics and non-relativistic quantum mechanics:

$$\mathbf{B} = -\frac{\mathbf{v} \times \mathbf{E}}{c^2} \rightarrow \mathbf{B} = \frac{\mathbf{r} \times \mathbf{p}}{m_e c^2} \left| \frac{E}{r} \right|. \tag{2.25}$$

Next, by setting $\mathbf{E} = -\boldsymbol{\nabla} V$, $U = eV$ and that the angular momentum is $\mathbf{L} = \mathbf{r} \times \mathbf{p}$, we get,

$$\mathbf{B} = \frac{1}{m_e e c^2} \frac{1}{r} \frac{\partial U(r)}{\partial r} \mathbf{L}. \tag{2.26}$$

SOC drives the precession of the electron spin, while momentum scattering makes this precession randomly fluctuating, both in magnitude and direction. In SCs, due to the crystal structure, the

SOI depends not only on the velocity of the electrons, but also on the band structure itself. SOC is the driving force for the tremendously active field of spintronics and other fundamental research areas in physics. A few examples in condensed matter physics are the spin Hall Effect, topological insulators, Majorana fermions, Dirac materials, chiral magnonics, spin-orbit torques, and spin-orbit qubits.

2.5.1 Bychkov-Rashba and Dresselhaus Effects

The basic effect of SOI in SCs is to break the degeneracy of the energy levels of spin-up and spin-down states, meaning that the parabolic dispersion curve of the electron energy will split into two curves centered symmetrically away from the Γ-point of the Brillouin zone. The aforementioned spin splitting arises from linear and cubic terms of momentum appearing in the Hamiltonian of the system. Taking into account the SOC effect, the Schrödinger equation for the conduction electrons in semiconductors in the most general case is

$$\left[\frac{\boldsymbol{p}^2}{2m^*} + V_0(\boldsymbol{r}) + V(\boldsymbol{r}) + \frac{\hbar}{4m_0^2c^2}(\boldsymbol{\nabla}V \times \mathbf{p}) \cdot \boldsymbol{\sigma}\right] \Psi_{n\mathbf{k}}(\boldsymbol{r}) = E_{n\mathbf{k}}\Psi_{n\mathbf{k}}(\boldsymbol{r}), \tag{2.27}$$

where $V_0(\boldsymbol{r})$ is the crystal potential and $V(\boldsymbol{r})$ is any other possible potential existing in the crystal or the electric potential from external electric fields.

The spin splitting can be induced either by the Rashba effect or by the Dresselhaus effect. In SCs with space inversion symmetry (e.g., silicon), the Bloch states in the band are doubly spin degenerate, and they stay degenerate in the presence of SOC due to time reversal symmetry.

$$\Psi_{\mathbf{k},n\uparrow}(\mathbf{r}) = \quad [\alpha_{\mathbf{k}n}(\mathbf{r})|\uparrow\rangle + b_{\mathbf{k}n}(\mathbf{r})|\downarrow\rangle] \exp(i\mathbf{k}\cdot\mathbf{r}) \tag{2.28}$$

$$\Psi_{\mathbf{k},n\downarrow}(\mathbf{r}) = \left[\alpha^*_{-\mathbf{k}n}(\mathbf{r})|\downarrow\rangle - b^*_{-\mathbf{k}n}(\mathbf{r})|\uparrow\rangle\right] \exp(i\mathbf{k}\cdot\mathbf{r}) \tag{2.29}$$

These two Bloch states have the same energy (Kramers theorem), and $|\alpha_{\mathbf{k}n}| \approx 1$ while $|b_{\mathbf{k}n}| \ll 1$ due to the weak SOC. It is worth mentioning that these states are not eigenstates of $\hat{\sigma_z}$. There are two ways of breaking this degeneracy. The first one is to break the time reversal symmetry by applying an external magnetic field. The second is to break the spatial inversion symmetry of the crystal, which is true for III-V materials such as GaAs, InSb, InAs, etc. In general, SOI can also break the spin degeneracy by two mechanisms. One of them originates from the structure inversion asymmetry (SIA) of the confining potential and is referred as the Bychkov-Rashba SOI [73]. This

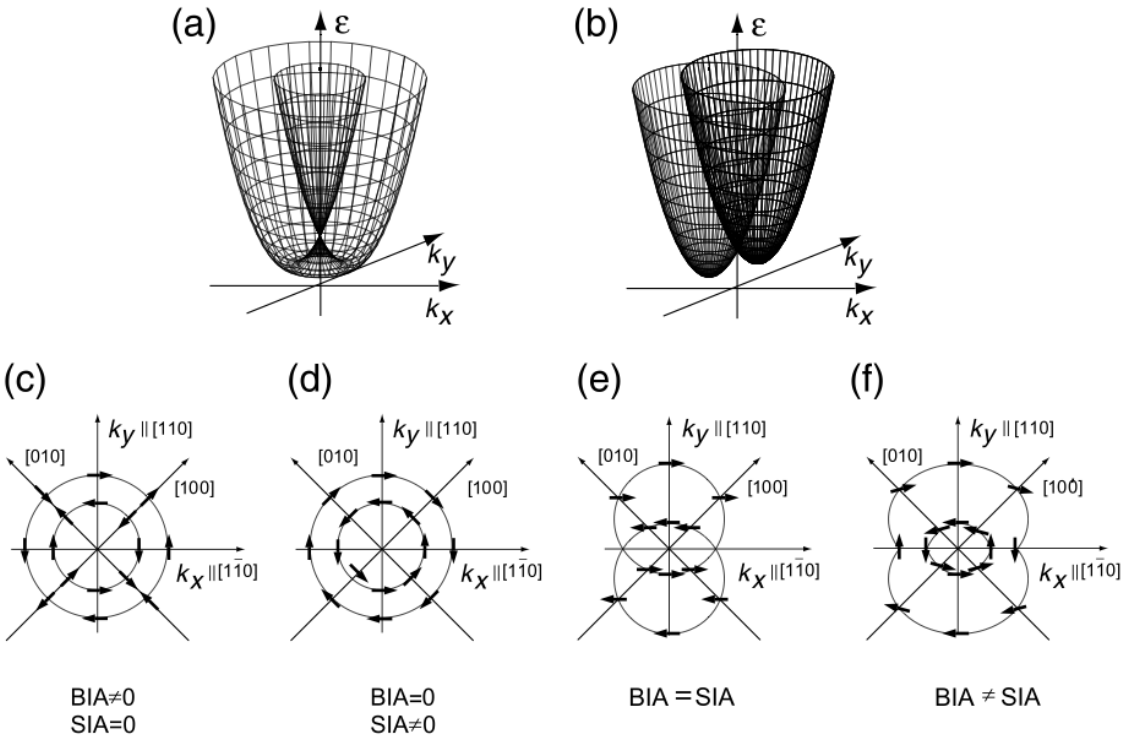

Figure 2.7: Schematic diagram of a 2D energy band structure for a system with linear momentum terms in the SOI Hamiltonian. a) Only BIA or SIA. b) BIA=SIA, (c-f) The distribution of the spin orientation at the Fermi level with various ratio of BIA/SIA. Figure is adapted from Ganichev and Prettl (2003) [38].

can be observed in all types of systems where additional electric fields exist due to the interfacial asymmetry. The Bychkov-Rashba term is linear in the wave vector $\mathbf{k}$.

The other mechanism arises from the crystal bulk inversion asymmetry (BIA) of the material and is called the Dresselhaus SOI [74]. The Dresselhaus interaction term is linear in the wave vector $\mathbf{k}$ as well. However, when interactions between the conduction band electrons and the valence band electrons are taken into consideration, a cubic term in the wave vector may also arise.

The Bychvov-Rashba SOI can be viewed as a momentum dependent effective magnetic field. The Bychkov-Rashba Hamiltonian for a 2D system is [75]:

$$H_{BR} = \mu_B \boldsymbol{\sigma} \cdot \mathbf{B_{eff}}(\mathbf{k}) \tag{2.30}$$

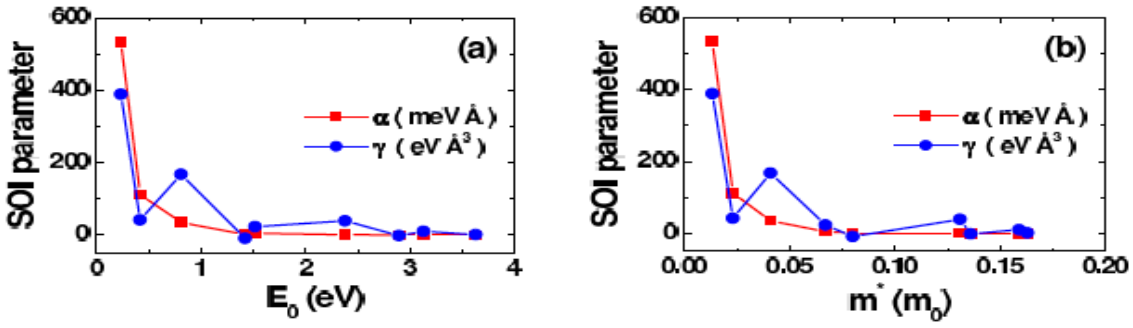

(a) (b)

Figure 2.8: Theoretical SOI parameters α and γ as functions of (a) the energy gap E_0, and (b) the effective mass m^*. Figure is adapted from Fabian *et al* [60].

where the k-dependent magnetic field is:

$$\mathbf{B_{eff}}(\mathbf{k}) = \frac{1}{\mu_B}\alpha_{BR}(-k_y, k_x, 0). \tag{2.31}$$

In general, it is written in the form $H_{BR} = \alpha_{BR}[\boldsymbol{\sigma} \times \mathbf{k}] \cdot \mathbf{n}$, where $\mathbf{n}$ is a unit vector directed along the normal of the heterojunction (e.g., xy-plane). The spin degenerate subband splits into two subbands (up and down spin) with different energies. The energies are given by

$$\epsilon_\sigma(\mathbf{k}) = \epsilon_0(\mathbf{k}) + \alpha_{BR}\sigma k_{||}, \sigma = \pm 1. \tag{2.32}$$

When both mechanisms have to be considered, the SOI Hamiltonian becomes,

$$H_{SO} = \alpha_{BR}(k_x\sigma_y - k_y\sigma_x) + \gamma_D(k_x\sigma_x - k_y\sigma_y) \tag{2.33}$$

where α_{BR}, γ_D are the Bychkov-Rashba and Dresselhaus parameters respectively, and σ_x, σ_y the Pauli matrices. Figure 2.7 depicts how a 2D band structure is transformed in the presence of BIA and SIA. The effective magnetic field is given by

$$\mathbf{B_{eff}}(\mathbf{k}) = \frac{1}{\mu_B}(\gamma_D k_x - \alpha_{BR}k_y, \alpha_{BR}k_x - \gamma_D k_y). \tag{2.34}$$

And the SOI energy splitting is given by $\Delta\epsilon_0 = 2\mu_B|\mathbf{B_{eff}}|$, i.e.,

$$\Delta\epsilon_0 = 2k_{||}\sqrt{\alpha_{BR}^2 + \gamma_D^2 + 2\alpha_{BR}\gamma_D sin(2\phi)}. \tag{2.35}$$

The Bychkov-Rashba and Dresselhaus parameters depend on the energy gap E_0 and the effective mass m^*, which is shown in Figure 2.8. The Bychkov-Rashba parameter increases with decreasing

E_0 and/or m^*. The Dresselhaus parameter exhibits an oscillating behavior. These spin-orbit related effects are very important and they dictate the spin relaxation processes in semiconductors. However, the efficient coupling of the electron spin to its motion by the Rashba and the Dresselhaus interactions is also a way to control spin precession. For example, the spin FET proposed by Datta and Das is based on the fact that the SOC parameters can be tuned by an external electric field (gate electric field).

2.6 Spin Relaxation Mechanisms

Spin relaxation is the effect of fluctuations of spin interactions that induce spin dephasing. In this subsection, the five major spin relaxation mechanisms of conduction electrons in semiconductors are introduced and described. They are schematically represented in Figure 2.9. In SCs, spin relaxation depends on several factors such as the symmetry of the crystal structure, the purity of the crystal, and the carrier doping density. In principle, different relaxation mechanisms can coexist, but usually one of them dominates spin relaxation and dephasing in a particular material.

a) The Elliot-Yafet mechanism, where the spin relaxes by momentum scattering off impurities or phonons. It was proposed by Elliot [76] and Yafet [77]. In this scheme, as it was pointed out in the spin-orbit coupling section, the electronic eigenstates (Bloch states) are spin up and spin down spinors. Due to spin-orbit interaction these states are mixtures of both spin-up and spin-down electrons, but with very small spin mixing ($|b| << 1$). As a result, every momentum scattering event has a finite probability to flip the spin from "up" to "down", and hence leads to spin relaxation. In addition, the lattice vibrations (phonons) can couple to spin via the spin-orbit interaction and cause spin flipping. A more simplistic picture to understand these effects is that the random electric field from the lattice vibrations or charged impurities is transformed to an effective random magnetic field through the spin-orbit interaction, which gives rise to spin relaxation. Spin relaxation by lattice vibrations is rather weak at low temperatures. For impurity scattering, the direction and value of the random magnetic field depends on the properties of the individual collision. Within this picture, every collision rotates the spin by a small angle ϕ and all the collisions are uncorrelated. The average square of spin rotation angle during time t is of order $< \phi^2 > (t/\tau_p)$, where τ_p is the momentum relaxation time (time between collisions). The

correlation between the spin relaxation time and the momentum relaxation time is given by

$$\frac{1}{\tau_s} \approx \frac{<\phi^2>}{\tau_p}. \tag{2.36}$$

The main conclusion is that the relaxation rate is proportional to the impurity concentration, which means that the faster the momentum scattering is, the faster the spin relaxation occurs. It is estimated that an electron has to undergo 10^5 scattering events for a spin flip to occur.

b) The Dyakonov-Perel mechanism, where the spin-orbit interaction behaves as an effective, momentum dependent magnetic field [78]. Electrons having an initial momentum feel an effective magnetic filed, which results in spin precession around the axis of that field. During momentum scattering, electrons change their momentum randomly, and after consecutive collisions they feel a different magnetic field (magnitude and direction changes). The precession frequency and axis change randomly, which can be described as motion of electron spin in a fluctuating magnetic field. The additional spin-dependent term in the Hamiltonian is $\hbar\Omega(p) \cdot S$, which is the energy of a spin in an effective magnetic field. Since the spin precession frequency is momentum dependent, the effective magnetic field changes with time. Thus the correlation time is on the order of the momentum relaxation time, τ_p, and for small $\Omega\tau_p$ the expression for the relaxation rate is

$$\frac{1}{\tau_s} \sim \Omega^2 \tau_p. \tag{2.37}$$

In contrast to the Elliot-Yafet mechanism, the spin rotates instead of flipping between adjacent collisions. Thus, the relaxation rate increases when the impurity concentration decreases. This mechanism is present in bulk crystals without a center of inversion symmetry, such as GaAs and InAs (zincblende structure), as well as in SC heterostructures/nanostructures, where the structure and interface spatial inversion asymmetry brake the spin degeneracy (even in crystals with a center of inversion symmetry). The most striking difference between EY and DP is their contrasting dependence on the momentum relaxation time. Another difference is the energy dependence of DP (cubic) compared to EY (quadratic). In general, DP mechanism is a stronger spin relaxation mechanism, especially at higher temperatures and large donor doping levels, whereas the Elliot-Yafet mechanism can be dominant in materials with small band gaps and large spin-orbit coupling.

c) The Bir-Aronov-Pikus mechanism, which is due to electron-hole exchange scattering and can be the dominant contribution in p-doped SCs [79]. The spin relaxation rate is proportional

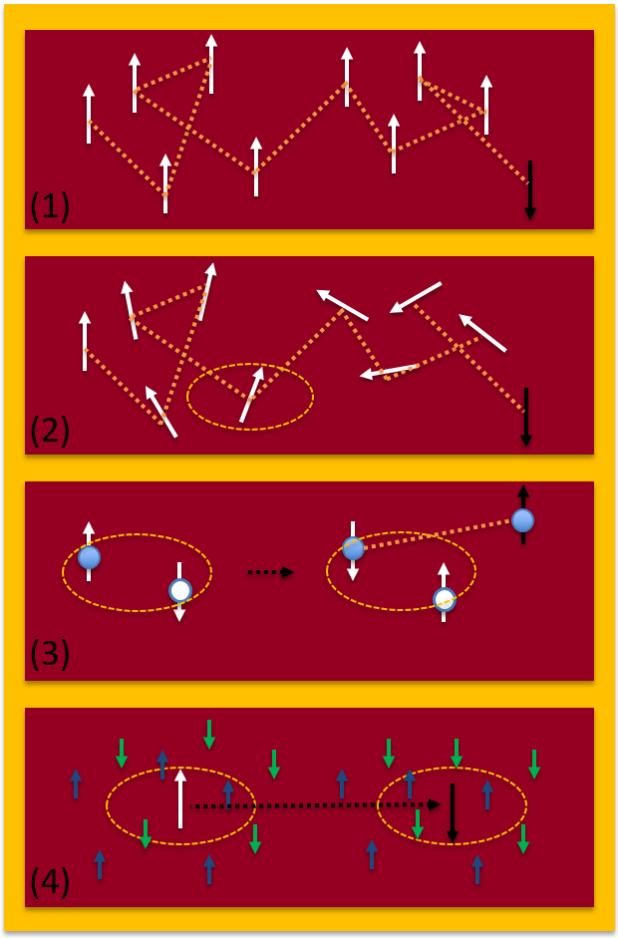

Figure 2.9: Mechanisms of spin relaxation in semiconductors.(1) The Elliott-Yafet mechanism: electrons scatter off impurities or phonons and can flip their spin at each scattering event. (2) Dyakonov-Perel mechanism: electrons spins precess along a momentum dependent magnetic field. At each scattering event the direction and the frequency of the precession changes randomly, which can be described by a random walk in a fluctuating magnetic field. (3) Bir-Aronov-Pikus mechanism: electrons exchange spins with holes (circles), which then lose spins very fast due to the Elliott-Yafet mechanism. (4) Hyperfine interaction: electrons with localized wave functions (dashed circles) interact with nuclear spins, which causes spin relaxation and dephasing (reproduced from reference [60]).

to the number of holes, and that is the reason why it is dominant in heavily p-doped SCs. This mechanism can become important, because spin and momentum relax very fast for holes. This is due to the strong spin-orbit coupling in the valence band compared to the conduction band. Within the valence band the relaxation follows the Elliot-Yafet mechanism, but with a very fast rate. Holes in the valence band can be described as a reservoir where spin equilibrium occurs.

d) The hyperfine interaction between nuclear spins and electron spins, $H_{hf} = I \cdot S$. The nuclei of the lattice provide a random effective magnetic field, which interacts with electron spins. This mechanism is important for localized electrons in insulating materials, but it is generally a weak effect. A well known effect, "dynamic nuclear polarization" is a hyperfine interaction effect which has been studied in FM/SC hybrid structures [80].

e) The anisotropic exchange interaction, which is relevant in doped SCs, but only in the insulating regime. This interaction originates from the anisotropic exchange field produced by randomly oriented spins of adjacent dopant electrons, which results in an effective magnetic field that promotes spin precession. This interaction exists in materials that lack inversion symmetry, either due to the bulk crystal structure, or as a result of interfacial asymmetric structures [81].

The Elliot-Yafet mechanism, the D'yakonov-Perel mechanism, and the Bir-Aronov-Pikus mechanism dominate spin relaxation in the mettalic regime. Hyperfine interaction and the anisotropic exchange interaction dominate spin relaxation in the insulating regime, where the wavefuctions of the electrons are localized. All the mechanisms can be interpreted in terms of effective magnetic fields acting upon the electron spin, and as a result they cause spin relaxation due to precession.

2.7 Spins in Silicon

Efficient spin injection and transport in Si is of great importance if we want to extend the functionalities of today's Si technologies. In this section, I will briefly discuss the efforts that have been done for realizing electrical spin transport in Si, as well as spin dynamics in Si, including relaxation mechanisms and spin lifetimes with varying parameters, such as temperature and doping density.

The main characteristics that render Si a good candidate for spin transport applications are:

1. A low atomic number ($Z = 14$), which means that the spin-orbit coupling strength is low (the spin-orbit energy splitting is $\Delta E \sim Z^4$, or $\Delta E \sim Z^2$ if screening from core electrons is included).

2. A spatial inversion symmetric crystal structure, which results in a spin degenerate conduction band, and as a result bulk Si is insensitive to the 'Dyakonov-Perel' spin relaxation mechanism.

3. Silicon's most abundant isotope (^{28}Si), has zero nuclear spin, hence there is no contribution to spin relaxation from the hyperfine interaction.

The first spin transport experiments in Si were conducted using ballistic hot-electron techniques [82]. After these experiments many groups tried to perform electrical spin transport experiments in Si with ohmic FM/Si contacts, but because of the conductivity mismatch problem the results were not promising. Efficient spin injection in Si was demonstrated after the conductivity mismatch problem was addressed by introducing oxide tunnel barriers (Al_xO or MgO) or Schottky barriers to increase the interface resistance [10, 83, 28]. Subsequent experiments using the four-terminal (4T) nonlocal and three-terminl (3T) local geometries further indicated efficient electrical spin injection in Si [67]. The afformentioned experiments prove that spin injection is feasible in Si, as well as the potential for realizing spin FETs. Extending these concepts in Si NWs is naturally the next step towards nanoscale devices. This thesis is focused on utilizing Si NWs as spin transport channels.

2.8 Spin Transport in Nanowires

Realizing spin transport in nanowires can prove advantageous, because of the useful physical properties that arise from one-dimensional (1D) confinement, such as reduced phonon density of states and ballistic transport. Among other advantages, surfaces states in NWs can introduce variations in carrier concentration along the length of the NW for small changes in diameter. Also, small variations in the concentration of impurity atoms can drastically alter the device performance.

Moreover, 1D confinement proves advantageous for spin transport applications as well. Specifically, it is proposed that by reducing the spin transport channel width, both the EY and DP spin relaxation mechanisms can be suppressed, resulting in longer spin lifetime and spin diffusion length [84, 85]. The EY mechanism, being proportional to momentum relaxation, is suppressed because phonon scattering is reduced in NWs as a result of the reduced density of states. The DP relaxation mechanism can be dimensionally constrained for widths as large as an order of magnitude larger than the electron mean free path [86].

It is important to point out that in materials with crystal inversion symmetry, the Dresselhaus SOI is absent. However, structural inversion asymmetry is inherent in all heterostructures, even the ones involving centrosymmetric crystals. The transverse electric field at the interface acts as a symmetry breaking field and leads to Rashba SOI. Consequently, in Si NWs Rashba SOI is present and contributes to spin relaxation [87].

2.9 Motivation for this Research

As it was pointed out, the FM/SC junction interface is considered to be the major factor for realizing efficient spin injection/detection, and it should exhibit some specific characteristics. It has been well established that spin injection efficiency depends not only on the properties of the FM contact material, but also depends crucially on the interface between the FM and the SC. The spin transport channel is also important, because it is the host for the spin relaxation mechanisms that depolarize the spins.

Some of the desirable attributes for the FM/SC junction which are also important for potential spin devices, are the following. High remnant magnetization which provides the desirable nonvolatile behavior, low coercive field and fast magnetization switching leading to low power consumption, highly spin polarized density of states (DOS) at E_F which produces large signals, low specific contact resistance to minimize the applied current densities and signal to noise ratios, and robustness against defects which can hinder spin injection.

The ability to inject spins into a SC by electrical means, along with the possibility to convert a spin accumulation into an electrical signal, is a prerequisite for spin transport and spin manipulation. Lateral structures for nonlocal bipolar spin injection/detection operations are of particular interest, especially those with the capability to add a gate electric field (tune SOI) and provide extended functionalities compared to conventional FETs.

The Si NWs used in this work provide an ideal system to study how different interfaces affect spin injection/detection. There are two main goals for the electrical spin transport experiments. The first is to study the FM/SC interface. The ability to form Ohmic-like contacts and Schottky barriers of differnt widths and heights on the same NW, due to the pronounced axial doping gradient along the length, provides a unique setup to study the dependence of the spin signals on the interfacial properties in a single Si NW. The second is to suggest new ways for fabricating lateral spin valve devices by taking advantage of asymmetric interfaces, and whether this approach can prove advantageous for bulk devices, and even more importantly for 1D devices. In 3D and 2D devices, a widely used approach to overcome the conductivity mismatch, while preserving sufficiently large current density, is to form graded doping profiles at the FM/SC interface to form a thin tunneling barrier. However, this approach is very difficult for 1D SCs, and one solution would

be to control the doping level along a NW, and thus manipulate the Schottky barrier characteristics in order obtain large spin signals.

CHAPTER 3

EXPERIMENTAL DETAILS

3.1 Silicon in Science and Technology

Silicon (Si), with atomic number 14, is the eighth most abundant element in the universe by mass. However, it is rarely found in the Earth's crust in its pure form. The crystalline form of Si was prepared for the first time in 1854 by Deville [88]. In scientific and technological applications the crystalline Si (c-Si) is of utmost interest due to the excellent and tunable electronic properties, which can be controlled by elemental doping in great precision. Doped Si is the major component for transistors, solar cells, semiconductor detectors, Raman lasers and many more semiconductor devices used in industry. In addition, monocrystalline Si is the most popular material for integrated circuits and is considered the most important material in computer industry. Monocrystalline Si can be prepared in intrinsic or extrinsic forms by the Czochralski process into single crystal ingots. Figure 3.1 (b) depicts Si ingots and polished wafers.

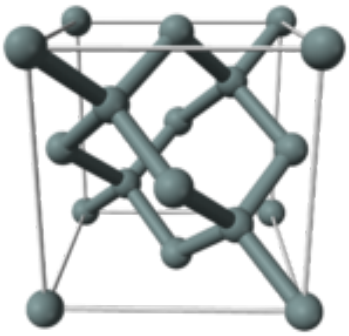

(a)

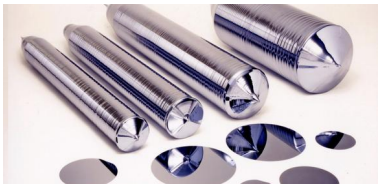

(b)

Figure 3.1: (a) Si diamond cubic crystal structure (unit cell). Image has been released into the public domain by Ben Mills. (b) Si single crystal ingots and polished wafers. Image has been released into the public domain by Michael Sweeney.

The crystalline stucture of Si under standard conditions is face-centered diamond cubic (Figure 3.1 (a)) with a lattice constant of 5.43 $\mathring{A}$, and electron configuration $[Ne]3s^2 3p^2$. Si is an indirect

bandgap semiconductor with energy gap $E_g = 1.12\ eV$ at 300 K. The effective mass of the electrons and holes are $m_e^\star = 1.08\ m_e$ and $m_h^\star = 0.60\ m_e$, respectively. The effective density of carriers at the band edges at room temperature are $N_c = 2.81 \times 10^{19}\ cm^{-3}$ and $N_v = 1.16 \times 10^{19}\ cm^{-3}$. The effective density of carriers can be calculated using:

$$N_c = 2\left(\frac{2\pi m_e^\star k_B T}{h^2}\right)^{\frac{3}{2}} \tag{3.1}$$
$$N_v = 2\left(\frac{2\pi m_h^\star k_B T}{h^2}\right)^{\frac{3}{2}}$$

These relatively low numbers of available states (compared to metals $\sim 10^{22}\ cm^{-3}$) lead to a low intrinsic carrier concentration of $n_i = 10^{10}\ cm^{-3}$ at room temperature, and very low conductivity $\sigma_i = n_i e(\mu_e + \mu_h) = 3 \times 10^{-6}\ \Omega^{-1} cm^{-1}$.

Increased conductivity is achieved with the insertion of small amount of dopant atoms. Even a small amount of dopants can significantly enhance the conducting properties of a SC. For example, Group V atoms, such as As, P, Sb, act as donors in a pure Si crystal. A shift in the Fermi level closer to the conduction band minimum results in an increase of the electron carrier concentration, and as a result an increase in the conductivity of the material as shown in Figure 3.2 (a). Figure 3.2 (b) shows the dependence of the Fermi level for Si as a function of temperature and impurity concentration.

The ability to tune the electrical properties of semiconductors via doping is the reason for the enormous technological breakthroughs that have been achieved in the past decades. Hence, the doping mechanisms are very important, and play a crucial role in this research. In this particular study, we are taking advantage of a special type of Si NWs, which exhibit an inhomogeneous doping profile that translates to an axial gradient in doping concentration along the length of the NWs. This effect is due to the simultaneous growth of NWs via vapor-liquid-solid and vapor-solid deposition under the presense of doping atoms.

Due to the importance of Si in today's semiconductor industry, it is apparent why it is desirable to study spin injection in Si. However, Si is not the best studied SC for spin injection and relaxation processes. In the research area of spintronics, GaAs has been studied more extensively [44, 90, 70, 91]. Spin relaxation in Si is less efficient than in GaAs. This is due to the fact that Si has a centrosymmetric crystal structure, which determines the effect of SOI inside the crystal. As it was

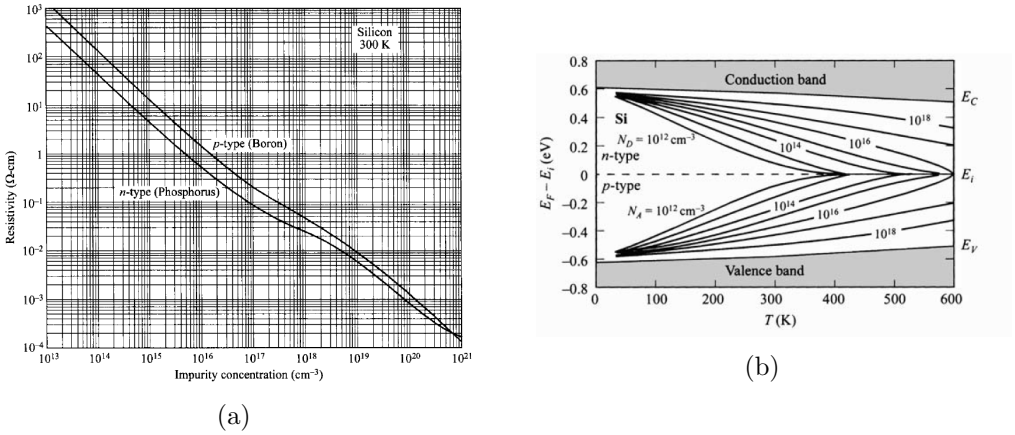

Figure 3.2: (a) Resistivity versus impurity concentration at 300 K for Si. (b) Fermi level for Si as a function of temperature and impurity concentration. The dependence of the bandgap on temperature is also shown [89].

extensively discussed in Chapter 2, microscopically SOI plays an important role in spin devices, both as a means for spin manipulation and as a primary source of spin decoherence. The g-factor in Si is about $g = 1.99875 \pm 0.0001$, indicating weak spin-orbit coupling, $E_{SO} = 0.044\ eV$. In comparison, GaAs has a g-factor $g \approx -0.44$. In addition, for ^{28}Si the nuclear spin is $I = 0$, so there is no contribution from the hyperfine interaction. Therefore, due to the centrosymmetric crystal structure, weak spin orbit interaction and zero nuclear spin, long spin lifetimes and spin relaxation lengths are expected in Si.

3.2 Silicon NWs Synthesis

3.2.1 Vapor-Liquid-Solid Method

The vapor-liquid-solid (VLS) is a common method to create one-dimensional structures, such as NWs, from chemical vapor deposition (CVD). In general, it offers high degree of control in length, diameter, composition and doping level of the produced NWs. This growth method was suggested by Wagner in 1964 [92]. Figure 3.3 shows a schematic of the VLS process. The first step for the VLS process is to coat a substrate with a few nanometers of a noble metal, such as gold or silver, in granular forms. Then the substrates are heated in a tube furnace while a gaseous reactant (precursor gas) is introduced in the chamber (e.g. silane SiH_4). VLS growth occurs when an alloy droplet, starting from the metal catalyst, becomes supersaturated with material from the gaseous reactant.

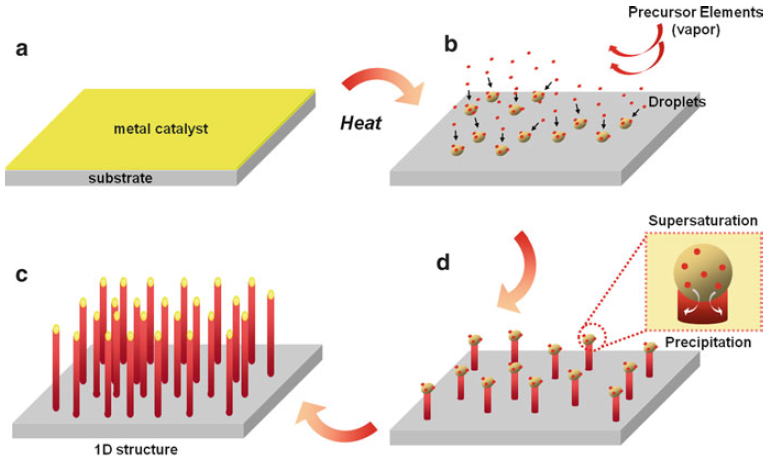

Figure 3.3: Growth of 1D structures by VLS mechanism. Figure is adapted from reference [93]

After the supersaturated point in which the actual concetration of the components is higher than the equilibrium concentration, the alloy droplet drives the precipitation of the component at the liquid-solid interface, and as a result a NW is formed. The growth continues as long as the vapor components are supplied.

The formation of the alloy droplet is important, since the growth temperature is defined by the eutectic point of the alloy. For example, the Au-Si eutectic point is $\sim 363°C$ when the ratio of the constituents is 4:1 Au:Si. The melting points of the individual constituents are higher than that of the eutectic alloy. For example, Si has a melting point temperature of $\sim 1414°C$. The Au-Si melting temperature is significantly lower ($\sim 363°C$), and as a result during the growth process Si atoms from the vapor state adsorb on the Au-Si droplets and then precipitate out of the droplet. The nucleation of the Au-Si alloy droplets on the surface of the substrate results in lowering the activation energy of direct vapor-solid (VS) growth.

3.2.2 Specific Growth Parameters

The Si NWs in our experiments are synthesized via a VLS method using silane (SiH_4) and phosphine (PH_3) precursor gases for the growth and doping respectively. The NWs were grown with the aid of our collaborator, Prof. Mei Zhang, from the Department of Industrial and Manufacturing Engineering at FAMU-FSU College of Engineering. Prof. Zhang's group has reported systematic growth of Si NWs on different substrates with similar growth parameters [94]. A CVD system that

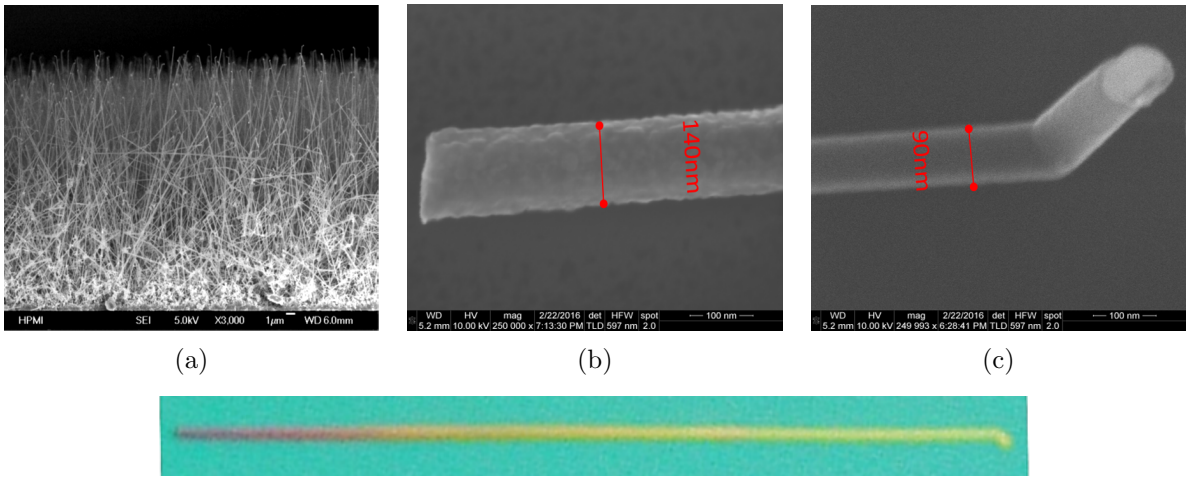

(a) (b) (c)

(d)

Figure 3.4: Si NW characteristics. (a) SEM image of as-grown Si NWs on a SiO_2 substrate. (b) Close-up SEM image of the base of a Si NW. (c) Close-up SEM image of the tip of a Si NW. (d) Optical micrograph of a Si NW. An obvious color difference between the base and the tip of the NW can be observed. The dark side is more electrically conductive than the light side.

allows precise control of the enviromental parameters, such as temperature, pressure, and gas flow rate, was utilized. In more details, the NWs are grown on SiO_2 substrates, which were coated with 4 nm of gold via thermal evaporation prior to the growth process. The substrates were transfered inside the CVD chamber and after reaching the base pressure, the chamber was filled with H_2 at a pressure of 20 Torr. The wafers were annealed at temperatures higher than the eutectic point of Si-Au ($\sim 363°C$), and the precursor gases were introduced in order to create Au-Si alloy droplets, which act as catalyst particles for the formation of the Si NWs. The growth took place at $460°C$ for a period of 15 minutes. SiH_4 gas was used as the source of Si at a flow rate of 80 sccm, and PH_3 gas was used to provide P dopants at a flow rate of 12 sccm. Upon completion of the growth the Si NWs are dispersed into an isopropanol solution via sonication. The diameter of the NWs ranges from $90 - 140$ nm and the length from $20 - 30$ μm.

Figure 3.4 (a) is an SEM image of as-grown Si NWs. The SEM reveals the high yield and uniformity of the growth, as well as a kink at the end of the NWs (gold catalyst) due to the different environmental conditions present at the end of the growth procedure. Figure 3.4 (d) is an optical image of a single Si NW under bright field. There is an obvious color variation along the length of the NW. This pronounced color difference is associated with a gradual change in the

electrical properties of the NW. Specifically, the dark side is significantly more conducting compared to the bright side. We will provide detailed electrical characterization measurements that support this argument. In addition, as we can see from Figures 3.4 (b), (c) there is also a concurrent change in the diameter along the length of a single NW from 140 nm to 90 nm.

The afformentioned observations are indications that there is a systematic inhomogeneity along the length of the NWs. Indeed, this inhomogeneity results in an axial doping gradient along the length of the NW, which yields the unique electrical properties.

3.3 Origin of the Axial Doping Gradient

In this section, I will present in more detail the mechanisms that are responsible for the formation of Si NWs with axial doping gradient. The main growth process of the NWs is via the VLS method. As mentioned earlier, during VLS growth a vapor precursor gas catalytically decomposes at a metal particle surface, forming a supersaturated eutectic liquid. The NWs grow by precipitation from the liquid catalyst droplet. Additional precursor gas(es) are used in order to provide dopant atoms that can modulate the electrical properties of the NWs.

However, the incorporation of the dopant atoms do not necessarily decompose only via the VLS growth mechanism. Indeed, once the NWs start forming, there is an additional radial growth mechanism at the surface of the NWs which involves a vapor-solid interface (VS growth). The dopant incorporation processes and rates for the two growth processes were studied by Lauhon's group in 2009 by using pulsed-laser atom probe tomography to elucidate the origins of the electronic properties of NWs at the atomic scale [95, 96]. Their studies revealed that there are two simultaneous growth mechanisms; VLS growth for the core of the NWs and nonselective VS deposition for the shell of the NWs. Furthermore, they showed that the dopant incorporation rates for the two growth mechanisms are different, with the nonselective VS growth being faster.

Figure 3.5 (a), (c) show the atom probe analysis of a P doped germanium NW. There is an apparent radial inhomogeneity in the doping concentration. Specifically, a heavily doped shell is surrounding a much lower doped core of the NW, as it is evident from the distribution of P atoms on the surface (grey spheres). Figure 3.5 (b) shows the presence of the native Si oxide formed around the shell of the NW. In addition, Figure 3.5 (d) demonstrates how the doping concentration

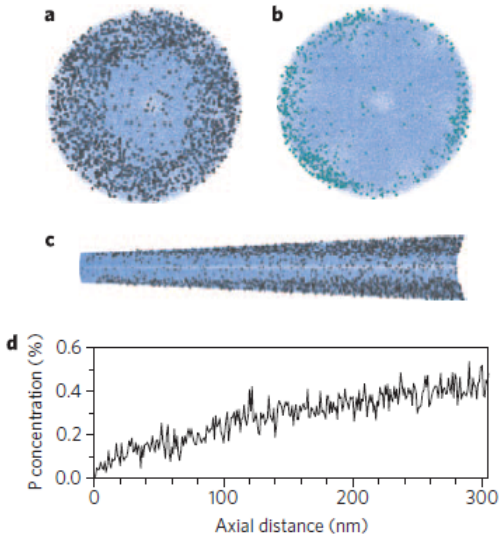

Figure 3.5: Distribution of dopant atoms. (a), (b) Distribution of phosphorus (a, grey spheres) and oxygen (b, light blue spheres) in a 43 *nm* in diameter germanium NW. (c) Side view of NW cross-section. (d) Average phosphorus concentration along the axial direction. Adapted from reference [95].

changes monotonically with respect to the axial distance where the origin represents the tip of the NW (catalyst droplet). Similar effects are observed during the growth of Si NWs.

The simultaneous growth via VLS for the core and VS for the shell of the NW results in a tapered morphology, and inhomogeneity in structure and composition. Figure 3.6 (a) shows schematically the two different pathways of growth, (i) VLS and (ii) VS. This type of growth results in the formation of a pronounced doping gradient along the axial direction of the NWs [96]. As a result, FET devices fabricated by placing a series of electrodes on a single NW exhibit a transition from Ohmic behavior (linear) to nonlinear contact-dominated behavior (rectifying) along the axial direction. The NW tip (catalyst droplet) is the region with less VS deposition, where the doping density is the lowest and the resistance is the highest.

One important observation that has to be noted is the following. The resulting higher surface doping does not affect the incorporation of dopants in the center of the NW via the VLS mechanism. That means that there is no diffusion of dopants from the surface of the NW to the core. As a result, the core of the NW is relatively uniformly doped. This is shown in Figure 3.6 (b) where the doping concentration is plotted as a function of the radial distance from the core of the NW.

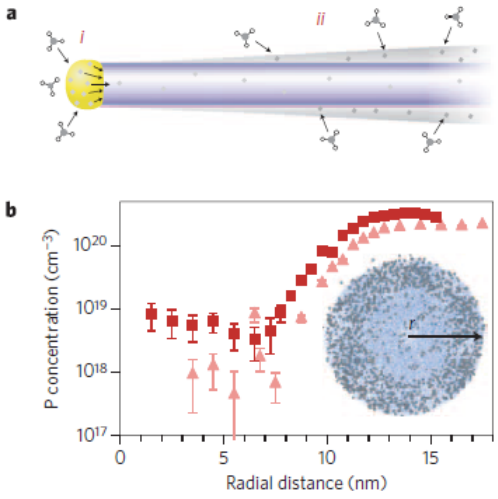

Figure 3.6: Doping incorporation pathways and radial distribution. (a) Representation of VLS growth for the core (i) and VS growth for the shell (ii) of the NW. (b) Phosphorus concentration versus the radial distance. The triangles and squares represent different $PH_3 : GeH_4$ ratios of $1 : 1000$ and $1 : 500$, respectively. Adapted from reference [95].

The doping concentration is roughly constant up to a specific diameter, within the core, and then it increases by more than an order of magnitude within the shell.

From the electrical characterization measurements performed on our Si NWs, which are going to be presented in the following chapter, we demonstrated that our Si NWs exhibit similar growth that leads to a pronounced gradient along the axial direction of the NWs. The dopant-enriched VS deposition alters the Schottky barrier characteristics of the metal/NW contacts which play a key role for the spin transport experiments, where I take advantage of this effect to study the dependence of spin injection/extraction on the junction resistance on a single NW.

3.4 Device Fabrication

The devices are fabricated in the so-called lateral spin valve geometry. The Si NWs are dispersed on $p^{++}-Si/SiO_2$ wafers with an additional Si_3N_4 layer on top. The $p^{++}-Si$ layer is a $500-550\ \mu m$, highly boron-doped wafer to serve as the backgate electrode in electrical gating measurements. On top of the highly doped layer, $250\ nm$ of SiO_2 is thermally grown and followed by a layer of $50\ nm$ of Si_3N_4. The SiO_2/Si_3N_4 bilayer serves as the primary dielectric for gating. The Si_3N_4 as a

passivation layer is superior to silicon dioxide due to its higher resistance to impurity diffusion and oxidation, as well as its higher dielectric constant ($\epsilon_r = 7.5$).

Alignment grids are prepatterned on the substrates by electron beam lithography (EBL) to help locating a specific NW. The grid is a 7×7 array of crosses separated by 150 μm. The substrates are cut in 5×5 mm^2 size squares and cleaned in a decontamination process. The process involves 5 min sonication in acetone, methanol, and isopropanol (IPA), followed by 2 min of oxygen plasma cleaning. The main purpose of the oxygen plasma cleaning is to remove organic contaminats (e.g. carbon) and promote adhesion.

Once a desired NW is located with an optical microscope, and the coordinates are determined, the wafer is spin-coated with polymethylglutarimide (PMGI) and polymethylmethacrylate (PMMA). Two layers of resist are used, which is a technique called "bilayer lithography", and it is used to form an undercut structure in order to achieve clean lift-off of deposited thin films.

The PMGI SF6 resist is spin-coated on the substrate at 5 krpm for 40 seconds, followed by hot-plate baking at $250°C$ for 90 seconds. The seconds layer of resist is 2% PMMA by weight in dichlorobenzene, and it is coated at 4 krpm for 30 seconds for a thickness of 85 nm. The PMMA is baked on a hot-plate at $155°C$ for 25 minutes before being transfered to the SEM for EBL.

Two different electrode patterns are employed, with different widths (0.8 to 1.2 μm) and separations (0.5 or 1.3 μm). The first is used for basic electrical characterization measurements with CoFe electrodes of the same width (1.0 μm) and separation (0.5 μm). The second pattern is used for spin transport measurements. It has alternating electrode widths of 0.8 μm and 1.2 μm and separation $1.1 - 1.8$ μm in order to obtain different coercive fields via shape anisotropy. An SEM micrograph indicating the electrode sizes and separation is shown in Figure 3.7 (c).

After EBL, the sample is developed in a 1:3 ratio of methyl-isobutyl-ketone: isopropanol (IPA) solution for 30 seconds at $19°C$, followed by a second step of development for the PMGI resist in 101A developer from Michrochem for 60 seconds at $19°C$. Finally, the sample is thoroughly rinsed with DI water and dried with pure nitrogen. Before the deposition of the FM electrodes, the native oxide on the Si NW is removed by bufferd HF etching (BOE) in order to ensure the formation of direct FM/SC contacts. The sample is submerged in BOE for 7 seconds, and then it is rinsed with DI water and dried with pure nitrogen.

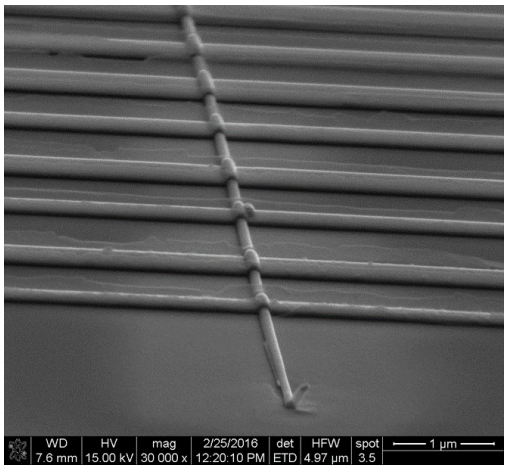

(a)

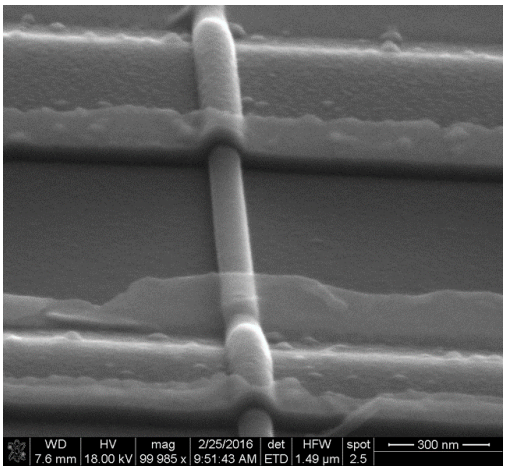

(b)

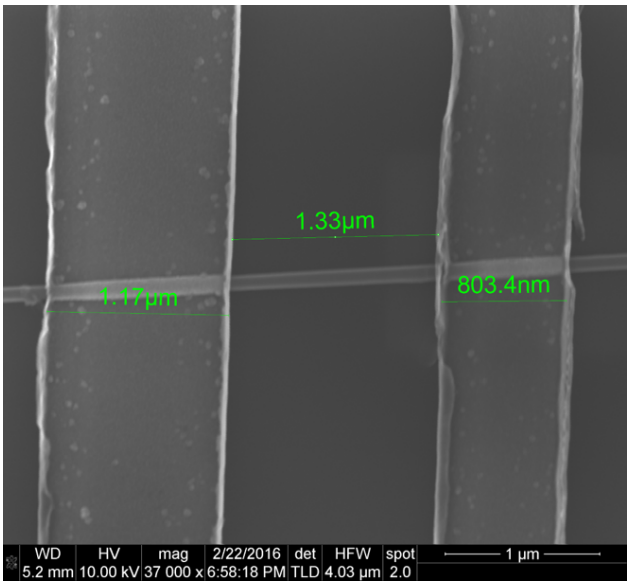

(c)

Figure 3.7: (a), (b) SEM images of a completed single Si NW device showing good deposition coverage of the Si NWs. (c) SEM image showing the different width and separation of the CoFe electrodes.

Immediately after the native oxide removal, the sample is transfered into the ultrahigh vacuum sputtering chamber, where $60-100\ nm$ of $Co_{70}Fe_{30}$ is sputtered at 3 mTorr argon pressure, followed by a 2 nm Al capping layer to prevent oxidation of the FM electrodes. After the deposition of the FM material, the sample is soaked in acetone for 2 hours to lift-off the pattern (removal of PMMA). The PMGI layer is removed by soaking the sample in remover PG by Microchem for 3 minutes at

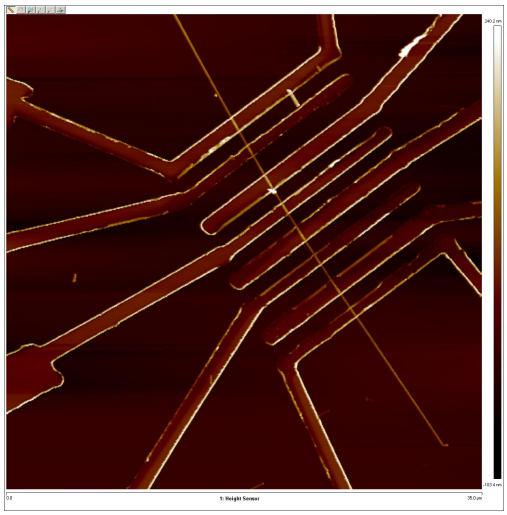

(a)

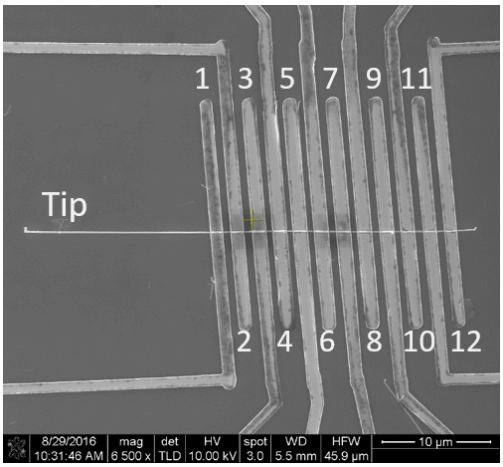

(b)

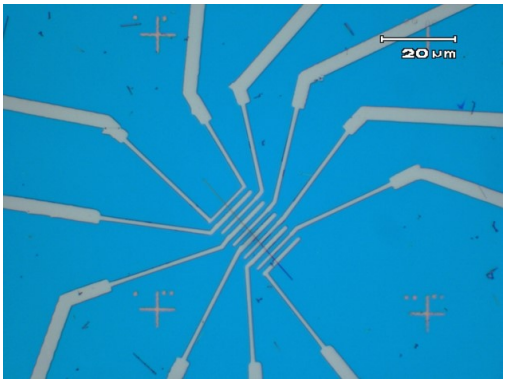

(c)

Figure 3.8: (a), (b) and (c) AFM, SEM and optical images of a single Si NW device after CoFe sputtering deposistion and lift-off process, respectively.

$80°C$, followed by thorough rinsing in IPA, DI water and drying with pure nitrogen.

Figures 3.8 (a), (b) and (c) show an AFM, SEM and optical image, respectively, of a completed device. Figures 3.7 (a), (b) indicate the good coverage of a Si NW by a 60 nm thick CoFe electrode. We can appreciate how a dome profile is formed on top of the NW, as well as relatively sharp edges after lift-off. Bilayer lithography was used during the fabrication process to significantly help the formation of sharp edges, since sputtering deposition is isotropic and sharp edges are difficult to define.

3.5 Electrostatic Discharge

Nanoscale devices are very sensitive to electrostatic discharge. Electrostatic discharge is the sudden flow of electric charge between two objects upon contact. One type of electrostatic discharge is via electrostatic induction. In this case, an electrically charged object brought in close proximity to a conductive object isolated from the ground will cause surface electric charge to redistribute. When that object comes into contact with a conducting path, the current can dissipate through the object following a low impedance path to ground. Electrostatic discharge is a well known problem in electronics, which can cause permanent damage (burning) in integrated circuits.

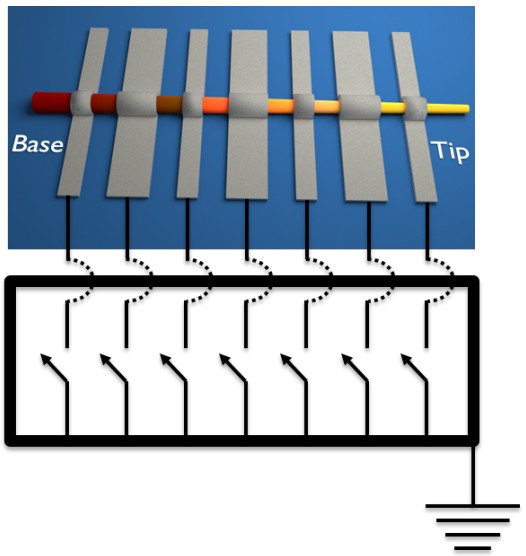

Figure 3.9: Schematics of a modified electrical box with a series of switches that allow each electrode to be grounded independently.

Our Si NW devices are extremely sensitive to electrostatic discharge, and special care during wire bonding and connecting to the measuring probe is necessary to prevent complete damage of the samples. The most sensitive region of the Si NWs is the conducting side (base), which acts as an excellent fuse due to the very low resistivity. In order to avoid electrostatic discharge effects, I implemented a number of steps to increase the device fabrication yield.

First, a special wiring box was used to connect all the electrodes to ground before wire bonding. In addition, I made sure that my body was properly grounded during the wire bonding process. Second, after wire bonding the samples were transfered and connected to the cryostat's measuring

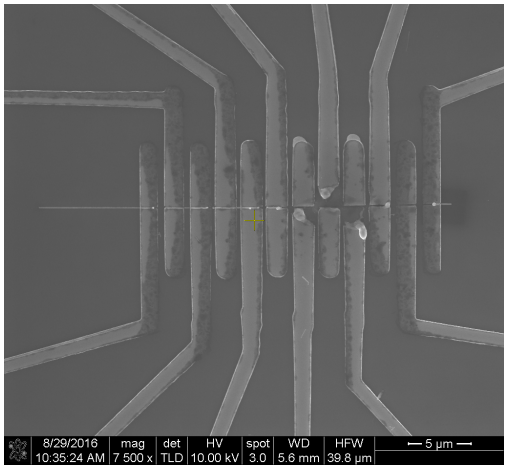

(a)

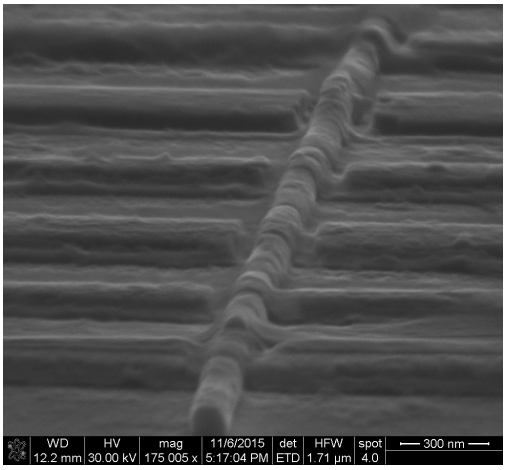

(b)

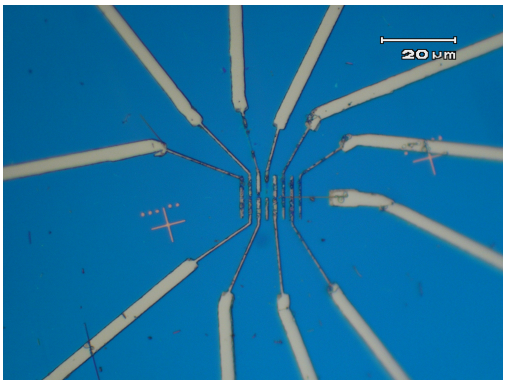

(c)

Figure 3.10: (a), (b) SEM images of a single Si NW damaged by electrostatic discharge before performing electrical measurements. (c) Optical image of a complete device suffered from electrostatic discharge.

probe. The sample was connected to ground before being disconnected from the wiring stage, and the measuring probe was grounded before connecting to the sample (I modified the probe connection box to include a series of switches that can independently connect to ground, a schematic is shown in Figure 3.9). Third, during the measurements, the sample and the electronic equipment shared a common ground to avoid any electric potential shifts.

Omitting any of the above steps would greatly increase the probability of fatal burning of the samples. Figures 3.10 (a), (b) show SEM images illustrating the effects of electrostatic discharge on a Si NW device. Figure 3.10 (c) is an optical image of a completely damaged device.

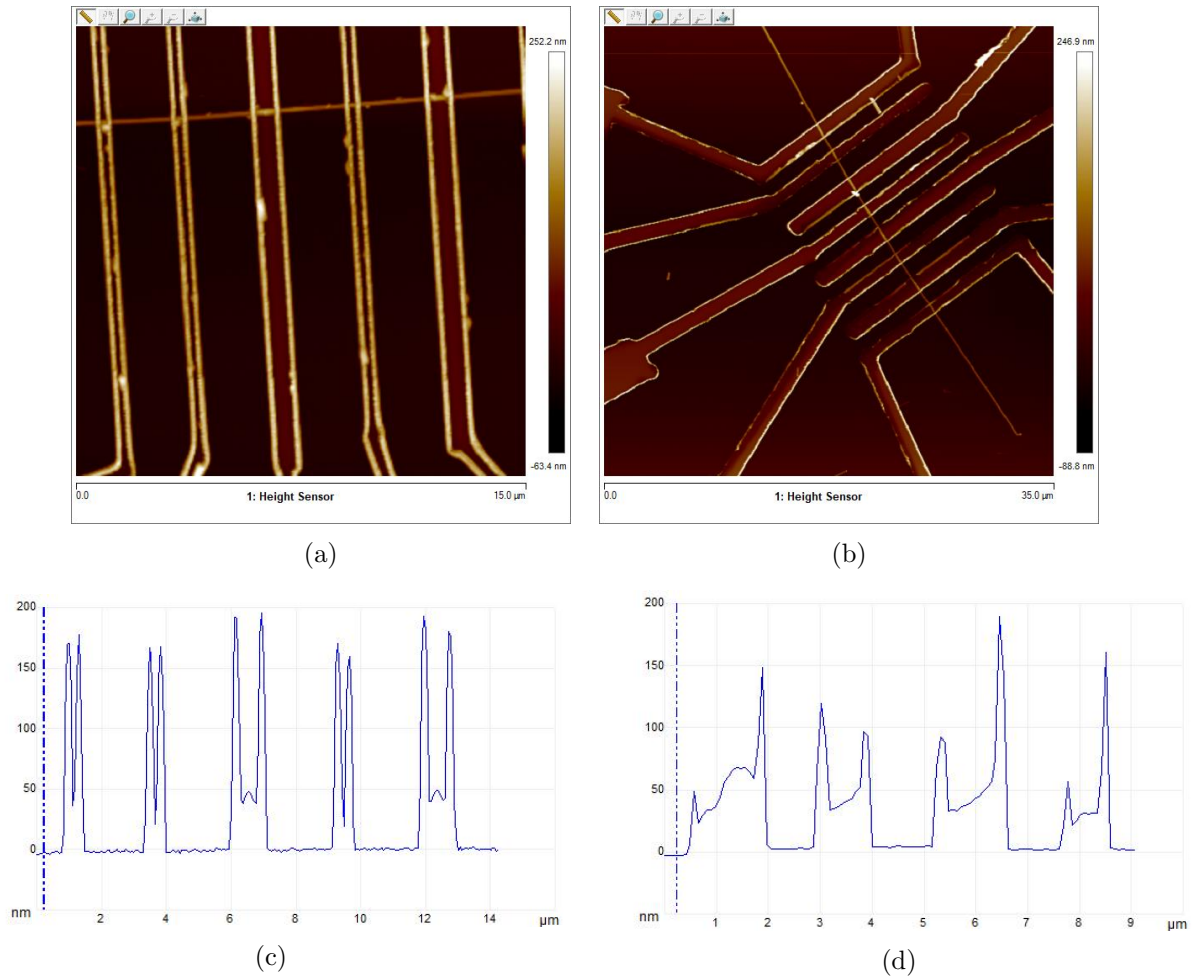

(a) (b)

(c) (d)

Figure 3.11: (a), (b) AFM images before and after changing the position of the sputtering gun, respectively. (c), (d) Depth analysis before and after changing the position of the sputtering gun, respectively. The height peaks are reduced when the gun is positioned directly under the substrate holder.

3.6 FM Electrodes

Another challenge I had to address during the fabrication of the nanodevices was the shape profile of the FM electrodes. This problem is associated with the isotropic coverage that sputtering deposition entails. Magnetron sputtering has many advantages over thermal evaporation and electron-beam evaporation, such as high deposition rates, good uniformity, high adhesion of films, excellent coverage of steps, ability to coat heat sensitive substrates, ability to sputter any metal, alloy or compound, and maintain material stoichiometry.

However, isotropic (non-directional) deposition can be an issue for nanoscale device fabrication, because small features on the order of hundreds of nanometers cannot be covered conformally. Figures 3.11 (a), (c) show an AFM picture of the sputtered FM electrodes, and the depth analysis when the sputtering gun is positioned at $\sim 45^{\circ}$ degrees angle with respect to the normal to the substrate holder plane, respectively. The edges of the FM electrodes are higher than the anticipated thickness, as indicated by the bright color, and the depth analysis show height peaks of $\sim 170\ nm$. In order to minimize this effect I decided to move the sputtering gun directly under the sample holder in order to achieve better working distance and sputtering deposition rate.

Figures 3.11 (b), (d) show an AFM picture and the depth analysis after changing the sputtering gun position. The effect was not eliminated, however, it was reduced as the depth analysis indicates that the edge heights peak have been reduced to below $\sim 150\ nm$. I would also like to point out that at the micrometer/submicrometer width scales the devices are designed for, the profile of the electrodes is not rectangular, which may have an effect on the magnetization switching properties. This is going to be further discussed in the spin transport measurements section.

3.7 Magnetic Characterization of $Co_{70}Fe_{30}$ and $Ni_{80}Fe_{20}$ Thin Films

In this section, I am going to present magnetic characterization measurements, which were performed in order to ensure the quality and the magnetic properties of the FM materials that were used for the spin injector/detector electrodes in the spin valve devices. The material that I decided to use for the spin valve devices is $Co_{70}Fe_{30}$ (permendur), however, I also tested NiFe (permalloy) FM electrodes. Both materials are categorized as soft magnetic materials. Soft magnetic materials are defined as materials with high permeability ($\mu = B/H$) in which the domain wall motion and domain magnetization rotation processes occur at weak magnetic fields, typically $H_c \leq 10^3 A/m$. In addition, both materials are also characterized as strong FMs, which means that the Fermi level lies above the top of the spin-up d-band (only the spin-down d-band has empty states). More strictly speaking, strong FMs are defined as materials where the exchange splitting is more than the energy difference between the top of the d-band and the Fermi level E_F.

I will briefly discuss two important aspects of magnetism in ultra thin films and ultra narrow elements, which are utilized for the fabrication of lateral spin valve devices, namely, the compo-

sition dependence of magnetic alloys and its effect on the magnetic properties, and the switching mechanisms in narrow nanoelements (width range 200 $nm - 2\ \mu m$).

The main concept of spin valve devices is to be able to realize two different magnetization states for the injector and detector electrodes, namely parallel and antiparallel, and a corresponding resistance change (low resistance to high resistance) upon switching between these two configurations.

One unique characteristic of FM materials is the magnetocrystalline anisotropy. Magnetocrystalline anisotropy describes the preference for the magnetization to be oriented along certain crystallographic directions, and it originates from the spin-orbit interaction, as well as chemical bonding of the orbitals of an atom with the crystalline electric field. As a result, FM materials have *hard* and *easy* axes of magnetization. The parameter that characterizes the magnetocrystalline anisotropy is called crystalline anisotropy energy, and it yields the equilibrium orientation of magnetization for different crystallographic configurations. For example, the anisotropy of a cubic system can be written as [97]:

$$u_a = K_0 + K_1(a_1^2a_2^2 + a_2^2a_3^2 + a_3^2a_1^2) + K_2(a_1^2a_2^2a_3^2) + \dots \tag{3.2}$$

where K_i are the anisotropy constants, and a_i are the direction cosines of the magnetization along the three coordinate axes.

Strong anisotropy constants are usually desirable for various applications, but for spin valve devices shape anisotropy is preferred. In order to minimize the strong effects of magnetocrystalline anisotropy in FM thin films, and take advantage of shape anisotropy, it is advantageous to choose materials with low anisotropy constants. Anisotropy constants are composition dependent, so different FM alloys have different anisotropy constants. Both iron-cobalt and iron-nickel alloys can have reduced anisotropy constant values. As the Ni or Co percentage increases, in Fe alloys the anisotropy constants decrease, and interestingly there is a change in the sign from positive to negative for the values of the K_1 anisotropy constant, at Ni (75%) and Co (45%) in Fe [97]. At that point the anisotropy vanishes. For my experiments I decided to use 30% of Co in Fe, which results in reduced magnetocrystalline anisotropy compared to pure Fe.

In order to be able to independently switch the magnetization direction of two FM electrodes, we take advantage of the thin-film magnetic shape anisotropy of the FM materials. The shape anisotropy arises from dipolar interactions. Dipolar interactions (H_{dip}) contribute to the total

anisotropy energy $G(\boldsymbol{\Omega_M})$. It turns out that the dipolar field H_{dip} experienced by a given moment $\boldsymbol{m_i}$ depends significantly on the moments located at the boundary of the sample, and this results in *shape anisotropy*. The dipolar field has contributions from the magnetocrystalline anisotropy and the shape anisotropy, but in comparatively thick films, the shape anisotropy dominates and determines the magnetization orientation.

The term of the dipolar field that is responsible for the shape anisotropy is called the demagnetizing field H_d. The demagnetizing field is the magnetic field generated by the magnetization of the material. It can be thought as the magnetic field produced by surface pseudo-charges, and it opposes externally applied magnetic fields, so that the internal field that the magnetization responds to is less than the external applied field, $H_i = H_{appl} + H_d$. The effect of the demagnetizing field is to minimize the total magnetic moment inside the sample. This results in shape anisotropy in single domain FMs, and the formation of magnetic domains and closure domains in larger FMs.

The preference of the magnetization to lie in a particular direction in a polycrystalline sample is a consequence of the shape anisotropy. The shape anisotropy energy is given by

$$G_{shape}(\boldsymbol{\Omega_M}) = -\frac{1}{2}\int_V \mathbf{M}(\mathbf{r}) \cdot \mathbf{H_d}(\mathbf{r}) dV \tag{3.3}$$

where $\boldsymbol{H_d} = -4\pi \boldsymbol{N} \cdot \boldsymbol{M}$, and $\boldsymbol{N}$ is the demagnetizing tensor, which is a function of the sample shape.

As a result, the aspect ratio (length:width:thickness) of thin films can affect the magnetic domain profiles and the magnetic switching behavior. For thin films of rectangular shapes, the shape anisotropy forces the easy axis of magnetization to be parallel to the long sides of the elements. Objects with small aspect ratios tend to form multidomain closure profiles that minimize the magnetostatic energy. However, in nanoelements with large aspect ratios (very narrow width compared to length), complete flux closure is not energetically favorable, and the elements tend to form single domain structures with small domain closures at the ends. This can drastically affect the magnetic switching behavior.

Another parameter that affects magnetic switching is the number of flat ends. It is known that needle-shaped ends affect the reversal process of magnetization [98]. Elements without flat ends have a higher switching field, because the reversal process cannot be facilitated by end domains, which in contrast are already present at remanence in flat samples. In this type of shapes the reversal

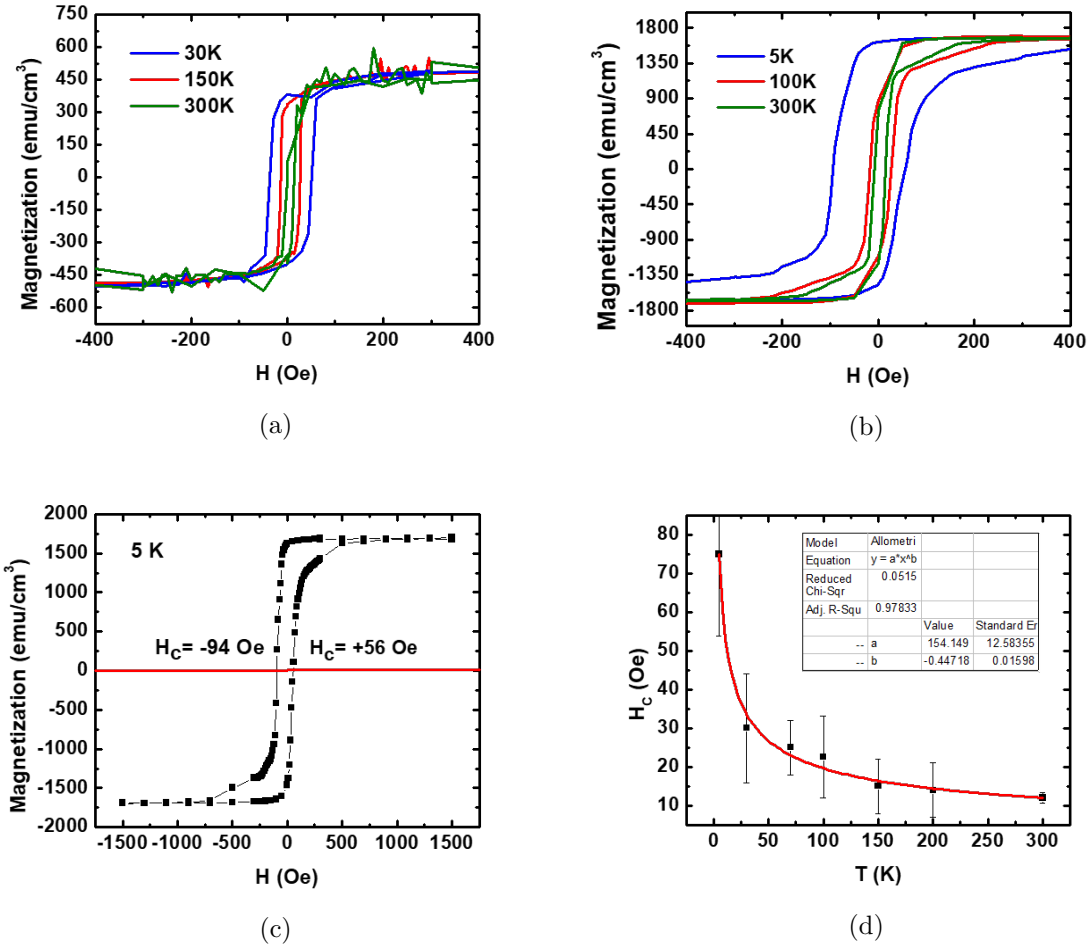

Figure 3.12: SQUID measurements. (a), (b) Magnetization curves with respect to applied field for $Ni_{80}Fe_{20}$ (40 nm thick) and $Co_{70}Fe_{30}$ (62 nm thick) thin films at different temperatures, respectively. (c) Magnetization curve for $Co_{70}Fe_{30}$ thin film at 5 K indicating the coercive field values H_C. (d) Average coercive field H_C versus temperature for $Co_{70}Fe_{30}$ 62 nm thin film. The red curve is a power law fit.

process is driven by nucleation and subsequent wall motion of magnetic regions with reversed magnetization. Non-flat ends block the formation of reversed domains and as a result have higher switching fields. I used this approach in some of my initial designs, but due to the complexity of the lift-off process I decided to use rectangular shapes with different widths.

In order to characterize the FM alloys, I performed SQUID (superconducting quantum interference device) and longitudinal magnetoresistance measurements. The SQUID measurements were performed at various temperatures between 5 K and 300 K. Figures 3.12 (a), (b) show magneti-

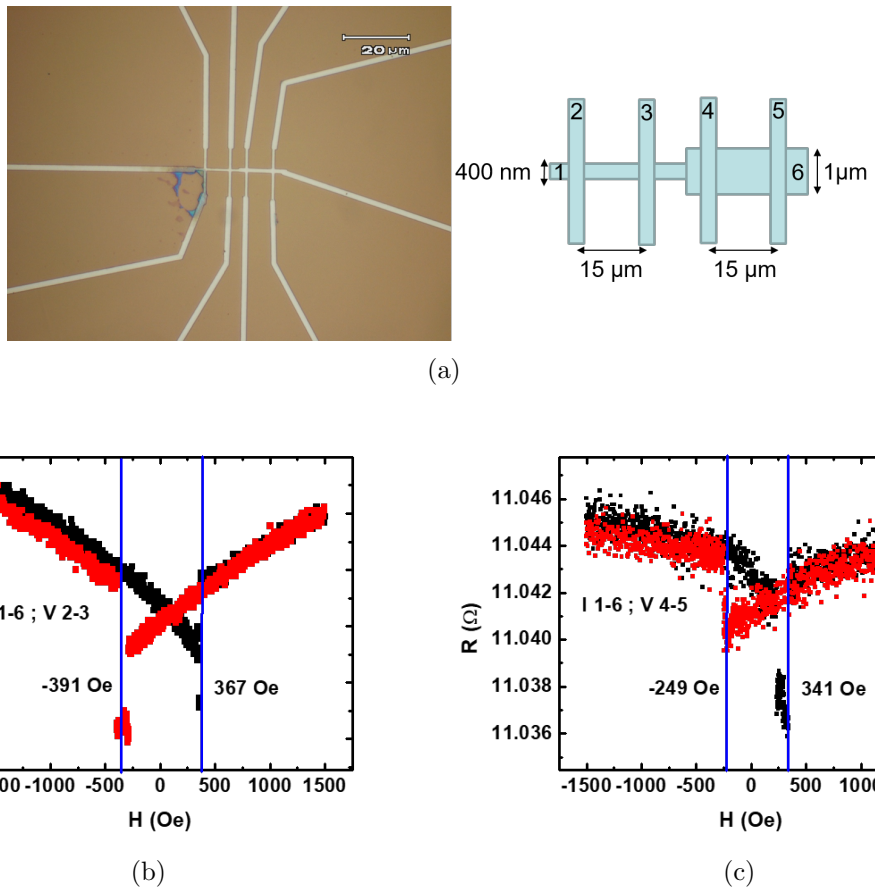

Figure 3.13: (a) Optical image and schematic for the device used for longitudinal MR measurements. (b), (c) Longitudinal MR versus applied magnetic field for the 400 nm and 1 μm wide electrode, respectively. The corresponding switching fields are indicated by the blue vertical lines.

zation hysteresis loops for $Ni_{80}Fe_{20}$ and $Co_{70}Fe_{30}$ thin films at different temperatures. We can clearly observe the square-like hysteresis loops indicating saturation along an easy magnetization axis along the film plane. For $Ni_{80}Fe_{20}$ the saturation magnetization is around 450 emu/cm^3 and for the $Co_{70}Fe_{30}$ around 1800 emu/cm^3. The $Co_{70}Fe_{30}$ has a significantly higher magnetization than $Ni_{80}Fe_{20}$, and it was chosen as the material for the Si NW spin valve devices.

Figure 3.12 (c) shows a hysteresis loop for $Co_{70}Fe_{30}$ at 5 K and the extracted coercive field values, which are $H_C = +56$ Oe and $H_C = -94$ Oe respectively. For this sample I extracted the coercive field values at different temperatures, and the results are plotted in Figure 3.12 (d). The coercive field H_C decreases with increasing temperature following a power law relation, however, there is not a theoretical model that decribes perfectly this behavior.

The longitudinal magnetoresistance measurements were performed in small $Co_{70}Fe_{30}$ electrodes at 5 K in order to check if there is any anisotropic magnetoresistance (AMR) signal, which would indicate magnetic switching of the electrodes [99]. For such small electrodes, SQUID measurement becomes ineffective. In a perfect single domain formation one should not expect to see an AMR signal since the magnetization is always parallel to the current direction. Nonuniform magnetization profiles will give rise to small nonzero AMR signals, which can provide information about the switching fields of the electrodes.

The device was prepared by electron beam lithography, and the aspect ratio of the electrodes was designed similar to the ones used for the actual spin valve devices. Specifically, as it is shown in Figure 3.13 (a), the length was $L = 15\ \mu m$, and the width was $W = 400\ nm$ and $W = 1\ \mu m$ respectively. The contact configuration for the magnetic transport measurements is also shown. The thickness of the sputtered $Co_{70}Fe_{30}$ thin film was 62 nm.

Figures 3.13 (b), (c) show the longitudinal four-terminal magnetoresistance as a function of the external magnetic field $H(Oe)$. As the external magnetic field is swept back and forth, from positive to negative, along the in-plane direction and along the length of the electrodes, the resistance drops at the points where the magnetization direction of the electrodes is reversed. We can observe that the switching points are different for the two electrodes, which can be attributed to the different widths (different demagnetization factors). As expected, the different aspect ratio affects the switching behavior, and we conlude that the narrow electrodes have higher switching fields, $H_{SW} = +367, -391\ Oe$ compared to the wider electrodes, $H_{SW} = +341, -249\ Oe$.

CHAPTER 4

ELECTRICAL AND SPIN TRANSPORT IN P-DOPED SI NANOWIRES WITH AXIAL DOPING GRADIENT

4.1 Electrical Transport Measurements

4.1.1 Schottky Tunnel Barriers

The presence of a tunnel barrier between a FM and a SC is a necessary condition to achieve efficient spin injection because of the "conductivity mismatch". Much effort has been expended in nanoscale contact engineering in order to overcome this problem. The interfaces that have been investigated are Schottky barriers (SB) [100, 18], artificial oxide tunnel barriers [19, 20], and graphene [22]. In the case of SBs for FM/SC heterostructures, a pioneering method was introduced by Hanbicki *et al.* [101] to reduce the depletion layer width and the effective barrier height. The method was to introduce a graded doping profile between the FM and the SC in order to reduce the large difference in the carrier concentrations at the FM/SC interface.

In my experiments, the contacts formed between the FMs and the Si NWs, after etching of the native oxide, are SBs. Specifically, we take advantage of the gradient doping profile along the length of a single Si NW to form SBs with different depletion layer width and barrier height. This allows us to systematically study how spin injection/extraction depends on different parameters of the FM/SC Schottky contacts on the same device.

In this section, I will discuss some of the basic characteristics of SB contacts due to their significance in our experiments. Figure 4.1 shows the energy band diagrams of a metal and a n-type SC in isolation, as well as the band diagrams when the two materials are brought in direct contact in the ideal case, without surface states or other defects. The Fermi level on both sides have to line up resulting in the band bending of the SC conduction band (CB) and valence band (VB). The work function for the metal is denoted by $q\phi_m$, the electron affinity of the semiconductor by $q\chi$, and the energy difference between the CB and the Fermi level by $q\phi_n$. In the case of $\phi_m > \phi_n$, when the two materials come in direct contact, the more energetic electrons in the SC CB diffuse

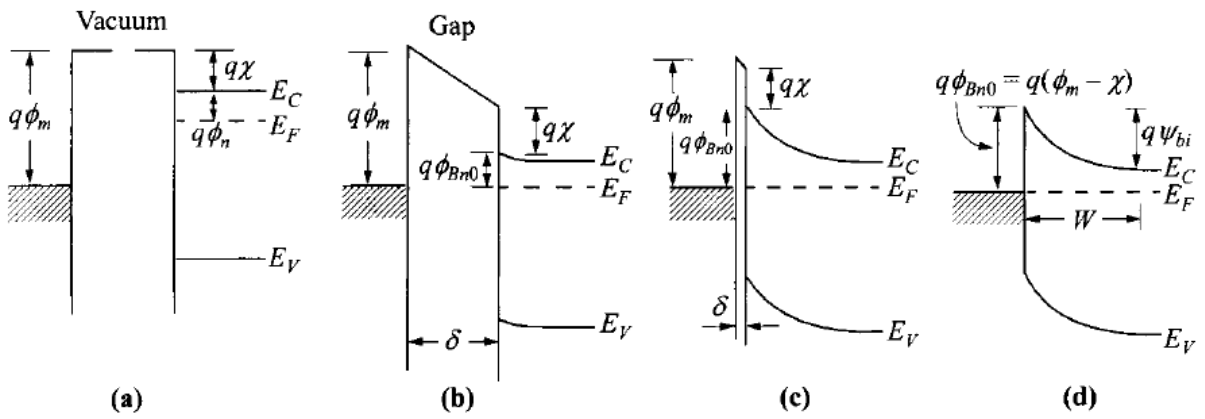

Figure 4.1: Schematic diagrams of metal-semiconductor contacts. (a) Metal and semiconductor in separated systems, and (b), (c), (d) evolution of band bending when the system is brought into contact and the gap δ is reduced to zero. Adapted from Sze [89].

into the metal lower energy empty states until equilibrium is achieved (uniform Fermi level). That process results in the formation of an electron-depleted region of width W (depletion layer width), and a built-in potential $\psi_{bi} = \phi_{Bn} - (E_C - E_F)$. The work function of the metal is equal to $q\phi_m = q(\chi + \phi_n)$. When the gap δ between the materials (see Figure 4.1 (c)) becomes comparable to the interatomic distances, we say that the SB has formed, and the barrier height is given by $q\phi_{Bn} = q(\phi_m - \chi)$ [89]. For n-type SCs, under the abrupt junction approximation (one-sided abrupt junction) the charge density is $\rho \approx qN_D$ for $x < W$, and $\rho = 0$ for $x > W$. The depletion layer width is given by:

$$W = \sqrt{\frac{2\epsilon_S}{qN_D}\left(\psi_{bi} - V - \frac{kT}{q}\right)} \tag{4.1}$$

and the maximum electric field at the interface $x = 0$ is given by:

$$E_{max} = \frac{qN_D}{\epsilon_S}W = \sqrt{\frac{2qN_D}{\epsilon_S}\left(\psi_{bi} - V - \frac{kT}{q}\right)} \tag{4.2}$$

However, these expressions have to be revised at the nanoscale dimensions that NWs offer, which is going to be briefly discussed in the next section.

Moreover, this simplistic model does not take into consideration the existense of interface states that can alter the properties of SB contacts. Interface states can also affect the spin transport

properties in spin injection experiments [102]. The ideal SB model predicts that the barrier height depends on the difference between the work function of the metal and the electron affinity of the SC. However, this is not true for a more realistic non-ideal contact. In general, the barrier height is determined by both the metal work function and the interface states that exist at the metal-SC interface. The more detailed energy-band diagram of a metal/n-type SC interface is shown in Figure 4.2. The parameter of interest is the energy level $q\phi_0$, which is called the neutral level, above which the unoccupied states are of acceptor type and below of donor type. This energy level is responsible for the "pinning of the Fermi level" close to one third of the bandgap in Si, and causes the barrier height to be less sensitive to the metal work function. The surface states result in an interface-trap charge density D_{it}, which has to be considered in the calculation of the barrier height. The full expression for the barrier height is [89]:

$$\phi_{Bn0} = \phi_m - \chi - \sqrt{\frac{2q\epsilon_S N_D \delta^2}{\epsilon_i^2}\left(\phi_{Bn0} - \phi_n - \frac{kT}{q}\right)} + \frac{qD_{it}\delta}{\epsilon_i}\left(E_g - q\phi_0 - q\phi_{Bn0}\right). \tag{4.3}$$

The Schottky diode current is composed of five different contributions: thermionic emission current, diffusion current (electrons), tunneling current, recombination, and diffusion of holes. The most important contributions in the Schottky diode current are from thermionic emission, diffusion of electrons, and tunneling. In thermionic emission, electrons in the metal acquire enough thermal energy from phonons and are able to overcome the barrier, leading to an injection current that depends exponentially on the applied voltage. For diffusion of electrons, the current also depends exponentially to the voltage similar to thermionic emission; however, the saturation current density for the diffusion theory is less sensitive to temperature variations. For tunneling, electrons quantum mechanically tunnel through the barrier, and the current density depends exponentially on the voltage and the barrier width, but is almost independent of temperature.

At room temperature (300 K), where I performed the electrical characterization measurements, the dominant contribution to the injection current is from thermionic emission of carriers, and the expression for the current-voltage relation is [89]:

$$J = \left[A^\star T^2 exp\left(-\frac{q\phi_{Bn}}{kT}\right)\right]\left[exp\left(\frac{qV}{kT}\right) - 1\right], \tag{4.4}$$

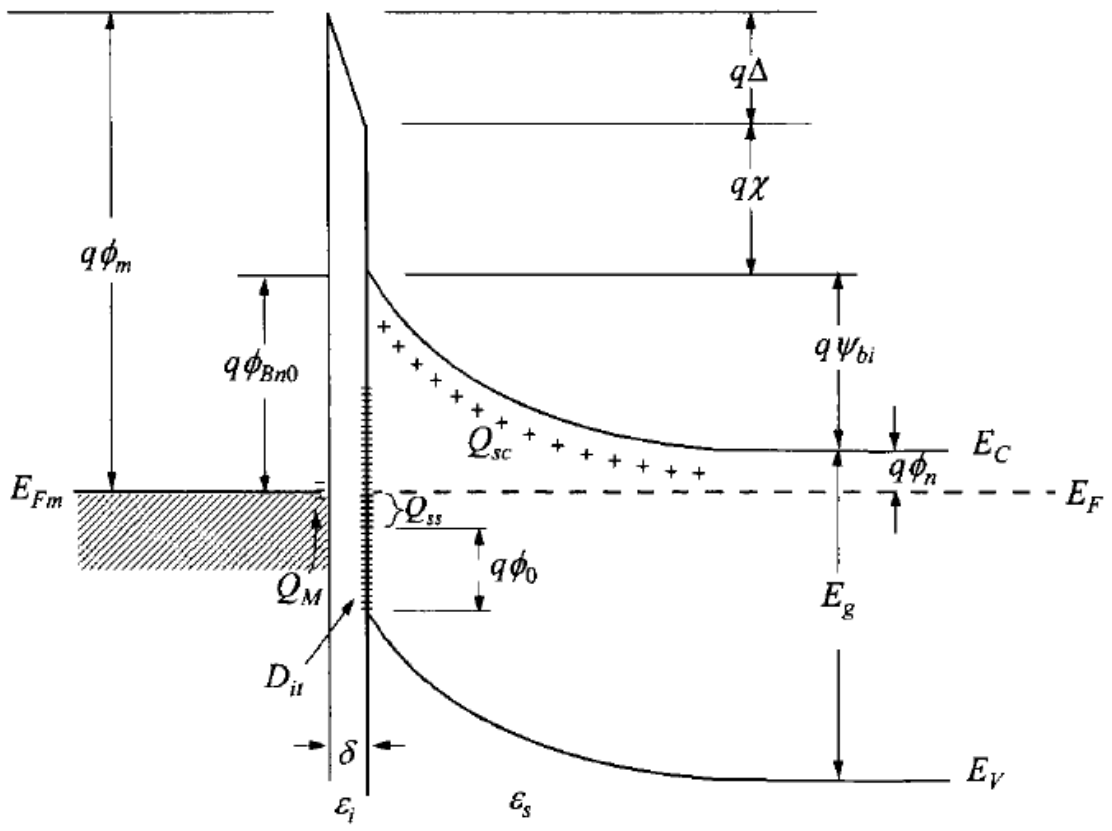

ϕ_m = Work function of metal
ϕ_{Bn0} = Barrier height (without image-force lowering)
ϕ_0 = Neutral level (above E_V) of interface states
Δ = Potential across interfacial layer
χ = Electron affinity of semiconductor
ψ_{bi} = Built-in potential
δ = Thickness of interfacial layer
Q_{sc} = Space-charge density in semiconductor
Q_{ss} = Interface-trap charge
Q_M = Surface-charge density on metal
D_{it} = Interface-trap density
ε_i = Permittivity of interfacial layer (vacuum)
ε_s = Permittivity of semiconductor

Figure 4.2: Energy band diagram of metal/n-type semiconductor contact including interface states. Adapted from Sze [89].

where

$$A^{\star} = \frac{4\pi q m^{\star} k^2}{h^3} \tag{4.5}$$

is the effective Richardson constant for thermionic emission.

For heavily doped SCs at low temperatures, tunneling is the dominant contribution to the injection current. In this study, the spin transport measurements are performed at 5 K, so current injection is via tunneling. The tunneling current is proportional to the quantum tunneling probability $T(E)$, and is given by the expression:

$$J_{s\to m} = \frac{A^{\star\star} T^2}{kT} \int_{E_{Fm}}^{q\phi_{Bn}} F_s T(E)(1 - F_m) dE \tag{4.6}$$

where F_s and F_m are the Fermi-Dirac distribution functions for the SC and the metal respectively, and $A^{\star\star}$ is the reduced effective Richardson constant. The current $J_{m\to s}$ has a similar expression, and the algebraic sum of the two gives the total current density, which has a similar expression as in the thermionic emission case. For a triangular barrier with a uniform field, the expression for the tunneling current is:

$$J = nqvT(E) \approx nqv\, exp\left(-\frac{4\sqrt{2m^{\star}} E_{barrier}^{3/2}}{3q\hbar\mathcal{E}}\right) \propto exp\left(-\phi_{Bn0}/\sqrt{N_D}\right) \tag{4.7}$$

The specific contact resistance R_C is defined as:

$$R_C \equiv \left(\frac{dJ}{dV}\right)_{V=0}^{-1}. \tag{4.8}$$

When the total current consists of both thermionic emission and tunneling currents, the current-voltage IV characteristic is combined in a single expression:

$$J = J_0 \left[exp\left(\frac{qV}{nkT}\right) - 1\right], \tag{4.9}$$

where J_0 is the saturation current density, and n is called the ideality factor. For thermionic emission processes n is close to unity, and for tunneling processes n increases.

4.1.2 Schottky Tunnel Barriers in NWs

NW devices have unique geometries and electrostatics, and as a result existing models describing the characteristics of electrical contacts made on NWs are often inapplicable [103, 104]. It is

important to try to understand the charge injection process in nanoscale devices, and how it can be different compared to bulk planar devices. For example, the most obvious differences compared to conventional planar devices is the formation of dome shaped contacts for cylindrical NWs, and more complicated structures for hexagonal NWs, as well as the high surface to volume ratio. The interface states become very important in such nanoscales for both band alignment and band bending. The simplest models for SBs assume that $\phi_B = \Phi - \chi$, where Φ is the metal work function and χ is the SC electron affinity. Surface states create allowed energy levels within the bandgap of the SC, which pin the Fermi level inside the bandgap. In bulk SCs the interface states can determine the formation of the SB. In 1D NWs, it has been studied that interface gap states have a weaker impact on the formation of the SB due to the different electrostatics at the nanoscale dimensions. It has been shown that the simple expression $\phi_B = \Phi - \chi$ describes well the experimental results in NWs [105].

Another significant difference that arises from the nanoscale geometry is that the depletion layer width is modified due to the different form of the Coulomb interaction than that in bulk systems. This gives rise to an exponential variation of the depletion layer width (and hence resistance) with dopant density, which is different from the behavior in bulk devices. Solving Poisson's equation for such geometries predicts the correct expression for the depletion layer width [103]. There are two limits that determine the correct form of the depletion layer width. In case where the radius of the NW is much larger than the depletion layer width ($R \gg W$), the expression is the same as in bulk systems:

$$W = \sqrt{\frac{2\epsilon(V_{bi} - V)}{qN_D}} \tag{4.10}$$

On the other hand, when $R \ll W$ which is the case for ultrathin NWs, the expression for the depletion layer width becomes:

$$W = R\, exp\left(\frac{4\epsilon(V_{bi} - V)}{qN_D R^2}\right) \tag{4.11}$$

The diameter of the Si NWs used in this study vary between $70 - 150\ nm$, with the base of the NW being thicker due to the VS growth. These NWs are not considered ultrathin, so Equation 4.10 was applied to estimate the depletion layer width (W).

4.1.3 2T and 4T I-V Measurements

The device used for all the conventional electrical characterizations is shown in Figure 4.3 (c). The numbering is the same for all the measurement data, starting from contact (#1) being the more resistive, and contact (#12) the most conducting. The axial doping gradient in the Si NW stems from simultaneous fast VLS axial growth and slow VS radial growth. As a consequence, the NW has a core-shell structure, resulting in unique electrical properties. The much slower VS growth rate leads to much higher density of phosphorus dopant incorporation within the shell, whereas the core is significantly lower doped. The base of the NW is more highly doped compared to the tip of the NW. The effects of the axial doping gradient can be studied by performing electrical transport measurements on the NW. The device has a series of CoFe FM electrodes, which can be used for electrical characterization measurements and spin transport measurements.

The channel and junction resistances are determined by performing 2T and 4T I-V measurements with appropriate configurations in the zero-bias regime. Figures 4.3 (a), (b) show the measurement schemes for 2T and 4T respectively, and Figure 4.3 (d) is an example of such measurements from combination #10-3 at 300 K. Figure 4.3 (e) shows the channel resistance versus temperature measurement for terminals #11-10 during the cooling down process. The resistance increases with decreasing temperature as expected for SCs. The 4T measurements provide the channel resistance (R_{ch}) directly, and the 2T measurements provide the resistance of the channel in series with the two junction resistances (R_J), thus $R_{2T} = R_{4T} + R_{J,1} + R_{J,2}$.

In order to extract the junction resistance of each electrode, I set up a system of linear equations for the different configurations. Let us examine three consecutive contacts (#1, 2, 3). We can write the following equation for a 2T I-V measurement for each combination:

$$R_{2T,ij} = R_i + R_j + R_{4T,ij} \rightarrow R_i + R_j = R_{2T,ij} - R_{4T,ij} \tag{4.12}$$

where i, j are the individual contacts. The relations for all possible combinations of three consecutive contacts are

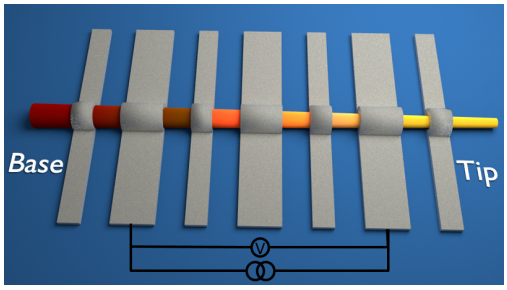

(a)

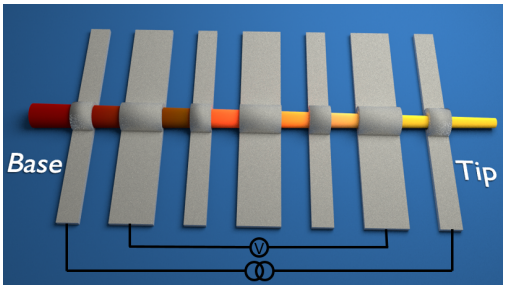

(b)

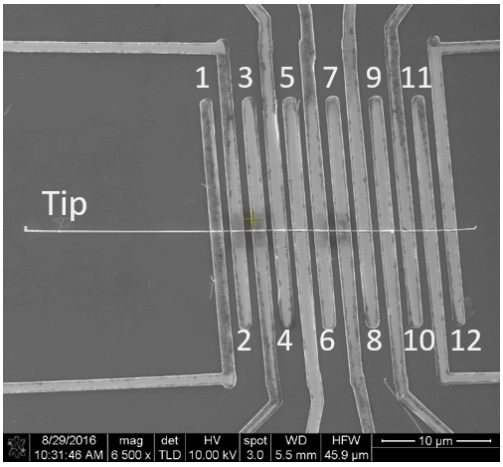

(c)

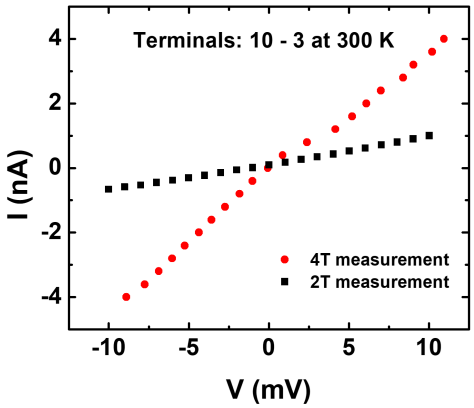

(d)

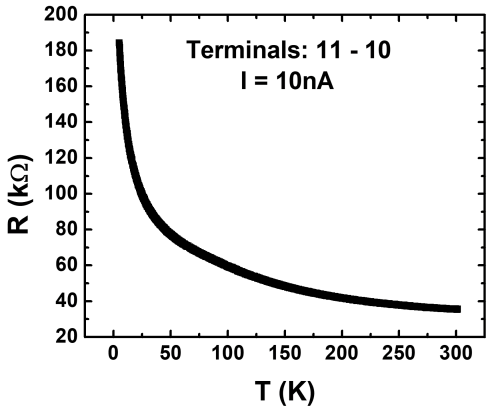

(e)

Figure 4.3: (a), (b) 2T and 4T I-V measurement schemes respectively, and (c) a typical device used for electrical characterization. The numbering refers to the CoFe electrodes. (d) I-V characteristics for 2T configuration (black) and 4T configuration (red) for the corresponding terminals (#10-3). (e) 4T resistance versus temperature curve for the corresponding terminals (#11 - 10).

Table 4.1: Channel resistances at 300 K. The distance from the tip is defined as the middle point between the electrodes.

Electrode configuration	Distance from the tip (μm)	Channel resistance (Ω)
11-10	26.8	32.3E+03
10-9	24.8	35.7E+03
9-8	22.7	45.5E+03
8-7	20.8	58.5E+03
7-6	18.8	94.4E+03
6-5	16.8	172.2E+03
5-4	14.8	55.0E+04
4-3	12.7	98.1E+04
3-2	10.6	3.27E+06

$$R_1 + R_2 = R_{2T,12} - R_{4T,12}, \tag{4.13}$$

$$R_1 + R_3 = R_{2T,13} - R_{4T,13}, \tag{4.14}$$

$$R_2 + R_3 = R_{2T,23} - R_{4T,23}. \tag{4.15}$$

The differences on the right hand side of Equations 4.13 - 4.15 are what is measured experimentally. By defining $R_{i-j} = R_{2T,ij} - R_{4T,ij}$ as the difference between the experimentally measured 2T and 4T resistances, the solutions to the equations yield the junction resistances for each individual contact

$$R_1 = \frac{R_{1-2} + R_{1-3} - R_{2-3}}{2}, \tag{4.16}$$

$$R_2 = \frac{R_{1-2} + R_{2-3} - R_{1-3}}{2}, \tag{4.17}$$

$$R_3 = \frac{R_{1-3} + R_{2-3} - R_{1-2}}{2}. \tag{4.18}$$

Table 4.1 lists the channel resistances for each segment of the Si NW at 300 K. The distance is measured from the tip of the NW (low doping region), to the middle point between two adjacent electrodes. The values were obtained from 4T measurements except for the last four which where extracted by subtractions of other combinations. For example, the channel resistance #6-5 was obtained by subtracting the channel resistance of #7-6 from #7-5. The measurements in the insulating part of the NW have very high noise, and it is difficult to directly extract the low

Table 4.2: Channel resistances at 5 K. The distance from the tip is defined as the middle point between the electrodes.

Electrode configuration	Distance from the tip (μm)	Channel resistance (Ω)
11-10	26.8	180.1E+03
10-9	24.8	469.1E+03
9-8	22.7	1.66E+06
8-7	20.8	3.68E+06
7-6	18.8	2.20E+07
6-5	16.8	4.01E+07

Table 4.3: Junction resistances at 300 K.

Pin number	Distance from the tip (μm)	Junction resistance (Ω)
11	27.8	3.35E+03
10	25.9	1.65E+0.3
9	23.7	4.25E+03
8	21.8	9.85E+03
7	19.8	8.35E+03
6	17.8	68.25E+03
5	15.9	30.91E+04
4	13.8	1.80E+06
3	11.6	1.31E+07
2	9.5	5.60E+07

bias resistances. Similarly, Table 4.2 shows the channel resistances at 5 K for the same Si NW. Due to the significant increase of the resistance at low temperatures, the configurations that were measurable with our electronic equipment are limited to combination #6-5. Tables 4.3 and 4.4 list the calculated values for the individual junction resistances by using the method described above at 300 K and 5 K, respectively.

In order to appreciate the evolution of the axial doping gradient along the axial direction, the data are plotted in Figure 4.4. Specifically, the junction resistances (R_J) and channel resistances (R_{ch}) are plotted with respect to the distance from the tip of the NW. Figures 4.4 (a), (b) show the results at 300 K and 5 K, respsectively. It is evident that both R_{ch} and R_J vary exponentially along the axial direction. Note that the y-axis is in logarithmic scale. The junction resistance changes by 5 orders of magnitude, and the channel resistance changes by 3 orders of magnitude over 25 μm

Table 4.4: Junction resistances at 5 K.

Pin number	Distance from the tip (μm)	Junction resistance (Ω)
11	27.8	35.65E+03
10	25.9	12.00E+04
9	23.7	18.57E+04
8	21.8	5.02E+06
7	19.8	1.01E+07
6	17.8	3.51E+08
5	15.9	2.10E+09

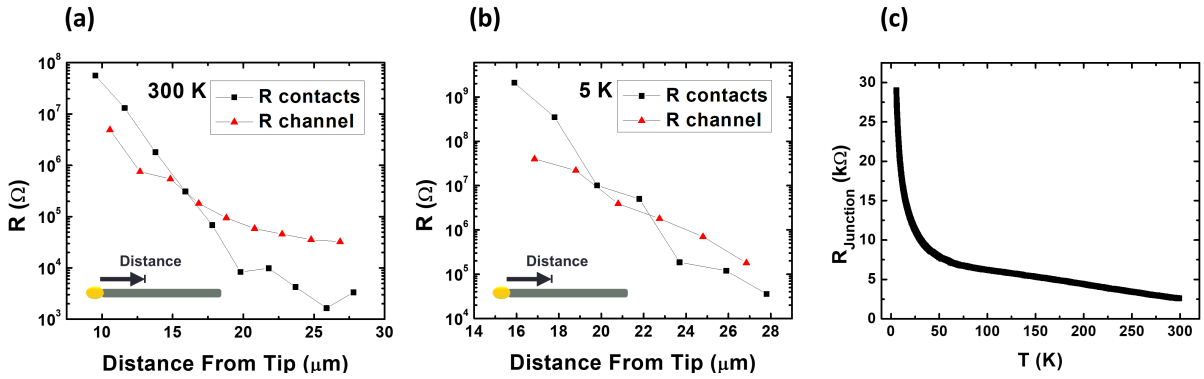

Figure 4.4: (a), (b) Extracted contact and channel resistances, from the device used for electrical characterization, with respect to the distance from the tip of the NW at 300 K and 5 K, respectively. (c) three-terminal measurement of junction resistance as a function of temperature for one contact.

along the NW. It is worth noting that at approximately 16 μm from the tip of the NW, there is a transition from a SB-dominated behavior to a channel-limited Ohmic behavior indicated by the crossing of the two curves.

Figures 4.5 (a), (b), and (c) show the 2T I-V curves for different combinations starting from the most conducting pair (#11-12) toward the most insulating pair (#1-12), while keeping the source electrode the same (#12), at 300 K. The common source electrode is the most linear (Ohmic) and lowest resistance contact available in the device (base of the NW). The 2T I-V evolves from linear at the base of the NW to non-linear closer to the tip. It is interesting to observe that the non-linear behavior represents a single SB contact, which can be analyzed within the thermionic emission model. The fitting results are presented in the following section.

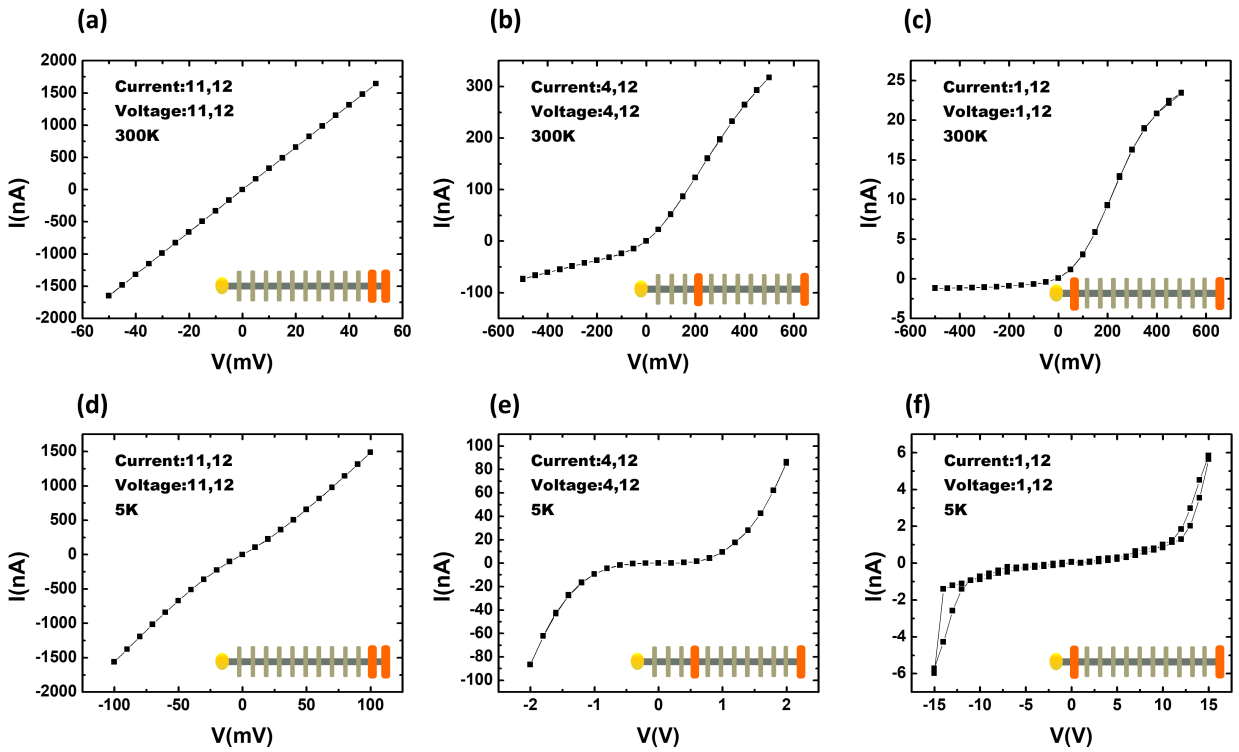

Figure 4.5: (a), (b), (c) Current-voltage (I-V) characteristic curves at 300 K for different electrode combinations starting from the most conducting pair toward the most insulating pair, respectively. As it is shown in the schematic insets, the source electrode is kept the same (#12) for all the measured configurations, and it corresponds to the most linear (Ohmic) contact (base of the NW). There is an apparent transition from linear to non-linear behavior as the drain electrode moves closer to the tip of the NW (gold droplet). (d), (e), and (f) Similar measurements at 5 K, showing similar evolution.

Similarly, Figures 4.5 (d), (e), and (f) show a transition from an almost linear to a non-linear behavior for the same configurations at 5 K. These plots are symmetric, suggesting the formation of thin SBs, and that the tunneling mechanism dominates the current flow. One way to verify that at low temperatures tunneling is the dominant current injection mechanism is to measure the temperature dependence of the junction resistance [89]. The relatively weak temperature dependence of the junction resistance $R_J(T)$, which is measured in a 3T configuration, and is shown in Figure 4.4 (c) corroborates the above statement.

The resistivity, $\rho = (R \cdot A)/L$, where A, L are the cross-section and length of the NW, for the first 8 electrode configurations (from the base toward the tip) varies between 0.009 $\Omega \cdot cm$

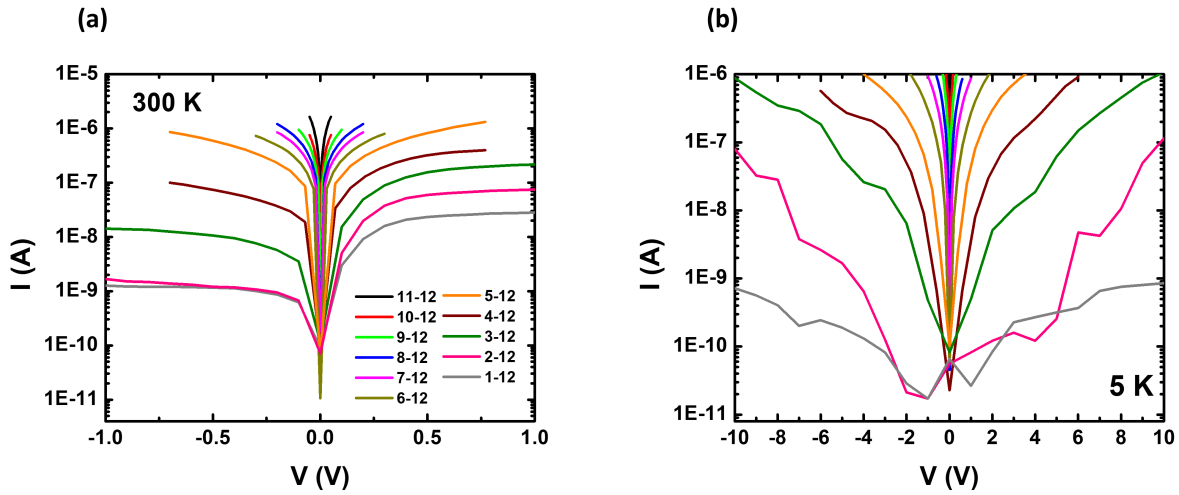

Figure 4.6: (a), (b) Semi-Log 2T I-V curves for a Si NW with multiple electrodes along its length at 300 K and 5 K respectively. The color and electrode numbering for the two graphs is identical.

to 0.027 $\Omega \cdot cm$ at 300 K. This change corresponds to an effective carrier concentration between 4.5×10^{18} cm^{-3} and 6.8×10^{17} cm^{-3} when infered from bulk Si values at 300 K. This indicates a transition from a moderately-doped to a low-doped regime. It should be pointed out that these values are the extracted effective carrier densities, which can be different from the actual doping levels within the shell of the Si NW. This will be important during the discussion of the spin transport measurements. It has been shown by pulsed laser atom probe tomography experiments that the doping concentration within the shell can be more than one order of magnitude higher than the effective carrier density values [95].

Lastly, to have a complete picture of how different types of contacts can be formed along the axial direction of a single Si NW, Figures 4.6 (a), (b) show the semi-log 2T I-V curves for twelve consecutive electrodes at 300 K and 5 K, respectively. At 300 K, starting from combination (#1-12) we clearly see the asymmetry between negative and positive voltage biases, and how the curves become symmetric after combination (#5-12). At 5 K, all the curves show symmetric behavior due to the domination of tunneling through the SBs.

Another approach to determine the junction resistance for the electrodes along the length of a NW, after it has been characterized, is to fit the results in Figure 4.4 (a) and (b) with an exponential function. A lot of Si NWs were characterized, and their behaviors were identical so this can serve

as a very beneficial and valid method to extract information about the position dependence of the junction resistance. At 300 K, the exponential fitting is:

$$R_J(\Omega) = 4.98 \times 10^{10} \exp(-0.712 \cdot L) - 125.04 \times 10^3 \tag{4.19}$$

where L is the distance from the tip of the Si NW in μm. Similarly, at 5 K the expression is:

$$R_J(\Omega) = 7.42 \times 10^{15} \exp(-0.948 \cdot L) - 7.34 \times 10^6 \tag{4.20}$$

4.1.4 Thermionic Emission Model

The room temperature data can be further analyzed within the thermionic emission model to elucidate key characteristics of the SBs. As it was shown previously, the I-V characteristic for a combination between an electrode at the base (#12) and an electrode at the tip of the NW (#1) follows the behavior of a single SB, so they can be fitted directly to the thermionic emission model (Equation 4.4). However, if a more realistic model that includes a resistor in series with one Schottky contact is used [106, 107]. The thermionic emission current is:

$$I = I_0 \left[\exp\left(\frac{q(V - IR_S)}{nk_BT} \right) - 1 \right] \tag{4.21}$$

where n is the ideality factor, R_S is the serial resistance, and I_0 is the saturation current at negative voltage bias

$$I_0 = SA^\star T^2 \exp\left(-\frac{q\phi_B}{k_BT} \right) \tag{4.22}$$

The serial resistance represents the channel resistance (Si NW). The ideality factor describes whether the dominant contribution of the current arises from thermionic emission ($n \sim 1$), or other current mechanisms, such as tunneling, contribute significantly ($n > 1$). Equation 4.21 is a transcendental equation. In order to fit the experimental data, the closed-form of the voltage (V) with respect to the current (I) is used

$$V(I) = I \cdot R_S + \left(\frac{nk_BT}{q} \right) \log\left(\frac{I + I_0}{I_0} \right) \tag{4.23}$$

Figure 4.7 presents the I-V characteristics for the most Ohmic pair in the device (#11-12) and the most non-linear Schottky pair (#1-12) at 300 K. The solid black line is the fitting of the latter to the thermionic emission model. The deviation at large positive bias voltage is due to the pinch-off of the channel; these points were not considered for the fitting. The resulting values for

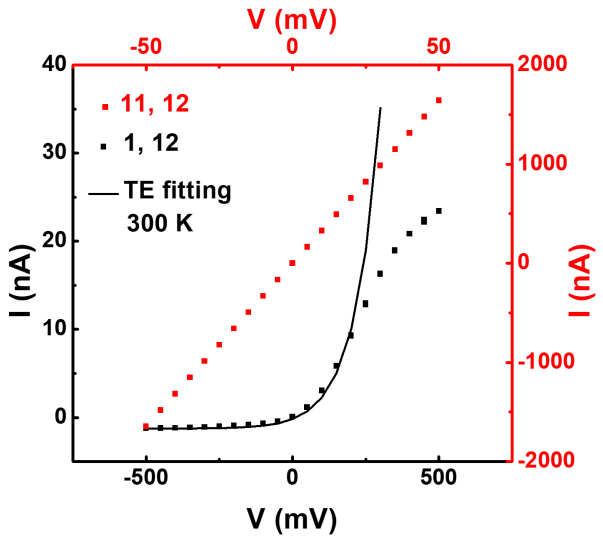

Figure 4.7: 2T I-V characteristics from two different combinations of the most conducting electrode (#12) with the closest (#11) and furthest (#1) electrode. The solid line represents the thermionic emission model fitting.

the SB height, serial resistance and ideality factor are $\phi_B = 0.453\ eV$, $R_S = 12.7\ M\Omega$ and $n = 1$, respectively. The ideality factor shows that the behavior is that of an ideal SB. The experimentally determined channel resistance for combination (#2-11), which corresponds to the longest channel that was measured, is $R_{4T,2-11} = 7.4\ M\Omega$. The extracted serial resistance for combination (#1-12), $R_{4T,1-12} = 13\ M\Omega$, is higher as expected, and it is consistent with the evolution of the doping profile along the Si NWs.

Based on additional electrical measurements, which were performed on Si NWs from the same growth, with non-magnetic metallic silver (Ag) contacts, by other members in my research group, there is an increase in the effective SB height concurrent with the axial doping gradient along the length of the NWs. The SB heights in those devices vary from ~ 0.210 eV to ~ 0.520 eV within 10 μm of the Si NWs length [108].

In conclusion, the electrical transport measurements yield results consistent with the unique doping profile of the Si NWs. Specifically, they provide direct evidence that different types of contacts are formed along the axial direction of the Si NWs due to the graded doping profile. The formation of SBs with different widths and heights on a single Si NW is a tremendous advantage that is going to be exploited during the electrical spin transport measurements.

4.2 Spin Transport Measurements

Performing electrical measurements of spin transport is one way of examining spin transport and spin coherence in a SC as a function of different material parameters. In addition, they could offer useful insight in the spin relaxation processes that take place within a SC, as well as at the FM/SC interface. The other way of studying coherence and transport is by optical pumping (optical excitation using circularly polarized light) [44, 90]. However, electrical measurements are very important if we want to develop devices with spin functionality, and explore a much broader range of technologies than those allowed by optical excitations [70, 91, 11].

Generally, in electrical spin transport experiments, one contact defines the spin injector, and another contact defines the spin detector. This is the case for nonlocal measurements, whereas for local measurements each contact acts as a spin injector and detector simultaneously. The contacts, which are readily scalable, set the dimensionality parameters of the interface. A magnetic material acting as an injector/detector is a necessary condition for injecting/detecting spin-polarized current through an interface. FM metals (Co, Ni, Fe), concentrated ferromagnetic SCs (EuS, EuO), diluted magnetic SCs ($Ga_{1-x}Mn_xAs$, etc.), and half metals (Heusler alloys, Co_2FeSi, etc.) are examples of such materials. Magnetic materials have a spin-polarized band structure and density of states (DOS). This means that at the Fermi level, E_F, there is a net spin polarization because the DOS is different for spin-up and spin-down bands, which is caused by the exchange interaction. Recall that the spin polarization is defined as:

$$P = \frac{N_\uparrow(E_F) - N_\downarrow(E_F)}{N_\uparrow(E_F) + N_\downarrow(E_F)} \tag{4.24}$$

where $N_\uparrow(E_F), N_\downarrow(E_F)$ are the density of states at the Fermi level for spin-up and spin-down bands, respectively.

4.2.1 Measurement Schemes for Spin Transport

In this section, I will describe the measurement setups for three different types of measurements that are commonly used for electrical spin transport experiments, namely, the local 2T spin valve, the nonlocal 4T (NL 4T) spin valve, and the three-terminal 3T Hanle effect. In order to perform spin transport measurements, the sample is attached on a 14-pin plug, and then it is wire-bonded with aluminum wire (after the lift-off process). The next step is to load the sample on a custom-made rotational probe, which has a Hall sensor that acts as an angle position sensor. Figures 4.8

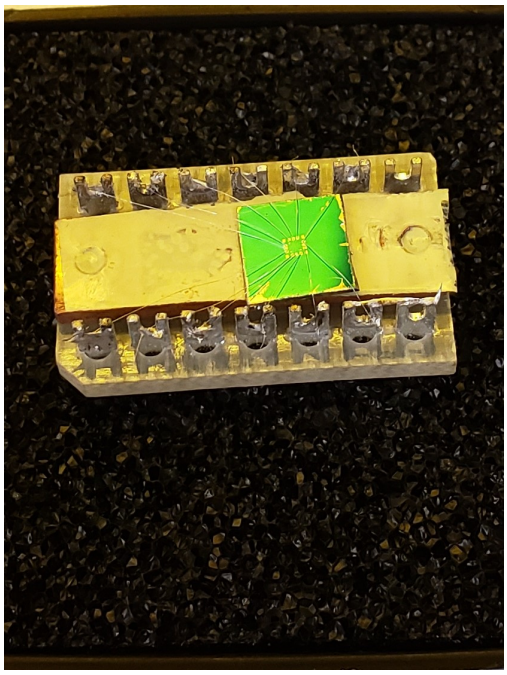

(a)

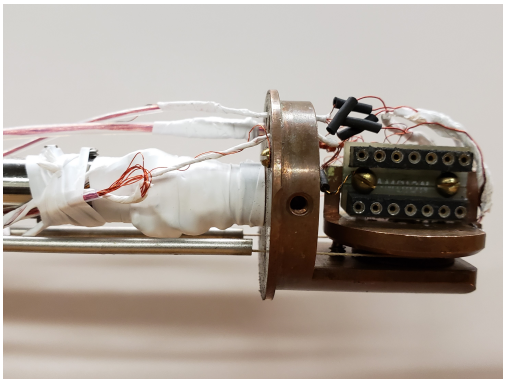

(b)

Figure 4.8: (a) Photograph of a device wired up to a 14 pin electrical plug. (b) Photograph of the rotation probe.

(a) and (b) show pictures of a wired-up Si NW device and the rotation probe, respectively. The probe is loaded inside a Helium-4 varytemp cryostat. This type of cryostat allows for electrical and magnetotransport measurements over a wide range of temperatures (5 - 320 K) and external magnetic fields (0 - 80,000 G). For spin valve measurements, the sample is oriented with the magnetic easy axis of the FMs (along the length of the electrodes) parallel to the external magnetic field direction, which enables switching of the relative orientation of the magnetization of the FM electrodes.

The sample is first cooled down to 5 K in the dark, and the FM electrodes are magnetized along their easy axis by applying a large external magnetic field. Then local and nonlocal spin-valve measurements are performed. For Hanle measurements, the sample is rotated so that the in-plane magnetization vector is perpendicular to the applied external magnetic field. The measurements are performed for different combinations of FM electrodes (different SBs) in order to systematically examine the dependence of the spin signals on the nature of the FM/SC nano interface. The measurements are perfomed with an AC lock-in technique at low frequency (17 Hz), as well as

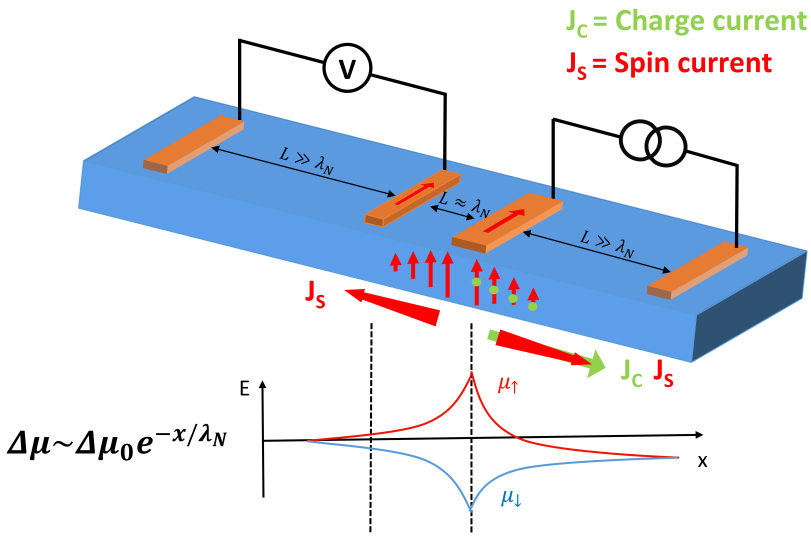

Figure 4.9: Schematic of the spin diffusion process in a lateral spin valve geometry. Spins diffuse isotropically away from the injector electrode (spin current), and decay exponentially inside the channel. Charge current flows only inside the closed circuit loop. The energy diagram represents the chemical potential splitting between the spin-up and spin-down subbabnds, and how the spin accumulation decays with respect to the distance, x, from the injection point.

with a DC current source and a DC voltmeter when noise levels are not too high. Phase-sensitive detection (lock-in amplifier) is prefered because the spin signals are very small ($\sim 1-100\ \mu V$), and they can be obscured by electronic noises.

Spin valve measurements: physical interpretation.

Similar to the definition of spin polarization, the difference of the current between parallel and antiparallel spin states determine the spin polarization of the current (SP). The spin polarization of the current is defined as

$$SP = \frac{I_{\uparrow\uparrow} - I_{\uparrow\downarrow}}{I_{\uparrow\uparrow} + I_{\uparrow\downarrow}} \tag{4.25}$$

where $I_{\uparrow\uparrow}$ and $I_{\uparrow\downarrow}$ are the spin currents for the parallel and antiparallel magnetization configurations, respectively.

It is very common to calculate the magnetoresistance signal, $\Delta R/R = (R_{\uparrow\uparrow} - R_{\uparrow\downarrow})/R_{\uparrow\uparrow}$, from spin valve measurements. MR refers to a change from a low resistance to a high resistance state upon switching the relative direction of the FM layers between parallel and antiparallel configurations.

In lateral spin valve measurements, one FM electrode acts as a spin injector and another FM electrode as the spin detector. As was described in Chapter 2, at the FM/SC interface there exists a non-equilibrium spin population, specifically a chemical potential splitting between spin-up and spin-down subbands. This splitting is called "spin accumulation", $\Delta\mu(x) = \mu_{\uparrow}(x) - \mu_{\downarrow}(x)$, and it translates to a spin polarized current ($I_{\uparrow\uparrow}$ or $I_{\uparrow\downarrow}$). The spin polarized current is injected inside the channel at the FM/SC interface, and the spins diffuse inside the channel isotropically in all directions, while charge current is confined in a closed circuit loop. The spin accumulation decays exponentially inside the channel, $\Delta\mu(x) = \Delta\mu_0\ exp(-x/\lambda_N)$, due to spin relaxation, with a characteristic spin diffusion length (λ_N), which depends on the material properties. In case the FM detector is placed close enough ($\sim \lambda_N$) to the FM injector, an open circuit voltage, which is proportional to the chemical potential splitting, can be detected. The open circuit voltage is measured experimentally, and it corresponds to the spin signal. Figure 4.9 shows a schematic representation of the spin diffusion process in a lateral spin valve setup, and how the spin accumulation decays away from the injection point. The direction of flow for the charge current and the spin current is indicated by green and red arrows, respectively.

The theoretical models that describe spin injection, spin detection, and spin transport suggest that the spin signal is expected to be bipolar, depend on the relative orientation of the magnetizations of the injector and detector electrodes, and decay exponentially as the spins diffuse inside the channel according to equation [53]:

$$\frac{V_{NL}}{I_{inj}} = \pm P_{inj} P_{det} \frac{\rho \lambda_N}{2S} e^{-x/\lambda_N} \tag{4.26}$$

where P_{inj}, P_{det} are the effective interfacial spin polarizations at the injector and detector respectively, λ_N is the spin diffusion length, ρ is the channel resistivity, and S is the cross-sectional area of the channel. A measurement of the spin signal with respect to the distance between the injector and the detector yields the spin diffusion length, and the spin lifetime via $\lambda_N = \sqrt{D\tau_s}$. In order to extract the spin diffusion length from Equation 4.26, proper values for the interfacial spin polarizations at the injector/channel and detector/channel interfaces are needed. In case that the spin diffusion length is already known for the system, information about the interfacial spin polarizations can be extracted, which is the approach that I am going to implement for my data analysis.

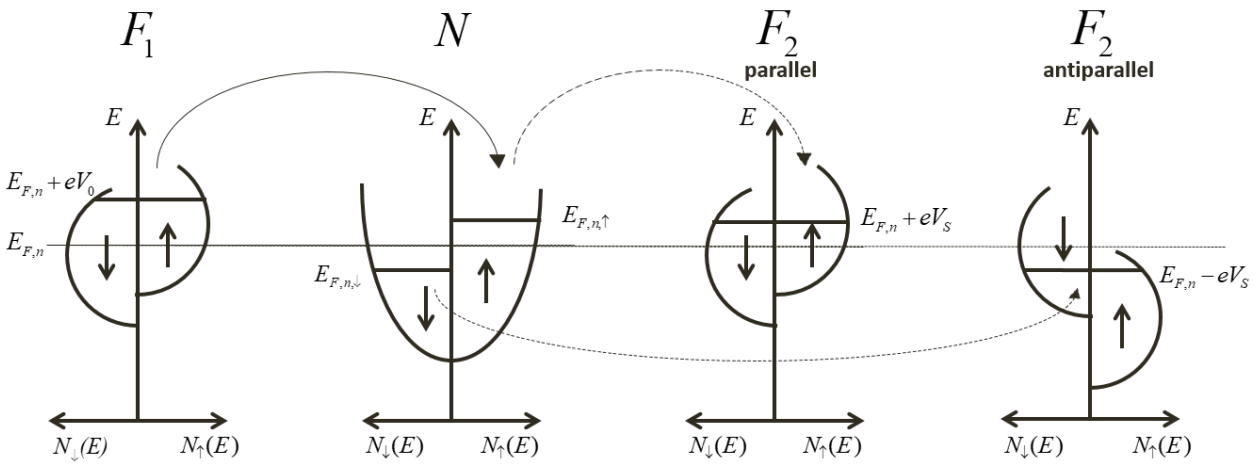

Figure 4.10: Simplified density of states diagrams for the description of the spin valve effect. F_1 represents the spin injector, N represents the nonmagnetic channel, and F_2 represents the spin detector. We can observe the splitting of the two spin sub-bands in the DOS diagram for N. When F_1 and F_2 are parallel (antiparallel) to each other a positive (negative) voltage is developed at the N/F_2 interface denoted by V_S. Experimentally, $\Delta V_S = 2V_S$ is the open circuit voltage measured nonlocally at the detector after switching the magnetization direction from parallel to antiparallel. This open circuit voltage represents the nonequilibrium magnetization signal due to the spin accumulation at the F_1/N interface. Reproduced from [58].

Figure 4.10 shows a pedagogical simplified density of states diagram which describes the nonlocal spin valve effect [58]. In the schematic, F_1 represents the spin injector, N represents a nonmagnetic channel, and F_2 represents the spin detector. At the F_1/N interface there is spin accumulation, which is shown as a splitting of the two spin sub-bands in the DOS diagram for the transport channel N. When F_1 and F_2 are parallel (antiparallel) to each other, a positive (negative) voltage is developed at the N/F_2 interface denoted by V_S. Experimentally, $\Delta V_S = 2V_S$ is the open circuit voltage measured nonlocally at the detector after switching the relative magnetization direction of the FMs from parallel to antiparallel. This open circuit voltage represents the nonequilibrium spin signal due to the spin accumulation at the F_1/N interface: As shown in the schematic, for the detection process the Fermi level of the detector aligns with the spin-up band of N for the parallel magnetization state, and with the spin-down band of N for the antiparallel magnetization state.

This simplified model assumes that the spin polarizations of the injector and the detector are the same, which does not always hold true. In addition, I would like to point out that these devices have asymmetric interfaces due to the formation of different SBs along the length of the Si NWs, so

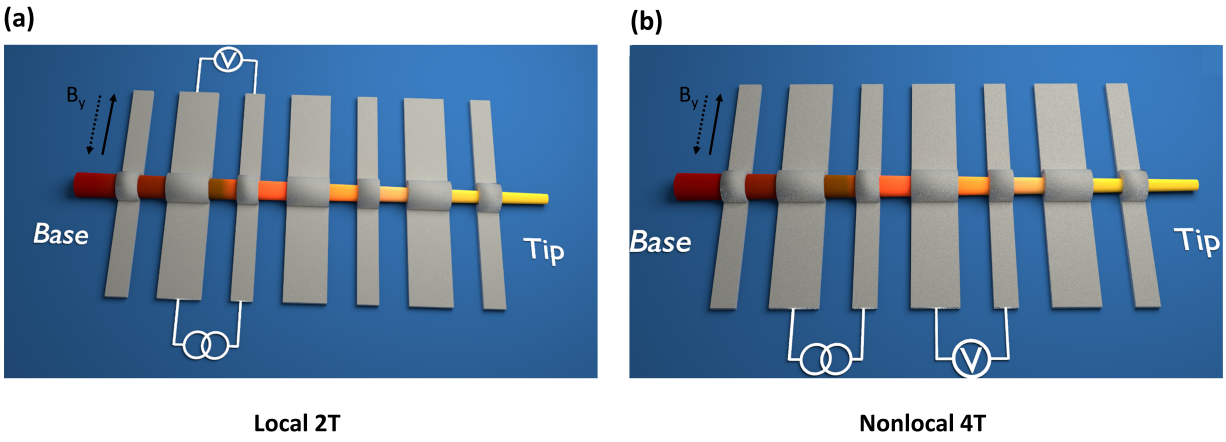

Figure 4.11: (a) Schematic for 2T local spin valve measurement. (b) Schematic for 4T nonlocal measurement. An external magnetic field B_y is applied in-plane and parallel to the easy magnetization axes of the FM electrodes. The external magnetic field is represented by the black arrows.

in this case we are actually dealing with a system that intrinsically breaks the symmetric character of the theoretical model.

The local 2T spin valve effect follows the same physical description as the nonlocal 4T spin valve effect, with the only difference being that both electrodes in the closed circuit act simultaneously as spin injector and detector. However, the local geometry introduces carrier drift effects due to the applied electric field, which affect the spin diffusion process [109, 110, 111, 112]. The description of the local 2T spin valve and the correlation with the nonlocal 4T spin valve, the effect of carrier drift, the parameters that can affect the spin polarization of the injector/detector, and the implications of the asymmetric interfaces, are going to be discussed further in the following sections.

In a typical lateral spin valve setup (2T local or 4T nonlocal), an in-plane magnetic field is applied along the easy axis of magnetization of the FM electrodes, and swept from negative to positive values and back, in order to switch their relative orientation and realise parallel and antiparallel configurations, and as a result extract the spin signal, ΔV_S (open circuit voltage). Figures 4.11 (a), (b) show the measurement schemes for 2T local and 4T nonlocal spin valves, respectively. In both figures, the directions of the external magnetic field are indicated with the black arrows.

Figures 4.12 (a), (b) show typical 2T local and 4T nonlocal spin valve signals respectively determined with AC lock-in measurements. These signals are extracted from the same transport

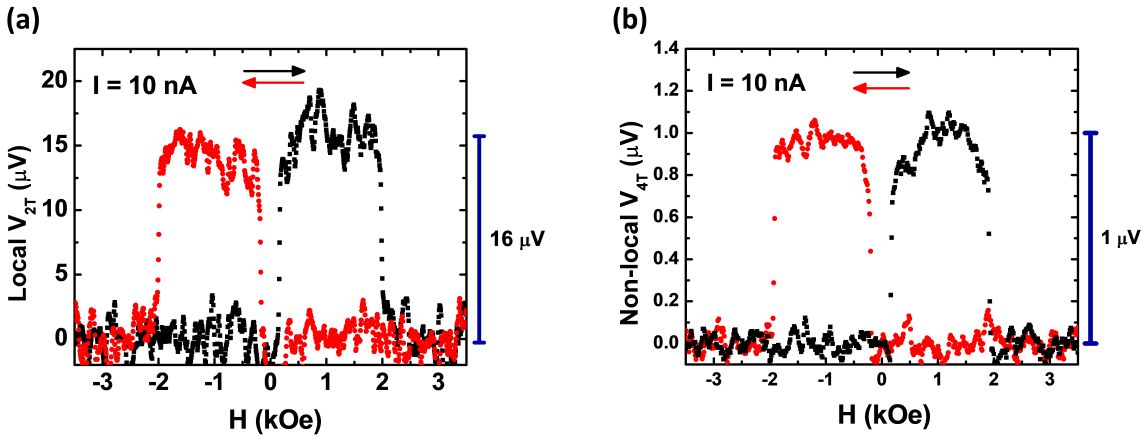

Figure 4.12: (a) and (b) Local 2T and nonlocal 4T spin valve signals for the same Si NW channel at current bias $I = 10\ nA$. The black and red arrows correspond to the sweeping of the external magnetic field from $-3000\ Oe$ to $+3000\ Oe$.

channel of a Si NW. The black and red arrows indicate the sweeping direction of the external magnetic field between $-3\ kOe$ and $+3\ kOe$. Around $H = \pm 210\ Oe$ the measured voltage increases, which corresponds to the change from parallel to antiparallel magnetization configuration. At $H = \pm 2000\ Oe$ the measured voltage decreases, which corresponds to the change from antiparallel to parallel configuration. Both the black and red curves, for the local 2T and nonlocal 4T measurement schemes, have similar switching points. The amplitude of the signal is $\sim 16\ \mu V$ and $\sim 1\ \mu V$ for the local and nonlocal measurements, respectively.

Nonlocal measurements are particularly useful, and have proved powerful for studying electrical spin injection and detection in both metallic and SC materials, because spurious magnetoresistance effects, such as the magneto-Coulomb effect [113], local Hall effects [57], and anisotropic magnetoresistance effects [114], are eliminated or greatly diminished. Nonlocal spin injection and detection experiments have been conducted in many systems, including metallic and SC channels [115, 116, 11, 117, 68]. However, the nonlocal technique may not be sufficient for operational spintronics devices due to the small signals they provide. A prerequisite for various concepts of spin transistors is the electrical spin signal in local configuration, as a result 2T local spin valve measurements are equally important. It is worth noting that for the same pair of injector and detector, similar switching fields are observed for both local 2T and nonlocal 4T measurement schemes (see

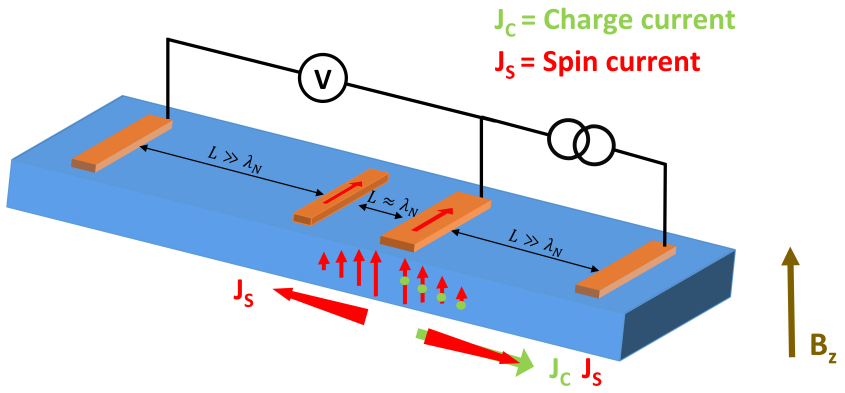

Figure 4.13: (a) Schematic for 3T Hanle effect measurement. An external magnetic field B_z is applied perpendicular to the magnetization.

Figure 4.12), which is a strong indicator that the local 2T signals indeed originate from the spin accumulation in the Si NW channel and not from other magnetoresistance effects.

Hanle Effect Measurements.

Hanle effect provides another rigorous way of measuring spin signals and verifying spin accumulation at the FM/SC interface. In Hanle measurements, an external magnetic field is applied perpendicular to the magnetization direction of the injector, as shown in Figure 4.13. These type of measurements probe the average spin orientation after transit time t through the channel. The spin of the electrons precesses due to the presence of the external magnetic field with a frequency $\omega = g\mu_B B/\hbar$ (Larmor frequency), where μ_B is the Bohr magnetron. The transit time is determined by drift motion, hence $t = x/\mu E$, where μ is the electron mobility. This type of motion is periodic in time, and proportional to $\sin(g\mu_B Bt/\hbar)$. At a specific point in the channel, x, different electrons arrive with different transit times. Due to the uncertainty in transit time Δt, which can be caused by random diffusion processes, the spin precession angle can accordingly change by $\Delta\theta = \omega\Delta t$. This change is proportional to the magnetic field B and upon averaging over all different transit times, the average spin at a specific point will vanish. The suppression of the spin signal by this effect is called Hanle effect or spin dephasing [118]. The mathematical formula describing the spin dephasing is:

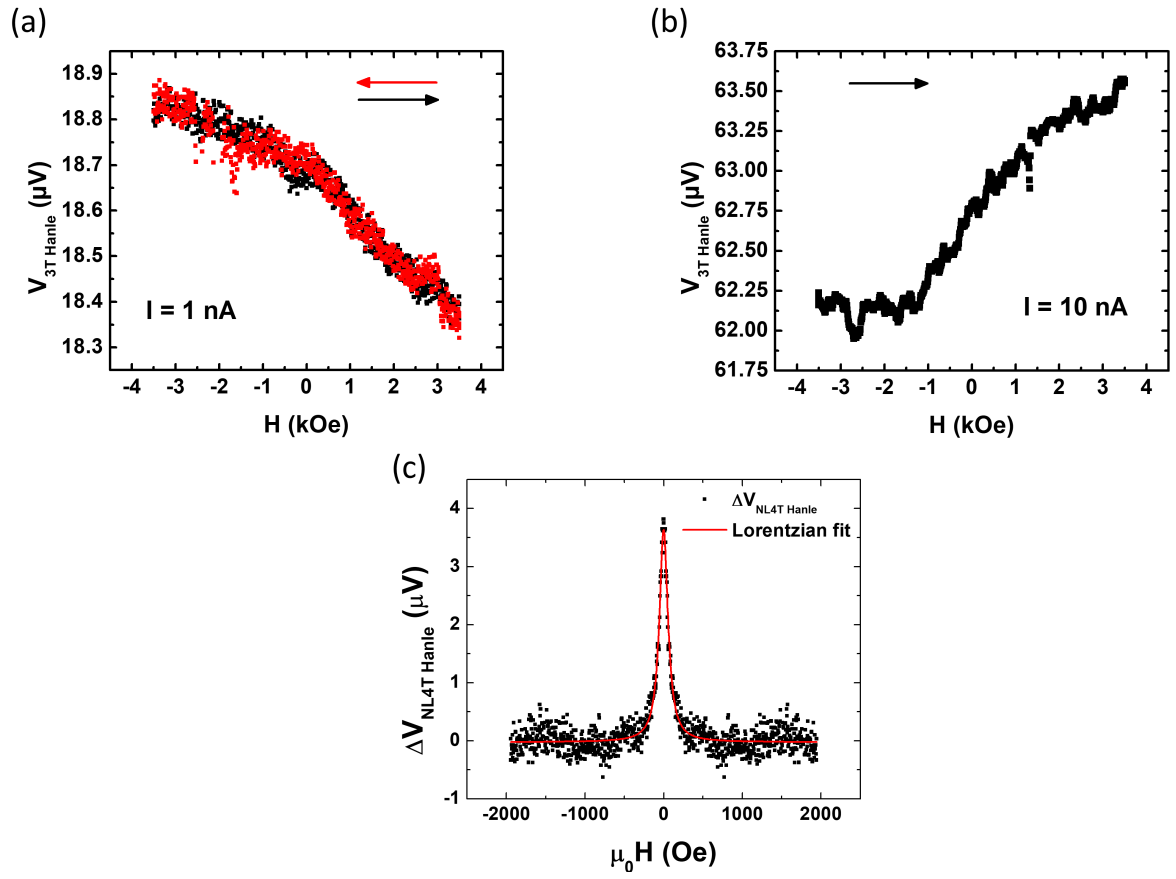

Figure 4.14: (a), (b) AC 3T Hanle effect measurements from two consecutive electrodes on a single Si NW. The external magnetic field is applied perpendicular to the in-plane direction. The arrows represent the direction of external magnetic field sweeps. (c) Nonlocal Hanle effect measurement from an Fe/AlGaAs heterostructure obtained by Joon-Ill Kim, a former student in our group ([119]).

$$S_x(x,t) \sim \frac{1}{\sqrt{4\pi Dt}} e^{-(x-v_d t)^2/4Dt} e^{-t/\tau} \sin(\omega t) \tag{4.27}$$

where τ is the spin dephasing time, D is the spin diffusivity, and $v_d = \mu E$ is the drift velocity. To obtain the measured spin at a specific point x, the equation has to be integrated over all transit times t from zero to infinity.

In Hanle effect measurements, a Lorentzian distribution of the measured voltage around zero applied magnetic field is predicted [11]. From the full width at half maximum (FWHM), the spin lifetime, and spin diffusion length ($\lambda_N = \sqrt{D\tau}$) can be extracted [11, 120]. Figures 4.14 (a), (b) show attempts of 3T Hanle effect measurements on a Si NW with two consecutive electrodes, and

Figure 4.14 (c) shows an example of a Hanle effect measurement with a Lorentzian fit from an Fe/AlGaAs heterostructure [119]. In the Si NW devices, there is no discernible Hanle (Lorentzian) curve around $H = 0\ Oe$, which means that we could not observe the precession of the spins as the perpendicularly applied magnetic field is swept between $\pm 3000\ Oe$. This is likely due to the dome-shaped morphology of the FM electrodes on top of the cylindrical NWs. The contacts are not planar, and the easy axis of magnetization is not parallel to the in-plane direction on top of the NW. As a result, the magnetization of the FM electrode is not always perpendicular to the applied magnetic field, perhaps with the exception of a small surface area at the top of the NW. Not having a uniquely defined magnetization direction hinders the Hanle measurement. It has been shown that planarization processes in NW devices can help facilitating Hanle measurements in NW devices [19]. In these processes, the NWs are embedded inside a thin layer of resist, which is etched away to expose only a few nanometers of the top surface of the NWs. Consequently, the deposited electrodes have a rectangular profile and amenable to Hanle measurements.

4.2.2 Takahashi-Maekawa Model

The data in my studies are analyzed within a general model of spin diffusion in a normal channel under electrical spin injection from a FM, and specifically the "Takahashi-Maekawa" model [121, 122].

The electron spin transport depends on a number of factors including the interface resistance, the FM electrode resistance, the electrode spin polarization, the channel resistance, and the spin diffusion length in the material. These factors determine the conditions for efficient spin injection, spin accumulation and spin transport (current) in the channel. Generally, the spin-dependent transport equations for the electrochemical potentials of spin-up and spin-down electrons can be applied to systems with junction resistance ranging from a metallic contact to a tunneling regime. The injection/detection of spin accumulation depends strongly on the nature of the FM/SC junction interface. The most efficient spin injection and detection are achieved with thin tunnel barriers [24].

In addition, the dimensions of the contact area can affect the spin signal in real devices. For example, the contact size could affect the uniformity of the interface current density [123]. The homogeneity of the current distribution affects the effective contact area through which most of the current passes, and as a result the spin current. For SC channels where the interface resistance

is much larger than the FM electrode resistance, the current distribution is considered uniform. Figure 4.15 shows top-view and side-view schematics of a spin device and the dimension parameters used in the following equations.

The spin accumulation signal (ΔR_S) depends on the relative magnitude between the junction resistances ($R_{i,inj}, R_{j,det}$) and the spin resistances (R_N and R_F), and is given by the following equation:

$$\Delta R_S = \frac{V_{\uparrow\uparrow} - V_{\uparrow\downarrow}}{I} = R_N \frac{(2P_{1,inj}r_1 + 2p_F r_F)(2P_{2,det}r_2 + 2p_F r_F)e^{-L/\lambda_N}}{(1 + 2r_1 + 2r_F)(1 + 2r_2 + 2r_F) - e^{-2L/\lambda_N}} \tag{4.28}$$

with the normalized resistances

$$r_i = \frac{1}{(1 - P_i^2)} \frac{R_i}{R_N},\ r_F = \frac{1}{(1 - p_F^2)} \frac{R_F}{R_N}, \tag{4.29}$$

where $R_{i,inj/det}$ is the interface resitance of junction i, R_N and R_F are the spin resistances of the nonmagnetic N and ferromagnetic F electrodes with the lengths of λ_N and λ_F respectively

$$R_N = \frac{\rho_N \lambda_N}{A_N},\ R_F = \frac{\rho_F \lambda_F}{A_J}, \tag{4.30}$$

where ρ_N, ρ_F are the resistivities of N and F, and $A_N = w_N d_N$, and $A_J = w_N w_F$ are the contact areas of the junctions, as shown in Figure 4.15. P_i is the interfacial current spin polarization, and p_F the spin polarization of the FM electrodes F_1 and F_2.

The expression for the spin accumulation (Equation 4.28) can be simplified depending on the nature of the junctions. There are three limiting regimes that can be defined depending on the relation between the junction resistances, channel spin resistance, and FM spin resistance. First, the transparent regime is defined with $R_i \ll R_F \ll R_N$. Second, the tunneling regime is defined when $R_i \gg R_N \gg R_F$. Third, the intermediate regime is defined when $R_F \ll R_i < R_N$. The extracted values for the junction resistances and channel resistances for the Si NWs used in this study (see Table 4.5 and Table 4.6), determine that the intermediate regime is appropriate for the description of the experimental data. For the intermediate regime, the expression for the spin accumulation signal (ΔR_S) is simplified to the following expression:

$$\Delta R_S = \frac{V_{\uparrow\uparrow} - V_{\uparrow\downarrow}}{I} = \frac{4P_J^2}{(1 - P_J^2)^2} \left(\frac{R_{1,inj} R_{2,det}}{R_N} \right) \frac{e^{-L/\lambda_N}}{1 - e^{-2L/\lambda_N}}, \tag{4.31}$$

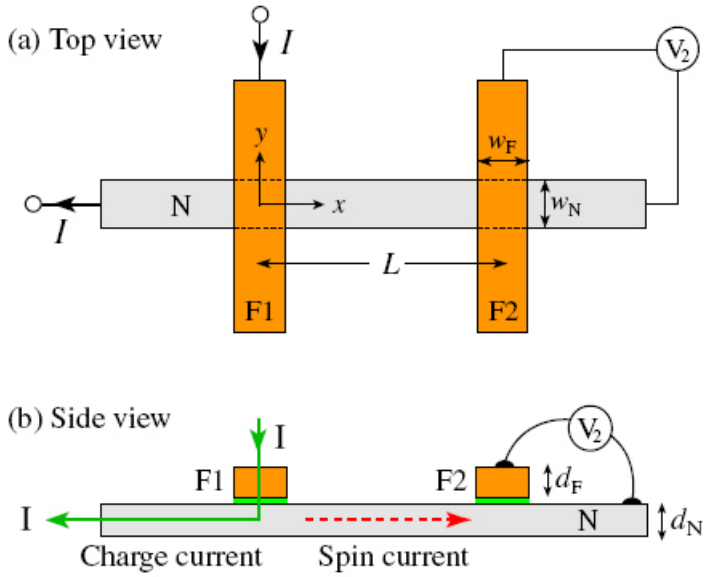

Figure 4.15: Nonlocal spin injection and detection device. (a), (b) Schematic diagrams illustrating geometrical parameters for top-view and side-view of the device. Figure is adapted from reference[122].

where R_i is the interface resistance of junction i, $R_N = \rho_N \lambda_N / A_N$ is the spin resistance of the semiconductor channel, L and λ_N are the channel length and spin diffusion length respectively. P_J is the interfacial current spin polarization of the injector and detector. This equation is going to be used to extract information about how the current spin polarization changes for different Schottky junctions along the length of the Si NWs.

However, two crucial aspects are not included in the theoretical model: The bias dependence of the spin injection/detection polarizations, and different interfacial properties that could alter the spin polarization such as the depletion width of SBs [124, 125]. The former was found by Dash *et al* in Si heterostructures, $Ni_{80}Fe_{20}/Al_2O_3/n-type\ Si$. They observed that there is an asymmetry in the measured spin signals with respect to voltage/current polarity [67]. Specifically, they observed that for electron injection ($I > 0$) the spin signal is increasing linearly with current density, whereas a sub-linear behavior was observed for electron extraction ($I < 0$). In addition, they observed that the bias asymmetry is not universal, which means that it depends on the junction properties, such as the material of the electrodes. In similar systems, with different tunnel barriers, $CoFe/MgO/n-type\ Si$, Jeon *et al* observed a different variation of the spin signal with

bias voltage; they observed a symmetric and linear bias dependence [126]. The conclusion that can be drawn from these experiments is that the electronic structure of the FM/(insulator interface) affects the bias dependence of the spin signal.

The bias dependence of the injected spin current is due to the dependence of the tunnel spin polarization on the energy of the electrons [127, 128]. For positive bias, occupied states below the Fermi energy of the FM contribute to the tunnel current, whereas at negative bias unoccupied states above the Fermi energy of the FM contribute to the tunnel current (electrons tunnel from Si into the FM). Tunnel spin polarization is different at different Fermi energy levels. It has also been studied that the efficiency of the spin detection depends on the bias voltage [110, 129].

In my studies, I will focus on the dependence of the spin polarization on the different interfacial properties (different SBs), since all the measurements were performed in the low bias regime; bias dependence effects are negligible.

4.2.3 4T Spin Valve Measurements

This section is dedicated to the nonlocal spin valve signals obtained on a couple Si NW devices. As it was described earlier, in the NL-4T configuration the spin accumulation is measured outside the charge current path (open-circuit voltage), while an in-plane magnetic field parallel to the (long) easy axis of the FM electrodes is swept between $-4\ kOe$ and $+4\ kOe$. Consecutive electrodes in the devices have different widths, alternating from $\sim 0.8\ \mu m$ to $\sim 1.2\ \mu m$, so that we can independently switch the magnetization direction of the FM electrodes.

The data are plotted after the background is subtracted from the raw data. In order to subtract the background, I mask the voltage increase/decrease and fit the remaining signal with a fourth degree polynomial, which is then subtracted from the raw data. An example of a spin valve signal before subtracting the background, after the fitting procedure, and after the background subtraction, is shown in Figure 4.16. The background may contain information about local MR effects which are not relevant to spin accumulation. Control experiments are the only way to separate these signals [125]. However, coupling with such signals at low temperatures, and in NWs with diameters much smaller than the spin diffusion length is unlikely to drastically affect the spin accumulation signals.

We focus on electrodes that are located close to the base of the NWs. More specifically, the electrodes that are used for the spin transport measurements are located up to the middle of the

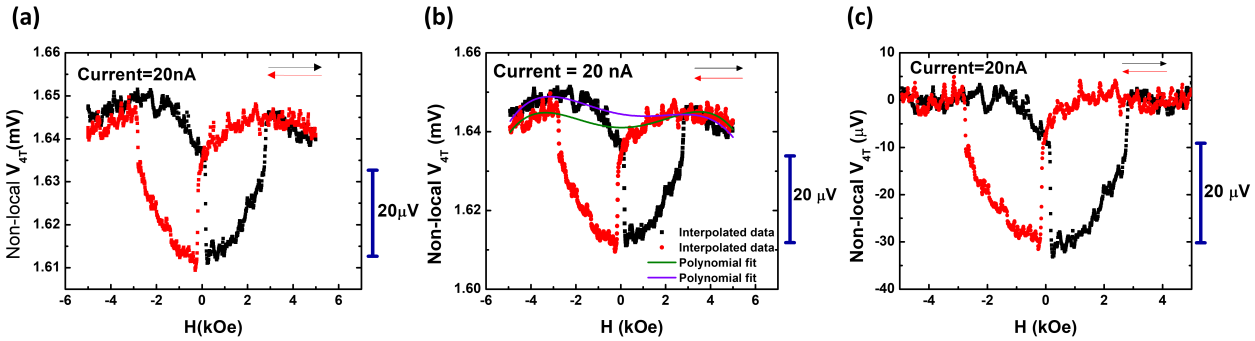

Figure 4.16: (a) Raw data of a nonlocal spin valve signal. (b) Interpolated data and polynomial fits to the raw data. The green line corresponds to the red data points, and the purple line corresponds to the black data points. (c) Background subtracted nonlocal spin valve signal.

NWs, $12 - 15\ \mu m$ away from the base, because at low temperatures ($5\ K$) after that point the junction resistances become too large, and hence negatively affect the spin signals. In addition, the SB widths become wider and the tunneling current is also reduced. Generally, there is a window of junction resistances where spin injection/detection is efficient [64, 130]. Below or above that range, spin signals are difficult to detect. In our Si NW devices, this effect can be directly observed due to the axial doping profile, which enables the formation of SBs with different widths and heights along the length of the Si NWs. To the best of our knowledge, this is the first observation of this ramification on a single device.

The existence of the optimal resistance window has been observed previously in systems using oxide tunnel barriers (MgO). However, many replicas with different oxide barrier widths had to be fabricated and measured individually, which render the analysis of the signals more complex [17]. For example, different growth parameters of the oxide tunnel barriers can control the location and density of localized states, which could affect the spin signals as it has been recently debated [102]. Furthermore, it is difficult to precisely control the thickness of an oxide layer in the order of a few nanometers.

Another limiting factor for determining spin signals is that large resistances often produce large background signals (of millivolts), and as a consequence the detection of small spin signals (of microvolts) can be challenging. In other words, the signal to noise ratio becomes smaller with the

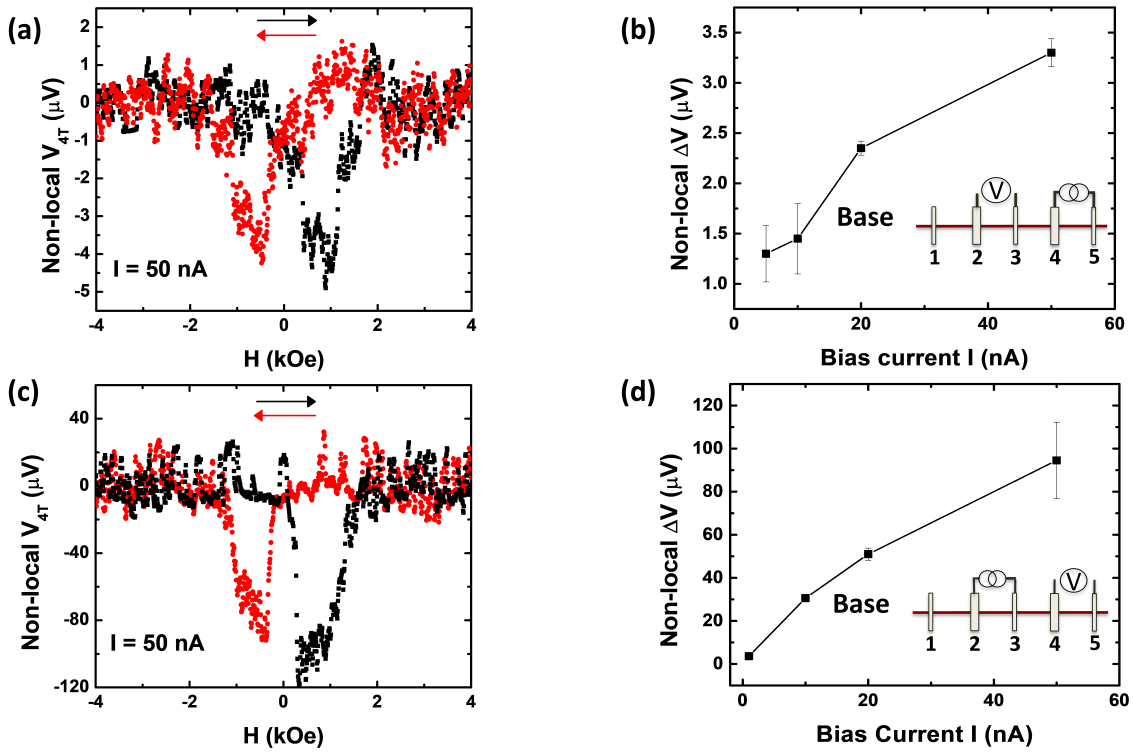

Figure 4.17: Nonlocal 4T spin valve field sweeps at $T = 5\ K$ and bias current $I = 50\ nA$, and bias dependence of the spin signal amplitude, for the same Si NW section (between #3-4) but different spin injector-detector combinations: (a), (b) #4 as injector and #3 as detector; (c), (d) #3 as injector and #4 as detector. The error bars represent the standard deviation from the values extracted from two consecutive sweeps of the applied magnetic field. The red and black arrows represent the sweeping direction of the applied magnetic field.

increase of junction resistance. Proper device design utilizing asymmetric junctions, such as in these Si NWs, can prove beneficial for spin transport.

Our devices with an inhomogeneously doped Si NW channel and FM/NW contacts of varying resistances present a unique platform to investigate how the NL-4T signals depend on the injector, detector, and channel properties. Specifically, on a single Si NW device, we can examine the variation of the NL-4T spin signal upon i) interchanging the injector and detector between two adjacent FM/NW contacts of different properties, and ii) using a same FM/NW contact as the detector and the contact on either side as the injector.

Figure 4.17 shows a direct comparison of two NL-4T signals taken at 5 K from the same set of four FM/NW contacts on a Si NW, with the only difference being an interchange of the injector and

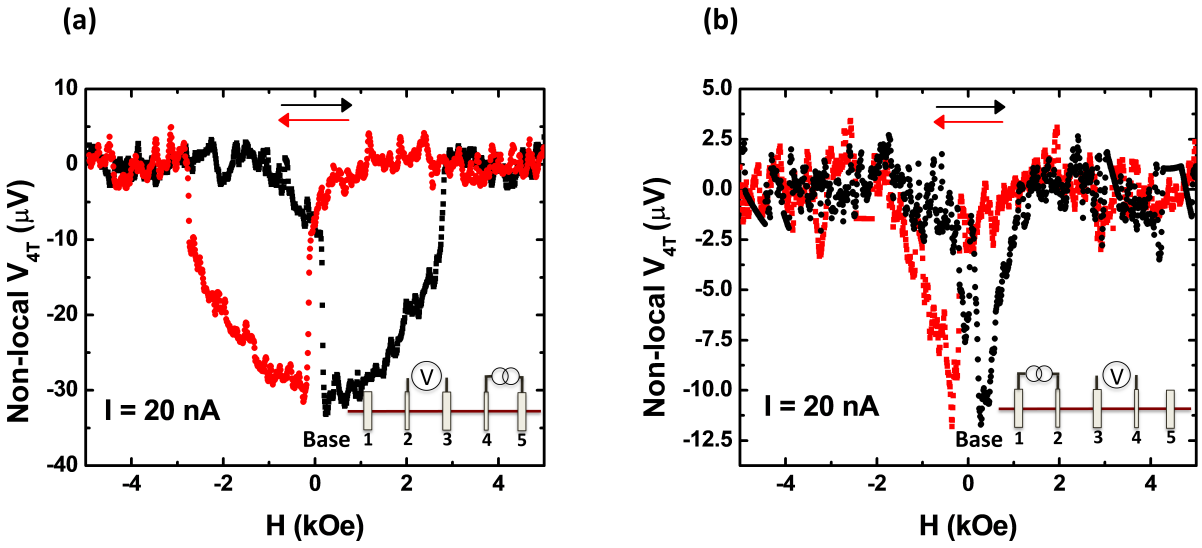

Figure 4.18: (a), (b) Nonlocal 4T spin valve signals from a Si NW device at $T = 5\ K$ and bias current $I = 20\ nA$. The injector was #2 and #4 respectively, while the detector was the same #3, as shown in the insets. The red and black arrows represent the sweeping direction of the applied magnetic field.

detector between the two inner contacts, #3 and #4, across the same NW channel. The contact resistances are $R_3 = 8.0\ k\Omega$ and $R_4 = 41.0\ k\Omega$. Figure 4.17 (a) shows the NL-4T signal for the setup with #4 and #3 as injector and detector respectively, at a bias current $I = 50\ nA$, while Figure 4.17 (c) shows the result after an interchange of the roles of the two electrodes. The two signals show broad similarities in their field dependences, with approximately the same shape and switching fields for the spin valve voltages in the antiparallel states. This is consistent with the expectation that the field-dependence of the NL-4T voltage is determined by the relative magnetic orientations of the injector and detector. However, the magnitudes of the two signals differ by a factor of 26, at about 3.5 μV (91.5 μV) when the high (low) resistance contact #4 (#3) is used as the injector. It is worth pointing out that the spin transport channels are the same section of the Si NW in both cases. Figures 4.17 (b), (d) show the corresponding bias current dependences for the two configurations. There is approximately a linear increase of the spin accumulation signal with the increase of the bias current. The magnetic field dependent switching of the non-local voltage is not as sharp as that in planar devices due to the dome-shaped profile of the FM electrodes on top of the cylindrical NW. In addition, the cylindrical shape is possibly the reason why we can observe

Table 4.5: Sample parameters for devices corresponding to Figures 4.17 and 4.18. L_{ch} is the channel length, R_{ch} is the channel resistance, and ρ is the channel resistivity.

Sample	$L_{ch}(\mu m)$	$R_{ch}(k\Omega)$	Si NW resistivity ρ $(\Omega \cdot cm)$
Figure 4.17	0.87	$R_{4-3} = 450$	$\rho_{4-3} = 0.122$
Figure 4.18	1.77	$R_{3-2} = 276$	$\rho_{3-2} = 0.056$
	1.57	$R_{4-3} = 665$	$\rho_{4-3} = 0.175$

broad switching points from antiparallel to parallel configurations for different FM electrodes on the same Si NW, or for different Si NW devices with similar designs (compare Figures 4.17 and 4.18).

Figure 4.18 shows data from a different device. For this set of measurements from a single Si NW, the same electrode is used for spin detection, while a different electrode on either side is used for spin injection. Both measurements were performed with injection current $I = 20\ nA$, and the injector-detector distances are approximately the same (see Table 4.5). However, the channel resistivities for the two neighboring sections of the Si NW are different. Specifically, they are $\rho_{3-2} = 0.056\ \Omega \cdot cm$ and $\rho_{4-3} = 0.175\ \Omega \cdot cm$ (see Table 4.5). Figure 4.18 (a) shows the NL-4T spin signal for the injector located on the more insulating side of the NW (high junction resistance, #4), with a signal amplitude of $\Delta V_{4T} = 20\ \mu V$. Figure 4.18 (b) shows the NL-4T spin signal for the injector located on the more conducting side of the NW (low junction resistance, #2), with a signal amplitude of $\Delta V_{4T} = 9.2\ \mu V$. Table 4.5 lists the sample parameters for the devices corresponding to Figures 4.17 and 4.18. Specifically, the channel resistance for the device in Figure 4.17 is $R_N = 450\ k\Omega$ (contacts #4-3), and for the device in Figure 4.18, $R_N = 276\ k\Omega$ (contacts #3-2) and $R_N = 665\ k\Omega$ (contacts #4-3). The corresponding channel lengths and resistivities are $L_{4-3} = 0.87\ \mu m$, $\rho_{4-3} = 0.122\ \Omega \cdot cm$ (Figure 4.17), and $L_{3-2} = 1.77\ \mu m$, $\rho_{3-2} = 0.056\ \Omega \cdot cm$, $L_{4-3} = 1.57\ \mu m$, $\rho_{4-3} = 0.175\ \Omega \cdot cm$ (Figure 4.18). The spin polarization of the FM (CoFe) is taken as $P_J = 0.35$, which is a reasonable value for CoFe alloys [131].

The Si NW channel resistances were determined directy from 4T IV measurements, and the FM/NW junction resistances were extracted with the method described in the electrical characterization part. The formation of the doping profile was described in Chapter 3. However, at this point I would like to describe the physical picture which describes the experimental results. Rigorous examination of the doping profile in such Si and germanium (Ge) NWs by electrical and pulsed

laser atom probe tomography techniques, revealed a core-shell structure [95, 132, 96]. Specifically, the NWs have a core of uniform diameter and doping density, and a thin shell of large gradients of thickness ($10\ nm - 1\ nm$) and doping density. From electrical measurements performed after etching the shell structure of the NWs, it is evident that these NWs can be regarded as having constant mobility and diffusivity. The variation in carrier density and electrical conductivity in the axial direction is related to the shell structure.

In order to explain my experimental spin transport results, I consider the thin shell as a modulation doping layer, hence scattering of the electrons from the phosphorus dopants in the shell (spin relaxation due to hyperfine interaction with nuclei, at low temperatures) is homogenized once the spins are injected inside the channel. Therefore, the spin diffusion length is considered to be constant ($\lambda_N = 2.2\ \mu m$) in the Si NWs.

The value of the spin diffusion length has been estimated by applying the theoretical model (Equation 4.31) with fixed spin polarization ($P_J = 0.35$) from different configurations. Specifically, the values are 0.54 μm, 0.84 μm, 0.61 μm and 6.80 μm. In addition, spin transport experiments performed on nondegenerate Si with dopant concentration of about $2\times10^{18}\ cm^{-3}$ at 300 K, estimate $\lambda_N = 1.4\ \mu m$ [28]. These values are in reasonable agreement. In this study, we focus on the effects of the interfacial properties on current spin polarization, and the specific value of the spin diffusion length does not affect the qualitative picture of that dependence.

The channel lengths for the Si NW devices are comparable to the spin diffusion length (for all the spin valve configurations) as a result, for R_N, I use the experimentally determined 4T resistance values, which are listed in Table 4.5.

Implicit in Equation 4.31 is a symmetry between the injector and detector, meaning that for an interchange of the injector and detector the spin signal should be the same. However, this is in apparent contradiction with the experimental results obtained on the device in Figure 4.17. As Figure 4.17 suggests, interchanging the injector and detector yields a spin accumulation signal (ΔR_S) 26 times higher for the same injection current when the lower-resistance contact (#3) is used as the injector (Figures 4.17 (a), (c)). The bias dependence effect on the spin injection efficiency is not the reason for this asymmetry. To verify this statement, the bias current dependence of the spin valve signals was measured (Figures 4.17 (b), (d)). The results show a small nonlinearity which cannot explain the observed asymmetry. Similar asymmetry was observed even in the case

when the two injector junctions were biased at the same voltage bias of $V = 12\ mV$, with the spin signals differing by a factor of 15.6. The results are summarized in Table 4.6.

Since the spin detector is unbiased in the NL configuration, these observations suggest that there is a significant difference in the spin polarization of the injected current, which depends on the nature of the FM/SC interface of the injector. Specifically, we observe that when the low resistance contact #3 is used as the injector, the spin accumulation signal is significantly higher, implying that a higher CoFe/Si NW contact resistance in our devices leads to a lower spin injection polarization.

In addition, Figure 4.19 shows multiple NL spin valve signals from another device at different current bias. We can appreciate the similarity of the signals and how the amplitude changes for different bias conditions. The fact that these signals are positive can be explained by invoking that the spin polarizations of the injector and detector have opposite polarities. We note that according to Equation 4.31, the sign of the spin signal depends on the signs of the spin polarizations $P_{inj},\ P_{det}$. Their product defines the overall sign of the detected spin signal. The inversion of the spin signals has also been observed in Fe/GaAs heterostructures via measurement of voltage bias experiments for the detector electrode [110].

A similar analysis is applied to the data acquired with the device in Figure 4.18. In this case, the same junction (#3) is used as the spin detector, while junctions #2 and #4 as the spin injectors. Since the two injectors have different interface resistances and the two sections of the NW have different resistivities, the spin accumulation signals are expected to be different according to Equation 4.31. Substituting the respective values for the interface resistance, channel resistance, and spin diffusion length $\lambda_N = 2.2\ \mu m$ into Equation 4.31, if one assumes that the interfacial spin polarization $P_J = 0.35$ is the same for the injector and the detector, a ratio of 10.9 is expected for the spin accumulation signals, ΔR_S:

$$ratio = \frac{\Delta R_S\,(high\ resistance\ injector)}{\Delta R_S\,(low\ resistance\ injector)} = 10.9 \tag{4.32}$$

However, the experiments yield a ratio of 4.3 (Table 4.6), which is significantly lower than the theoretical expectation. Consequently, this is another strong indication that the higher resistance contact produces a lower spin injection polarization.

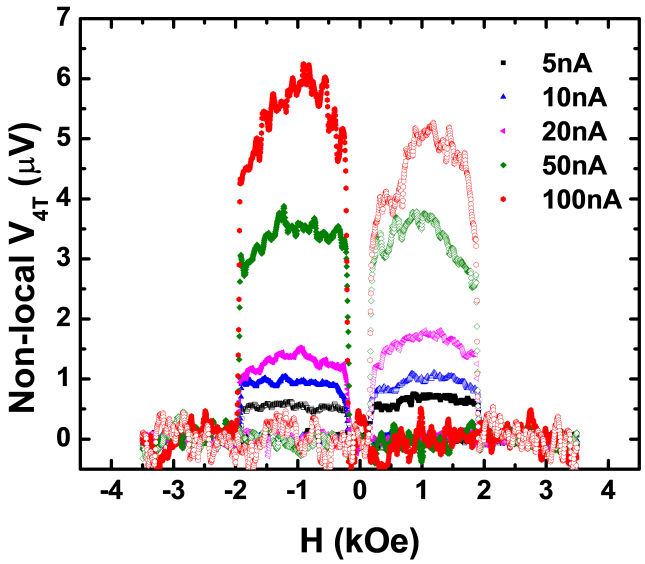

Figure 4.19: AC Nonlocal 4T spin valve bias current dependence. The colors represent different bias currents, and the open/closed symbols indicate the sweeping direction of the applied magnetic field. The change of the spin signal amplitude for different bias conditions is shown.

The aforementioned observations point to a direct correlation between the spin injection polarization and the varying doping density along the length of the Si NWs. To quantify the experimental results, I introduce a phenomenological parameter (α) in Equation 4.31:

$$\Delta R_S = \frac{V_{\uparrow\uparrow} - V_{\uparrow\downarrow}}{I} = \frac{4\alpha P_J^2}{(1-\alpha P_J^2)^2}\left(\frac{R_{1,inj}R_{2,det}}{R_N}\right)\frac{e^{-L/\lambda_N}}{1-e^{-2L/\lambda_N}} \tag{4.33}$$

The parameter α represents the dependence of the spin signals on the different interfacial properties due to the varying doping density at the FM/NW junctions. The extracted values for the parameter α from the measurements are listed in Table 4.6. In addition, Table 4.6 lists the junction resistances (R_i) and the spin accumulation signals (ΔR_S). The parameter α is observed to decrease monotonically with increasing junction resistance R_i of the injector contact.

The variation of parameter α is interpreted as a decrease of the injected current spin polarization across the FM/NW SB of increasing width/height. From previous electrical characterization measurements with nonmagnetic silver (Ag) electrodes, we have observed a decrease of the SB height with increasing doping density [108]. As it has been shown theoretically and experimentally, both the magnitude and the sign of the spin polarization P_J can depend on the SB height [133, 134].

Table 4.6: 4T nonlocal spin valve results. The spin valve configuration indicates which electrode is used as a spin injector. The bias voltages for the spin injectors are also provided. R_i is the interface (junction) resistance; α is a phenomenological parameter describing how the injector polarization changes for different interfaces. $\Delta R_S = \Delta V/I$ is the nonlocal spin accumulation signal.

Sample	Spin valve configuration	$R_i(k\Omega)$	α coefficient	$\Delta R_S(\Omega)$
Figure 3	I 4-5 ; V 3-2 $V_{4,inj} = 12\ mV$	$(i = 3)$ 8	(#4) 0.25	117
	I 3-2 ; V 4-5 $V_{3,inj} = 12\ mV$	$(i = 4)$ 41	(#3) 2.21	1830
Figure 4		$(i = 2)$ 25.0		
	I 4-5 ; V 3-2 $V_{4,inj} = 8\ mV$	$(i = 3)$ 65	(#4) 0.12	2000
	I 2-1 ; V 3-4 $V_{2,inj} = 8\ mV$	$(i = 4)$ 570	(#2) 0.27	460

The experimental results can be accounted for within a picture of variation of the spin polarization of tunneling electrons through a tunneling barrier. Specifically, I am going to describe how the FM's $3d$ electron states and $4sp$ electron states contribute to the tunneling current for varying Schottky junctions, and how the spin polarization and the spin accumulation are affected. This discussion is based on relevant previous experiments in AlGaAs.

The nature of the tunneling current and how it impacts the spin polarization have been a subject of intensive discussion since early spin-polarized tunneling experiments, which determine the spin polarization of FMs [41, 135, 136, 137]. Specifically, the sign of the spin polarization and how it is determined has been debated. One model that describes the experimental findings is the following: $3d$ electrons provide most of the magnetization of transition metals but are localized, while itinerant $4sp$ electrons, dominating the transport, are polarized by exchange interaction with the localized $3d$ electrons, and as a result they have a smaller polarization with opposite sign [138, 137]. This realization lead to the description that the total tunneling current emitted from a FM metal originates from both $3d$ electorn states and $4sp$ electron states, and the composition of the tunneling current determines the spin polarization.

More specifically, as it was shown by scanning tunneling microscopy (STM) [139] and spin-resolved superconducting tunneling [140], as well as theoretical modeling [138, 137], both the highly

polarized, localized $3d$ electrons and the less polarized, higly mobile $4sp$ electrons contribute to the current from a transition metal FM across a tunnel barrier. The overall spin polarization of the current depends on the relative contributions of the two currents. These localized and delocalized currents have much different characteristic decay lengths k_{sp}^{-1} and k_d^{-1}, therefore their relative contributions to the current spin polarization can change greatly depending on the barrier thickness. A schematic representation of the tunneling scheme with two currents having different decay lengths is shown in Figure 4.20 (a). Specifically, the total tunneling current can be expressed as the superposition of the $3d$ and $4sp$ tunneling currents:

$$i_T = i_{d,0}\, e^{-k_d W} + i_{sp,0}\, e^{-k_{sp} W} \tag{4.34}$$

where $i_{d,0}, i_{sp,0}$ are the contributions to the tunneling current at the interface by the $3d$ and $4sp$ electrons, respsectively, and W is the barrier width. The overall spin polarization of the current is given by $i_T P = i_d P_d + i_{sp} P_{sp}$. It should be pointed out that in transition metal ferromagnets such as CoFe, P_d is large and negative, whereas P_{sp} is small and positive. In systems with oxide barriers such as Al_2O_3, the interfacial bonding favors the $4sp$ states and the current spin polarization across the barrier is positive and increases with the barrier thickness due to the rapidly diminishing contribution from the negatively polarized $3d$ states [140]. In contrast, it was shown by STM experiments on AlGaAs [139] that the tunneling current across a vacuum barrier is predominantly from the $3d$ states, hence the current spin polarization decreases with increasing barrier width.

In my experiments, I attribute the observed monotonic decay of the parameter α to the increased contribution of the $4sp$ states at increasing injector junction resistance. As we move from the base (low resistance junctions) towards the tip (high resistance junctions) of the NWs, the electrodes acting as injectors have wider depletion widths, and as a result the total spin polarization of the current is expected to decrease due to the increased contribution from the $4sp$ states, which are oppositely polarized compared to the $3d$ states. This statement is supported by the theoretical expression for the spin polarization of the tunneling current:

$$P = \frac{P_d + P_{sp}\frac{i_{sp,0}}{i_{d,0}} e^{-(k_{sp}-k_d)W}}{1 + \frac{i_{sp,0}}{i_{d,0}} e^{-(k_{sp}-k_d)W}} \approx P_d + P_{sp}\frac{i_{sp,0}}{i_{d,0}} e^{-(k_{sp}-k_d)W}. \tag{4.35}$$

where P_d, P_{sp} are the spin polarizations for the $3d$ and $4sp$ electron states, respectively.

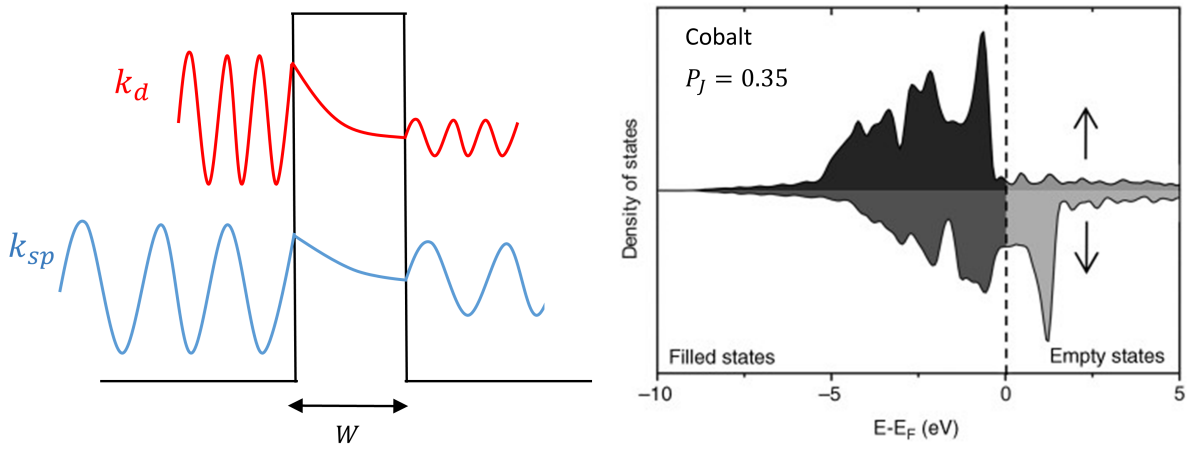

Figure 4.20: (a) Schematic representation for tunneling of two currents with different characteristic decay lengths, $k_d^{-1} < k_{sp}^{-1}$. (b) Density of states for cobalt (Co). At the Fermi level the density of states is larger for spin-down electrons [141].

The approximation in Equation 4.35 holds for $(i_{sp,0}/i_{d,0})\, e^{(k_d - k_{sp})W} \ll 1$, which is valid for these Si NW devices, since $i_{sp,0}/i_{d,0} \approx 10^{-2}$ is approximately the ratio of the $4sp$ to the $3d$ density of states at the Fermi level [139], and the exponential factor is on the order of $e^{(k_d - k_{sp})W} \approx 10$ for relatively thin barriers ($\sim 0.5\ nm$) [140]. Within this approximation, Equation 4.35 indicates that the second term becomes larger as the depletion width (W) becomes wider, since $k_d(\approx 2.86) > k_{sp}(\approx 3.33)$. Consequently, the overall current spin polarization decreases with increasing injector junction resistance, because P_d and P_{sp} have opposite signs.

At this point, I would like to evaluate the SB widths (W) in the CoFe/Si NW junctions and how they change along the Si NWs due to the doping gradient. As was mentioned in section 4.1.2, the depletion width in NWs and in the limit of $R\,(radius\,of\,NW) \gg W\,(depletion\,width)$ is given by $W = \sqrt{2\epsilon V_{bi}/eN_d}$, where V_{bi} is the built-in potential and N_d is the doping density. This expression, for $V_{bi} = 0.85\ V$ and $0.90\ V$, and based on the estimated change of the effective carrier density from $6.8 \times 10^{17}\ cm^{-3}$ to $4.5 \times 10^{18}\ cm^{-3}$, predicts a change in the depletion width from $40\ nm$ to $16\ nm$. The built-in potential was calculated using the work function of cobalt ($\Phi_{Co} = 5.0\ eV$) and equation:

$$V_{bi} = \frac{\Phi_B}{e} - \frac{E_c - E_{F,n}}{e} \tag{4.36}$$

where $\Phi_B = \Phi_{Co} - X_{Si}$, and $E_c - E_{F,n} = k_B T \cdot \ln(N_c/N_d)$ where $N_c = 2.8 \times 10^{19}\ cm^{-3}$ is the effective density of states at 300 K and N_d is the doping density, which I assumed to be equal to the two effective carrier densities. However, this estimate does not take into account the core-shell structure of our Si NWs. The core-shell structure can alter significantly the depletion layer width, as it was shown by Perea *et al.* Their experiments (pulsed laser atom probe tomography) suggest that the actual doping level within the shell of the NWs can be more than an order of magnitude higher than the values extrapolated from the effective carrier densities [95]. In addition, it has been suggested that this is possible because most of the dopants in the shell of such structures are electrically active [132]. Consequently, such variations in the doping density at the surface will have a significant impact on the depletion layer width (SB width), and a much thinner depletion width should be expected. In such a case, one can estimate that the depletion width can reach $W \sim 3.6\ nm$ for $V_{bi} = 0.98\ V$ and $N_d = 1 \times 10^{20}\ cm^{-3}$. This range of barrier widths are consistent with the dominance of the $3d$ states in the tunneling current, and an associated decrease of the overall current spin polarization with increasing W due to the increasing contribution of the $4sp$ states in the tunneling current. This physical picture offers a reasonable and self-consistent picture for the experimental observations.

4.2.4 2T Spin Valve Measurements

This section is focused on the local spin signals measured from the Si NW devices, and a direct comparison of the 2T local and 4T nonlocal signals. In the 2T local configuration, two consecutive electrodes of different widths are used to apply electric current and measure the voltage, while an external magnetic field is swept parallel to the (long) easy axis of magnetization of the FM electrodes between $-4\ kOe$ and $+4\ kOe$.

Figure 4.21 (a) shows the 2T spin valve signals for two consecutive pairs of CoFe contacts on the same Si NW at the same injection current of 10 nA. The higher-resistance pair produces a larger spin valve signal than the low-resistance pair. This is observed at all bias current, as it is evident in Figure 4.21 (b). Similar to the nonlocal 4T case, this is expected due to the different interface and channel resistances, as Equation 4.31 suggests. The ratio for the two signals is roughly $\Delta R_{3-2}/\Delta R_{2-1} \approx 3$. We can use Equation 4.31 to predict the ratio for the two signals corresponding to the two segments of the Si NW. Table 4.7 lists all relevant parameters for the two segments of the

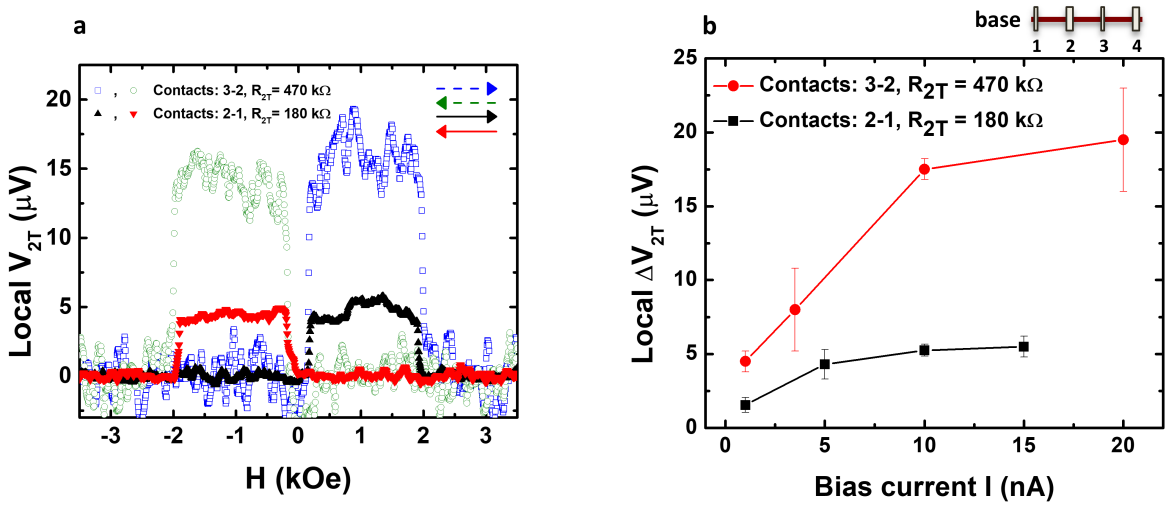

Figure 4.21: (a) Local 2T spin valve signals at bias current $I = 10\ nA$ for two consecutive electrodes, #2-1 and #3-2, on the same Si NW with $R_{2T} = 180\ k\Omega$ and $R_{2T} = 470\ k\Omega$ respectively. (b) Bias current dependence of the 2T spin valve signals for the two configurations. The error bars represent the standard deviation from the values extracted from two consecutive sweeps of the external magnetic field.

NW. According to the theoretical model, if we substitute the values from Table 4.7 into Equation 4.31, the expected ratio is $\Delta R_{3-2}/\Delta R_{2-1} \approx 2.7$, in good agreement with the experimental results.

A direct comparison of the local 2T signals with the nonlocal 4T signals provides additional insight into the spin transport. The devices in this study enable such a comparison over a broad range of contact resistances. First, we note that in all cases the 2T local and 4T nonlocal spin signals have broad similarities, confirming that the spin-valve signals indeed originate from the spin accumulation in the Si NW. Second, in lateral spin valve devices the ratio of the 2T spin signal over the nonlocal 4T spin signal amplitudes, $\Delta V_{2T}/\Delta V_{4T}$, is predicted to be 2 in a one-dimensional spin diffusion model [142, 130, 143].

Moreover, as it has been studied theoretically [142] and observed experimentally [143], in the linear regime of spin injection there is a symmetry of the nonlocal spin signal $V^{nl}_{\alpha,\beta}$ upon the interchange in α and β indices, which represent the injector and detector contacts. Due to this symmetry, $V^{nl}_{\alpha,\beta} = V^{nl}_{\beta,\alpha}$, and opposite direction of the current density $J_\alpha = -J_\beta$, one deduces that the spin accumulation in the local case is twice the spin accumulation signal in the nonlocal case,

Table 4.7: Interface and channel parameters for the device corresponding to Figure 4.21, and used to calculate the 2T spin valve signal ratios.

Sample	Spin valve configuration	$R_i(k\Omega)$	Si NW channel resistance ($k\Omega$)	$L_{ch}(\mu m)$	$\Delta R_S(\Omega)$
Figure 4.21	IV 2-1 $I = 10\ nA$	$(i = 1)$ 6	(2-1) 159	(2-1) 0.96	500
	IV 3-2 $I = 10\ nA$	$(i = 2)$ 15	(3-2) 407	(3-2) 1.10	1500
		$(i = 3)$ 49			

namely, $V_{2T}^{loc} = 2 \times V_{4T}^{nl}$.

In our case, this ratio can vary greatly due to the different interface resistances along the NW. The ratio can vary from values close to 2 to values significantly higher, depending on the positions of the injector/detector electrodes on the Si NW, and more sensitively, on the choice of the injector and detector in the nonlocal 4T measurement. As an example, I will focus on the data obtained from the device in Figure 4.22. For the same bias current, $I = 10\ nA$, the nonlocal spin signals across the same NW segment (between #3 and #4) from the combinations I3-2; V4-5 and I4-5; V3-2 are 25.8 μV and 1.4 μV, respectively. The local 2T spin signal between combination #4-3 is $\sim$ 57.0 μV, corresponding to ratios of $\Delta V_{2T}/\Delta V_{4T} = 2.2$ and 41.0. The variations arise from the different interfacial properties of the two adjacent FM/NW contacts due to the axial doping gradient. It is interesting to note that the ratio is close to the theoretical value of 2 for spin valves when the spin diffusion is initiated by the low resistance junction, while it is much higher in the case of the high resistance junction.

This discrepancy can be associated with the results from the spin diffusion model in the nonlocal 4T configuration. In the previous section, it was demonstrated that the spin injection polarization of the injector was higher for the low resistance junction. For a symmetric device (identical junction resistances), at low bias, the 2T signal is expected to be equal to the sum of the two signals measured in the nonlocal configuration for the same transport channel, $\Delta V_{2T} = \Delta V_{i,j}^{NL} + \Delta V_{j,i}^{NL}$, where i, j correspond to the different junctions, and $\Delta V_{i,j}^{NL}$ corresponds to the voltage drop at contact i due to the spin accumulation generated under contact j [144]. Figure 4.23 shows how the total spin accumulation $\mu^s(x) = \mu_S^s(x) + \mu_D^s(x)$ is generated at the source and drain contacts, and how

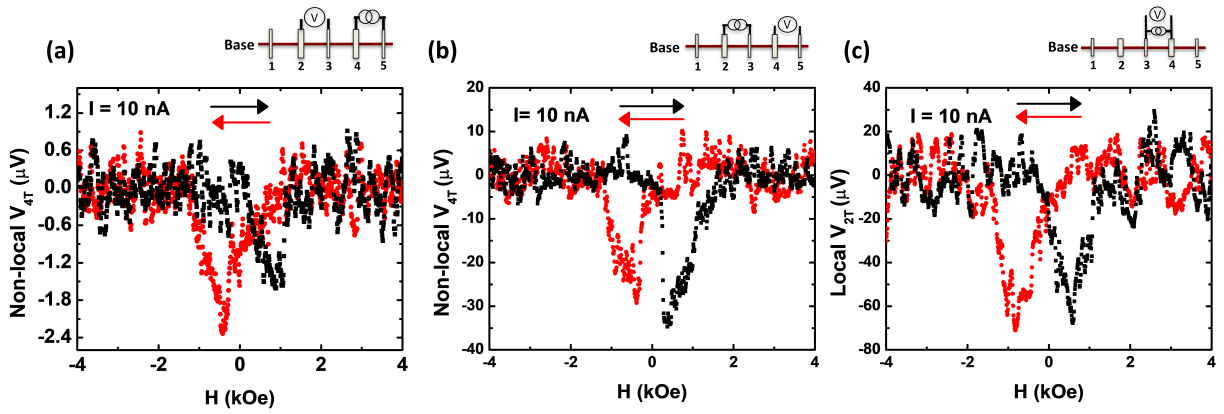

Figure 4.22: Local and nonlocal spin valve signals from a single Si NW for the same transport channel #4-3, and same bias current $I = 10\ nA$. (a) Nonlocal 4T spin valve signal for combination I:4-5; V3-2. (b) Nonlocal 4T spin valve signal for combination I3-2; V4-5. (c) Local spin valve signal for combination IV4-3. The amplitudes of the spin signals are 1.4 μV, 25.8 μV and 57 μV, respectively.

each contact (source/drain) contributes to the spin signal. Specifically, Figure 4.23 (a) shows the spin accumulation profile for the nonlocal and parallel configuration, and how it decays from the source electrode (injector) towards the drain electrode (detector); it also shows the amplitude of the spin signal $\Delta V^{nl} = 2\delta V$. Figure 4.23 (b) shows the spin accumulation profile for the local 2T and antiparallel configuration in an open geometry. The voltage drop at each FM/SC interface contains two spin-dependent contributions, one from the μ^s generated at one contact (e.g. drain) and one from the other contact (e.g. source). In the antiparallel configuration the two voltages add up, as it is shown in the schematic. Similarly, Figure 4.23 (c) shows the spin accumulation profile for the local 2T and parallel configuration. In this case, the two voltages partially cancel each other. In the limit of low electric field ($E \approx 0$), the 2T spin valve signal can be approximated by $\Delta V_{E=0} = \Delta V^{nl}_{S,D} + \Delta V^{nl}_{D,S}$.

In our case, this relation does not hold: $\Delta V^{NL}_{4,3} + \Delta V^{NL}_{3,4} = 25.8 + 1.4\ \mu V = 27.2\ \mu V$, while the measured 2T signal is 2.1 times as large. One possible explanation for this discrepancy is the effect of carrier drift on spin diffusion [109, 145, 144]. The existence of an electric field can affect spin transport along the channel, and effectively modify the spin diffusion length by enhancing or suppressing the diffusion process of the spins. This effect is more pronounced in materials with

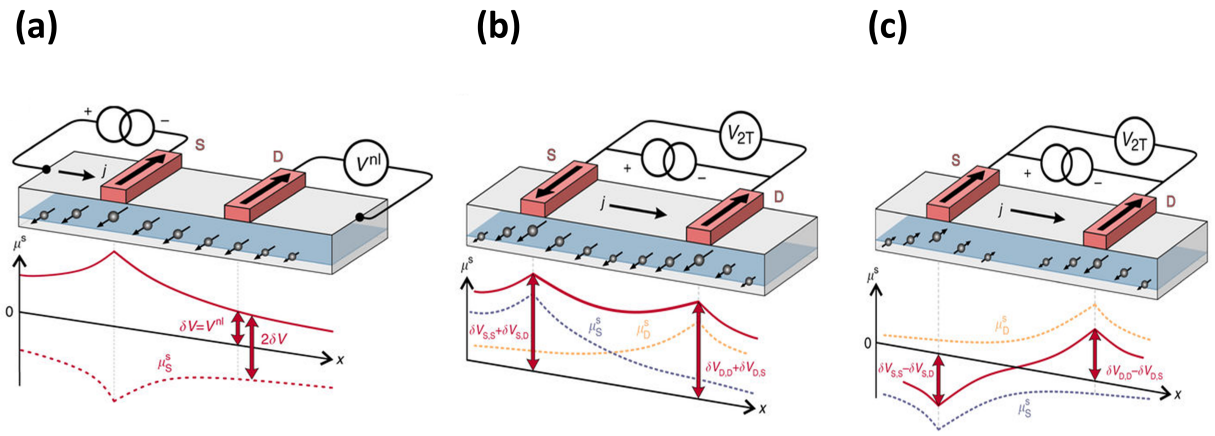

Figure 4.23: (a) Nonlocal 4T configuration, with S being an injector and D a detector. The solid line indicates the spin accumulation profile $\mu^s(x)$ for the parallel configuration, whereas the dashed line shows the spin accumulation profile for the antiparallel configuration. The total spin signal is $\Delta V_{nl} = 2\delta V$. (b), (c) Local 2T configuration for antiparallel (AP) and parallel (P) orientation of the magnetization of the source/drain electrodes, respectively. Solid lines indicate the total spin accumulation $\mu^s(x) = \mu^s_S(x) + \mu^s_D(x)$, where $\mu^s_{S(D)}$ (dashed line) is the spin accumulation generated at the source (drain). In AP (P) configuration, both components have the same (opposite) sign, and as a result μ^s is larger (smaller). Figure is adapted from reference [144].

low carrier densities. The spin drift effect redistributes the spin accumulation between the spin source and drain. The electric field enhances diffusion of spins in drift direction ("downstream") and suppresses diffusion of spins in the opposite direction ("upstream"). In the case of a forward bias current applied to the source FM/SC tunnel contact (electron extraction from the channel), the electric field in the channel causes drift of electrons from the source to the drain, thus enhancing the spin accumulation under the drain compared to the case of spin diffusion alone. Because the spin diffusion length of the extracted spins from source to drain is suppressed, spin accumulation in the channel adjacent to the source is almost insensitive to the magnetic configuration of the drain.

The equation that describes the modified spin diffusion length in the channel for the upstream (downstream) case is given by [145]:

$$\lambda_{N,u(d)} = \left[-(+)\frac{|E|}{2}\frac{\mu_e}{D_s} + \sqrt{\left(\frac{|E|}{2}\frac{\mu_e}{D_s}\right)^2 + \frac{1}{\lambda_N^2}} \right]^{-1} \tag{4.37}$$

where λ_N and $\lambda_{N,u(d)}$ are the intrinsic up (down) stream spin discussion lengths in the channel, respsectively, μ_e is the electron mobility, D_s is the spin diffusivity, and E the electric field.

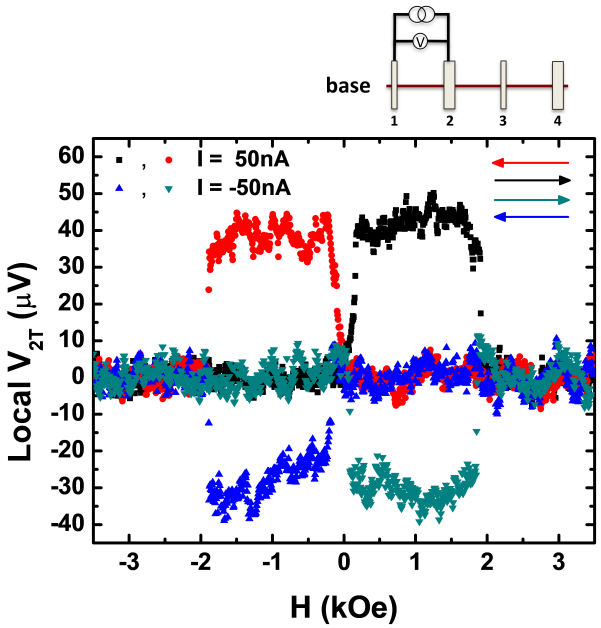

Figure 4.24: DC local 2T spin valve signals for bias currents, $I = +50\ nA$ and $I = -50\ nA$. The red and black points correspond the different sweeping directions of the applied magnetic field for $I = +50\ nA$, whereas the blue to cyan points represent the different sweeps for $I = -50\ nA$.

By comparing the ratio between the spin signal with electrical drift and without drift, it is possible to define an enhancement factor, which can be used to measure the effective spin diffusion length change. Specifically, one can define an enhancement factor as [144]:

$$\eta = \frac{\Delta R_S^{E\neq 0}}{\Delta R_S^{E=0}} \approx \frac{e^{-\frac{L}{\lambda_{N,drift}}}}{e^{-\frac{L}{\lambda_N}}} \tag{4.38}$$

where $\Delta R_S^{E\neq 0}$ is the spin signal at finite electric fields, and $\Delta R_S^{E=0}$ is the spin signal expected from standard theory without electric field effects, which are measured by nonlocal 4T experiments. $\Delta V^{E=0} = \Delta V_{S,D}^{E=0} + \Delta V_{D,S}^{E=0}$, where $\Delta V_{S,D}^{E=0}$ and $\Delta V_{D,S}^{E=0}$ correspond to the voltage change at the source due to the spin accumulation generated at the drain, and the other way around.

By setting $\lambda_{N,drift} = \beta \times \lambda_N$, and extracting the parameter β, which represents the effective spin diffusion length change, we can calculate the enhancement. From my experimental data, $\eta = 2.1$ and $L = 0.87\ \mu m$, yield $\beta = 1.68$. Therefore, if spin drift effects are responsible for the observed 2T value, then $\lambda_{N,drift} = 1.68 \times \lambda_N$.

When the noise level of the measurements is not very high, and the amplitude of the spin signal is significant, DC 2T spin valve measurements were also performed. Figure 4.24 shows DC local 2T spin valve signals for a Si NW device with 2T resistance of $R_{2T} = 179.7\ k\Omega$. The signals show similar switching behavior as in the AC measurements when the antiparallel and parallel configurations are realized. The magnetic field sweeps were performed for two bias currents, $I = +50\ nA$ and $I = -50\ nA$. The spin signals for both bias currents are $\sim 40\ \mu V$, indicating that there is no asymmetry between positive and negative bias currents, as the theoretical model suggests (Equation 4.26). This is expected since the measurements are within the low bias regime, and hence bias dependence effects on spin polarization are not prominent.

4.2.5 3T Spin Valve Measurements

Finally, I also performed AC measurements in the local 3T scheme (Figure 4.25), where the current is applied similar to the 2T local scheme, but the voltage is measured between one of the electrodes and an electrode placed farther away in the channel outside the charge current path. In this type of measurement, we access the spin accumulation under one contact, which helps reducing the noise level compared to the local 2T configuration. Figures 4.25 (a) and (b) show the spin valve signals from two configurations, I2-3; V2-1 and I2-1; V2-3, respectively. The interface and channel parameters of the device are listed in Table 4.7 (same Si NW), and the 3T spin valve signals ΔR_S are listed in Table 4.8. The amplitudes of the spin signals for the same bias voltage $V_{bias} = 5\ mV$ are on average $\Delta V_{3T} = 2.98\ \mu V$ and $\Delta V_{3T} = 2.65\ \mu V$, respectively. The switching points for the antiparallel and parallel configurations for the black and red sweeps are $H = \pm 171\ Oe$ and $H = \pm 1912\ Oe$ for combination I2-3; V2-1, and $H = \pm 164\ Oe$ and $H = \pm 1986\ Oe$ for combination I2-1; V2-3. Once again, we notice that the switching fields are similar to the ones obtained from the NL-4T and local 2T measurements, which indicates that these signals originate from spin accumulation in the channel.

Furthermore, similar to the previous analysis, we can estimate the expected ratio of the spin signals between the two measurements with Equation 4.31, due to the fact that we use different segments of the NW for spin transport. The expected ratio based on the corresponding channel and junction parameters is $\Delta R_S^{3-2}/\Delta R_S^{2-1} = 2.48$. The experimental values (Table 4.8) give a ratio of $\Delta R_S^{3-2}/\Delta R_S^{2-1} = 2.25$, in good agreement with the theory. This further supports that the spin signal is due to the spin accumulation under contact #2.

Table 4.8: 3T spin valve results. The spin valve configuration indicates which electrode is used as the spin injector. The voltage bias for the spin injectors is also provided. $\Delta R_S = \Delta V/I$ is the spin accumulation signal under contact #2.

Sample	Spin valve configuration	$\Delta R_S(\Omega)$
Figure 4.25	I 2-3 ; V 2-1 $V = 5\ mV$	298
	I 2-1 ; V 2-3 $V = 5\ mV$	132

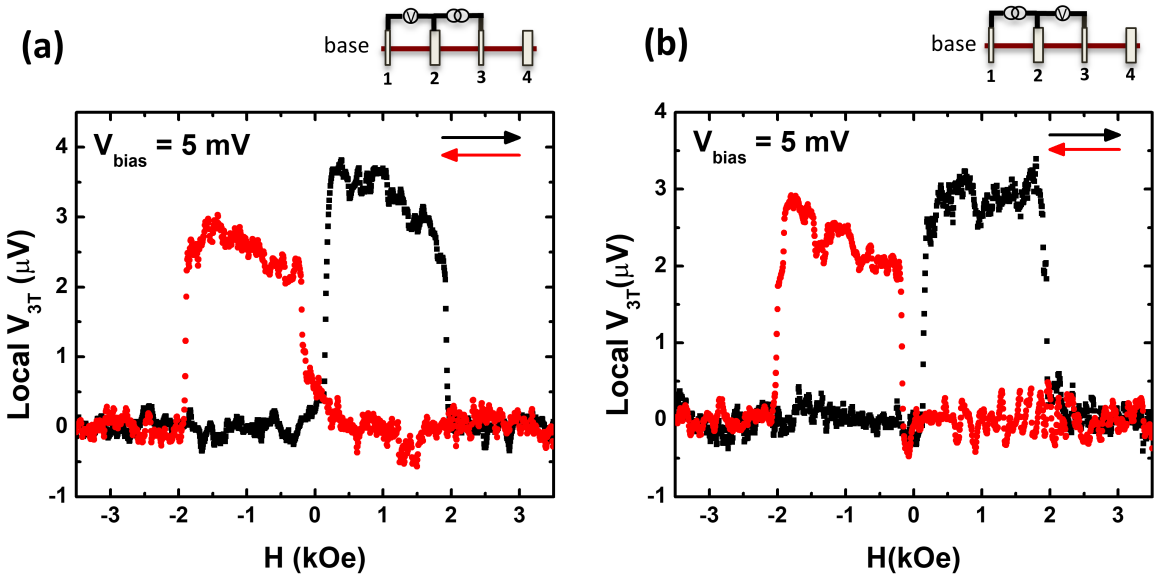

Figure 4.25: Local 3T spin valve signals for the same contact #2 with a junction resistance $R_2 = 15\ k\Omega$. (a) Spin signal measured from combination I2-3; V2-1, (b) Spin signal measured from combination I2-1; V2-3. The bias voltage for both measurements was $V_{bias} = 5\ mV$.

If we compare our 2T local spin valve signals with the ones extracted from the 3T local spin valves, we notice a difference in the magnitudes of the signals even though the same transport channel and the same bias current were used (the Si NW used is the same as in Figure 4.21). For example, the extracted magnitudes, for bias current $I = 10\ nA$, from Figure 4.21 (b) and Figure 4.25 (a) are 17.5 μV and 2.98 μV, respectively. While the 3T local scheme mostly detects the spin accumulation under one contact (#2), the 2T local measurement is obviously affected by the other contact (#3) and the spin drift effect.

CHAPTER 5

CONCLUSIONS

In this thesis, I have presented electrical spin transport measurements in a unique type of 1D spin transport media, Si NWs with a pronounced axial doping gradient. Specifically, I have performed 2T local and 4T nonlocal spin valve measurements, in an effort to systematically study the dependence of the spin polarization of the current on different interfacial properties on a single Si NW. From the acquired data and model analysis, a distinct correlation between the FM/Si NW junction resistance of the injector electrode and the spin polarization of the current was revealed. The explanation for the experimental observations is based on a picture of differently and oppositely spin polarized $3d$ and $4sp$ electron states contributing to the tunneling injection current, and how the different characteristic decay lengths of the two tunneling currents determine the total spin polarization of the injection current.

The observed correlation was possible due to the formation of different SBs along the length of a single Si NW. The unique structure of the Si NWs translates into a systematic variation of the FM/Si NW contacts of Schottky nano-junctions of different barrier width/height along the length of an individual Si NW. These devices are good candidates for studying the control of the interface spin polarization with different SB heights without having to use different FM materials of different work functions, which has been studied in FM/Si interfaces, or by using different oxide layer thicknesses as tunnel barriers. Fabricating many different replicas render the experimental results more difficult to interpret. Practically, our experiments on this device platform demonstrate that there is an optimal window of interface parameters for maximum spin injection efficiency and current spin polarization.

The results obtained in this thesis suggest new pathways for fabricating nanoscale spintronics devices, and specifically, how asymmetric interfaces can prove beneficial for maximizing spin injection/detection. In lateral spin valve devices the FM/SC interface can be tuned to provide optimum conditions for efficient spin injection. Non-symmetric interfaces could be beneficial, since by tuning

the FM/SC interfaces, devices with one tunnel junction (J_1) for high spin injection and one metallic junction (J_2) as a strong spin absorber could be realized.

The work required extensive use of the diverse set of tools and techniques often utilized in nanoscale device fabrication, and high sensitivity electrical/magnetic characterizations, including electron beam lithography, SEM, AFM, magnetron sputtering, AC lock-in amplifier technique.

Specifically, nonlocal 4T spin valve measurements were performed for different electrode configurations in order to examine the variation of the nonlocal spin signal upon i) interchange the injector and detector between adjacent FM/NW contacts of different properties, and ii) using a same FM/NW contact as the spin detector and the contact on either side as the spin injector. The spin signals were analyzed with a modified spin transport model, in which I introduced a phenomenological parameter α. The parameter α represents the dependence of the spin signals on the different interfacial properties due to the varying doping density at the FM/NW junctions. The experimental results reveal that α decreases monotonically with increasing junction resistance of the injector contact. The monotonic decay is attributed to the increased contribution of the $4sp$ electron states over the $3d$ electron states at increasing injector junction resistances due to the concurrent increase of the depletion layer width of the SBs. These results provide further insight into the mechanism and the origin of the spin polarization of the tunneling current in FM/SC Schottky junctions.

The local 2T spin valve measurements were performed for different electrode combinations, and they were compared with the nonlocal 4T measurements to provide additional insight about the spin injection process. The signals showed identical magnetic switching behavior and reasonable magnitude values, which indicates that the local 2T spin signals originate from spin accumulation in the Si NW channel, and are not due to other magnetoresistance effects. Direct comparison of the local 2T and nonlocal 4T spin signals in the Si NW devices showed that the 2T spin signals are larger than the nonlocal 4T spin signals for the same transport channel, which is not predicted by the original theoretical model. We ascribed this deviation to the electrical spin drift effect, which is present in the local measurement scheme, and has been previously observed in SC spin valve devices. In addition, by analyzing the data with a model that predicts enhancement of the effective spin diffusion length by spin drift, we determined that the enhancement factor is $n = 2.1$.

In addition, local 3T spin valve measurements and local 3T Hanle measurements were performed. The local 3T measurements measure spin accumulation directly under a single contact. By comparing them with the local 2T spin signals, which are larger in magnitude, we were able to observe how the electrical spin drift effect alters the spin transport process for the same transport channel. We were unable to obtain viable Hanle signals. We surmise that it is a consequence of the non-planar geometry of the FM electrodes covering the surface of the Si NWs, namely, the dome-shaped profile. The electrode geometry is responsible for the magnetization profile of the FM injector/detector. The dome-shaped profile results in more complicated and non-planar magnetization directions, and as a result the Hanle effect signals are hindered. A planarization process to form rectangular electrodes may resolve this issue.

Through this work, we have expanded on the knowledge and understanding of the importance of the FM/SC interface properties on spin injection/detection on nanoscale in spin valve experiments, and indicated the intriguing possibility of fabricating devices with asymmetric interfaces for potential spintronics applications. Sytematic studies will be continued on more samples with different growth parameters to control the doping gradient, and study whether the sign of the spin signal switches sign with the progressive increase of the $4sp$ electron states contribution. An optimized fabrication procedure (planarization process) to realize sharp switching will also be implemented.

BIBLIOGRAPHY

[1] W.H. Brattain and B. John. Three-electrode circuit element utilizing semiconductive materials, October 3 1950. US Patent 2,524,035.

[2] W. Shockley. Circuit element utilizing semiconductive material, September 25 1951. US Patent 2,569,347.

[3] J.S. Kilby. Miniaturized electronic circuits, June 23 1964. US Patent 3,138,743.

[4] K. Dawon. Electric field controlled semiconductor device, August 27 1963. US Patent 3,102,230.

[5] F.M. Wanlass. Low stand-by power complementary field effect circuitry, December 5 1967. US Patent 3,356,858.

[6] G. E. Moore. Cramming more components onto integrated circuits. *Electronics*, 38(8), 1965.

[7] HJ Zhu, M Ramsteiner, H Kostial, M Wassermeier, H-P Schönherr, and KH Ploog. Room-temperature spin injection from Fe into GaAs. *Physical Review Letters*, 87(1):016601, 2001.

[8] A. T. Hanbicki, B. T. Jonker, G. Itskos, G. Kioseoglou, and A. Petrou. Efficient electrical spin injection from a magnetic metal/tunnel barrier contact into a semiconductor. *Applied Physics Letters*, 80(7):1240–1242, 2002.

[9] Pol Van Dorpe, Willem Van Roy, VF Motsny, Gustaaf Borghs, and J De Boeck. Efficient electrical spin injection in GaAs: A comparison between AlO_x and Schottky injectors. *Journal of Vacuum Science & Technology A: Vacuum, Surfaces, and Films*, 22(4):1862–1867, 2004.

[10] Berend T. Jonker, George Kioseoglou, Aubrey T. Hanbicki, Connie H. Li, and Phillip E. Thompson. Electrical spin-injection into silicon from a ferromagnetic metal/tunnel barrier contact. *Nature Physics*, 3:542 EP –, Jul 2007.

[11] Xiaohua Lou, Christoph Adelmann, Scott A. Crooker, Eric S. Garlid, Jianjie Zhang, K. S. Madhukar Reddy, Soren D. Flexner, Chris J. Palmstrom, and Paul A. Crowell. Electrical detection of spin transport in lateral ferromagnet-semiconductor devices. *Nat Phys*, 3(3):197–202, 03 2007.

[12] Hyun Cheol Koo, Jae Hyun Kwon, Jonghwa Eom, Joonyeon Chang, Suk Hee Han, and Mark Johnson. Control of spin precession in a spin-injected field effect transistor. *Science*, 325(5947):1515–1518, 2009.

[13] Wei Han, Xin Jiang, Adam Kajdos, See-Hun Yang, Susanne Stemmer, and Stuart SP Parkin. Spin injection and detection in lanthanum-and niobium-doped $SrTiO_3$ using the Hanle technique. *Nature Communications*, 4:2134, 2013.

[14] M. Oltscher, M. Ciorga, M. Utz, D. Schuh, D. Bougeard, and D. Weiss. Electrical spin injection into high mobility 2D systems. *Phys. Rev. Lett.*, 113:236602, Dec 2014.

[15] Pojen Chuang, Sheng-Chin Ho, LW Smith, F Sfigakis, M Pepper, Chin-Hung Chen, Ju-Chun Fan, JP Griffiths, Ian Farrer, Harvey Edward Beere, et al. All-electric all-semiconductor spin field-effect transistors. *Nature Nanotechnology*, 10(1):35, 2015.

[16] Li-Te Chang, Inga Anita Fischer, Jianshi Tang, Chiu-Yen Wang, Guoqiang Yu, Yabin Fan, Koichi Murata, Tianxiao Nie, Michael Oehme, Jörg Schulze, et al. Electrical detection of spin transport in Si two-dimensional electron gas systems. *Nanotechnology*, 27(36):365701, 2016.

[17] En-Shao Liu, Junghyo Nah, Kamran M Varahramyan, and Emanuel Tutuc. Lateral spin injection in germanium nanowires. *Nano letters*, 10(9):3297–3301, 2010.

[18] Jean Tarun, Shaoyun Huang, Yasuhiro Fukuma, Hiroshi Idzuchi, YoshiChika Otani, Naoki Fukata, Koji Ishibashi, and Shunri Oda. Demonstration of spin valve effects in silicon nanowires. *Journal of Applied Physics*, 109(7):07C508, 2011.

[19] S. Heedt, C. Morgan, K. Weis, D. E. Bürgler, R. Calarco, H. Hardtdegen, D. Grützmacher, and Th. Schäpers. Electrical spin injection into InN semiconductor nanowires. *Nano Letters*, 12(9):4437–4443, 2012. PMID: 22889199.

[20] Shixiong Zhang, Shadi A. Dayeh, Yan Li, Scott A. Crooker, Darryl L. Smith, and S. T. Picraux. Electrical spin injection and detection in silicon nanowires through oxide tunnel barriers. *Nano Letters*, 13(2):430–435, 2013. PMID: 23324028.

[21] Jianshi Tang, Chiu-Yen Wang, Li-Te Chang, Yabin Fan, Tianxiao Nie, Michael Chan, Wanjun Jiang, Yu-Ting Chen, Hong-Jie Yang, Hsing-Yu Tuan, Lih-Juann Chen, and Kang L. Wang. Electrical spin injection and detection in Mn_5Ge_3/Ge/Mn_5Ge_3 nanowire transistors. *Nano Letters*, 13(9):4036–4043, 2013. PMID: 23937588.

[22] O. M. J. van 't Erve, A. L. Friedman, C. H. Li, J. T. Robinson, J. Connell, L. J. Lauhon, and B. T. Jonker. Spin transport and hanle effect in silicon nanowires using graphene tunnel barriers. 6:7541 EP –, 06 2015.

[23] G. Schmidt, D. Ferrand, L. W. Molenkamp, A. T. Filip, and B. J. van Wees. Fundamental obstacle for electrical spin injection from a ferromagnetic metal into a diffusive semiconductor. *Phys. Rev. B*, 62:R4790–R4793, Aug 2000.

[24] A. Fert and H. Jaffrès. Conditions for efficient spin injection from a ferromagnetic metal into a semiconductor. *Phys. Rev. B*, 64:184420, Oct 2001.

[25] Byoung-Chul Min, Kazunari Motohashi, Cock Lodder, and Ron Jansen. Tunable spin-tunnel contacts to silicon using low-work-function ferromagnets. *Nat Mater*, 5(10):817–822, 10 2006.

[26] Y Lu, VG Truong, P Renucci, M Tran, H Jaffrès, C Deranlot, J-M George, A Lemaître, Y Zheng, D Demaille, et al. MgO thickness dependence of spin injection efficiency in spin-light emitting diodes. *Applied Physics Letters*, 93(15):152102, 2008.

[27] F. J. Jedema, A. T. Filip, and B. J. van Wees. Electrical spin injection and accumulation at room temperature in an all-metal mesoscopic spin valve. *Nature*, 410(6826):345–348, 03 2001.

[28] Tomoyuki Sasaki, Yuichiro Ando, Makoto Kameno, Takayuki Tahara, Hayato Koike, Tohru Oikawa, Toshio Suzuki, and Masashi Shiraishi. Spin transport in nondegenerate Si with a spin MOSFET structure at room temperature. *Phys. Rev. Applied*, 2:034005, Sep 2014.

[29] M. N. Baibich, J. M. Broto, A. Fert, F. Nguyen Van Dau, F. Petroff, P. Etienne, G. Creuzet, A. Friederich, and J. Chazelas. Giant magnetoresistance of (001)Fe/(001)Cr magnetic superlattices. *Phys. Rev. Lett.*, 61:2472–2475, Nov 1988.

[30] G. Binasch, P. Grünberg, F. Saurenbach, and W. Zinn. Enhanced magnetoresistance in layered magnetic structures with antiferromagnetic interlayer exchange. *Phys. Rev. B*, 39:4828–4830, Mar 1989.

[31] Supriyo Datta and Biswajit Das. Electronic analog of the electrooptic modulator. *Applied Physics Letters*, 56(7):665–667, 1990.

[32] Satoshi Sugahara and Masaaki Tanaka. A spin metal-oxide-semiconductor field-effect transistor (spin MOSFET) with a ferromagnetic semiconductor for the channel. *Journal of Applied Physics*, 97(10):10D503, 2005.

[33] M.I. Dyakonov and V.I. Perel. Current-induced spin orientation of electrons in semiconductors. *Physics Letters A*, 35(6):459 – 460, 1971.

[34] Y. K. Kato, R. C. Myers, A. C. Gossard, and D. D. Awschalom. Observation of the spin Hall effect in semiconductors. *Science*, 306(5703):1910–1913, 2004.

[35] Joerg Wunderlich, Bernd Kaestner, Jairo Sinova, and Tomas Jungwirth. Experimental observation of the spin-Hall effect in a two-dimensional spin-orbit coupled semiconductor system. *Physical Review Letters*, 94(4):047204, 2005.

[36] S. D. Ganichev, E. L. Ivchenko, V. V. Bel'kov, S. A. Tarasenko, M. Sollinger, D. Weiss, W. Wegscheider, and W. Prettl. Spin-galvanic effect. *Nature*, 417:153 EP –, May 2002.

[37] Jairo Sinova, Sergio O Valenzuela, J Wunderlich, CH Back, and T Jungwirth. Spin Hall effects. *Reviews of Modern Physics*, 87(4):1213, 2015.

[38] S D Ganichev and W Prettl. Spin photocurrents in quantum wells. *Journal of Physics: Condensed Matter*, 15(20):R935, 2003.

[39] H. Ohno. Making nonmagnetic semiconductors ferromagnetic. *Science*, 281(5379):951–956, 1998.

[40] H. Ohno, N. Akiba, F. Matsukura, A. Shen, K. Ohtani, and Y. Ohno. Spontaneous splitting of ferromagnetic (Ga, Mn)As valence band observed by resonant tunneling spectroscopy. *Applied Physics Letters*, 73(3):363–365, 1998.

[41] Robert Meservey and PM Tedrow. Spin-polarized electron tunneling. *Physics Reports*, 238(4):173–243, 1994.

[42] Nevill Francis Mott. The electrical conductivity of transition metals. *Proceedings of the Royal Society of London A: Mathematical, Physical and Engineering Sciences*, 153(880):699–717, 1936.

[43] Georges Lampel. Nuclear dynamic polarization by optical electronic saturation and optical pumping in semiconductors. *Phys. Rev. Lett.*, 20:491–493, Mar 1968.

[44] J. M. Kikkawa and D. D. Awschalom. Resonant spin amplification in n-type GaAs. *Phys. Rev. Lett.*, 80:4313–4316, May 1998.

[45] E. Saitoh, M. Ueda, H. Miyajima, and G. Tatara. Conversion of spin current into charge current at room temperature: Inverse spin-Hall effect. *Applied Physics Letters*, 88(18):182509, 2006.

[46] G. Binasch, P. Grünberg, F. Saurenbach, and W. Zinn. Enhanced magnetoresistance in layered magnetic structures with antiferromagnetic interlayer exchange. *Phys. Rev. B*, 39:4828–4830, Mar 1989.

[47] B. Dieny, V. S. Speriosu, S. S. P. Parkin, B. A. Gurney, D. R. Wilhoit, and D. Mauri. Giant magnetoresistive in soft ferromagnetic multilayers. *Phys. Rev. B*, 43:1297–1300, Jan 1991.

[48] Bernard Dieny, Bruce A Gurney, Serhat Metin, Stuart SP Parkin, and Virgil S Speriosu. Magnetoresistive sensor based on the spin valve effect, October 27 1992. US Patent 5,159,513.

[49] J. S. Moodera, Lisa R. Kinder, Terrilyn M. Wong, and R. Meservey. Large magnetoresistance at room temperature in ferromagnetic thin film tunnel junctions. *Phys. Rev. Lett.*, 74:3273–3276, Apr 1995.

[50] T. Miyazaki and N. Tezuka. Giant magnetic tunneling effect in $Fe/Al_2O_3/Fe$ junction. *Journal of Magnetism and Magnetic Materials*, 139(3):L231 – L234, 1995.

[51] Stuart S. P. Parkin, Christian Kaiser, Alex Panchula, Philip M. Rice, Brian Hughes, Mahesh Samant, and See-Hun Yang. Giant tunnelling magnetoresistance at room temperature with MgO (100) tunnel barriers. *Nature Materials*, 3:862 EP –, Oct 2004.

[52] Claude Chappert, Albert Fert, and Frédéric Nguyen Van Dau. The emergence of spin electronics in data storage. *Nature Materials*, 6:813 EP –, Nov 2007. Review Article.

[53] Mark Johnson and R. H. Silsbee. Interfacial charge-spin coupling: Injection and detection of spin magnetization in metals. *Phys. Rev. Lett.*, 55:1790–1793, Oct 1985.

[54] Mark Johnson and R. H. Silsbee. Spin-injection experiment. *Phys. Rev. B*, 37:5326–5335, Apr 1988.

[55] A.G. Aronov. Spin waves in a medium with nonequilibrium spin orientation. *Sov. Phys. Semicond*, 10:698, 1976.

[56] S. J. van der Molen, N. Tombros, and B. J. van Wees. Magneto − Coulomb effect in spin-valve devices. *Phys. Rev. B*, 73:220406, Jun 2006.

[57] F.G. Monzon, D.S. Patterson, and M.L. Roukes. Characterization of individual nanomagnets by the local Hall effect. *Journal of Magnetism and Magnetic Materials*, 195(1):19 – 25, 1999.

[58] Michel I Dyakonov and AV Khaetskii. *Spin physics in semiconductors*, volume 1. Springer, 2008.

[59] Mark Johnson. Spin polarization of gold films via transported (invited). *Journal of Applied Physics*, 75(10):6714–6719, 1994.

[60] Jaroslav Fabian, Alex Matos-Abiague, Christian Ertler, Peter Stano, and Igor Zutic. Semiconductor spintronics. *Acta Phys. Slovaca*, 57(4-5):565, 2007.

[61] P. R. Hammar, B. R. Bennett, M. J. Yang, and Mark Johnson. Observation of spin injection at a ferromagnet-semiconductor interface. *Phys. Rev. Lett.*, 83:203–206, Jul 1999.

[62] E. I. Rashba. Theory of electrical spin injection: Tunnel contacts as a solution of the conductivity mismatch problem. *Phys. Rev. B*, 62:R16267–R16270, Dec 2000.

[63] D. L. Smith and R. N. Silver. Electrical spin injection into semiconductors. *Phys. Rev. B*, 64:045323, Jul 2001.

[64] A. Fert, J. M. George, H. Jaffres, and R. Mattana. Semiconductors between spin-polarized sources and drains. *IEEE Transactions on Electron Devices*, 54(5):921–932, May 2007.

[65] Yunong Qi, D. Y. Xing, and Jinming Dong. Relation between Julliere and Slonczewski models of tunneling magnetoresistance. *Phys. Rev. B*, 58:2783–2787, Aug 1998.

[66] V. F. Motsnyi, J. De Boeck, J. Das, W. Van Roy, G. Borghs, E. Goovaerts, and V. I. Safarov. Electrical spin injection in a ferromagnet/tunnel barrier/semiconductor heterostructure. *Applied Physics Letters*, 81(2):265–267, 2002.

[67] Saroj P. Dash, Sandeep Sharma, Ram S. Patel, Michel P. de Jong, and Ron Jansen. Electrical creation of spin polarization in silicon at room temperature. *Nature*, 462(7272):491–494, 11 2009.

[68] Tomoyuki Sasaki, Tohru Oikawa, Toshio Suzuki, Masashi Shiraishi, Yoshishige Suzuki, and Katsumichi Tagami. Electrical spin injection into silicon using MgO tunnel barrier. *Applied Physics Express*, 2(5):053003, 2009.

[69] Klaus H. Ploog. Spin injection in ferromagnet-semiconductor heterostructures at room temperature (invited). *Journal of Applied Physics*, 91(10):7256–7260, 2002.

[70] S. A. Crooker, M. Furis, X. Lou, C. Adelmann, D. L. Smith, C. J. Palmstrøm, and P. A. Crowell. Imaging spin transport in lateral ferromagnet/semiconductor structures. *Science*, 309(5744):2191–2195, 2005.

[71] C. Adelmann, X. Lou, J. Strand, C. J. Palmstrøm, and P. A. Crowell. Spin injection and relaxation in ferromagnet-semiconductor heterostructures. *Phys. Rev. B*, 71:121301, Mar 2005.

[72] O. M. J. van 't Erve, A. L. Friedman, E. Cobas, C. H. Li, J. T. Robinson, and B. T. Jonker. Low-resistance spin injection into silicon using graphene tunnel barriers. *Nature Nanotechnology*, 7:737 EP –, Sep 2012. Article.

[73] Y.A. Bychkov and E.I Rashba. Properties of a 2D electron gas with lifted spectral degeneracy. *Journal of Experimental and Theoretical Physics Letters*, 39:78, 1984.

[74] G. Dresselhaus. Spin-orbit coupling effects in zinc blende structures. *Phys. Rev.*, 100:580–586, Oct 1955.

[75] S. D. Ganichev, V. V. Bel'kov, L. E. Golub, E. L. Ivchenko, Petra Schneider, S. Giglberger, J. Eroms, J. De Boeck, G. Borghs, W. Wegscheider, D. Weiss, and W. Prettl. Experimental separation of Rashba and Dresselhaus spin splittings in semiconductor quantum wells. *Phys. Rev. Lett.*, 92:256601, Jun 2004.

[76] R. J. Elliott. Theory of the effect of spin-orbit coupling on magnetic resonance in some semiconductors. *Phys. Rev.*, 96:266–279, Oct 1954.

[77] Y. Yafet. g factors and spin-lattice relaxation of conduction electrons. *Solid State Physics*, 14, Academic Press, New York, 1963.

[78] Perel V.I D'yakonov, M.I. Spin orientation of electrons associated with the interband absorption of light in semiconductors. *Zh. Eksp. Teor. Fiz.*, 33:1053, 1971.

[79] G.L. Bir, A.G. Aronov, and G.E. Pikus. Spin relaxation of electrons due to scattering by holes. *Journal of Experimental and Theoretical Physics*, 42:705, 1975.

[80] J. Shiogai, M. Ciorga, M. Utz, D. Schuh, T. Arakawa, M. Kohda, K. Kobayashi, T. Ono, W. Wegscheider, D. Weiss, and J. Nitta. Dynamic nuclear spin polarization in an all-semiconductor spin injection device with $(Ga, Mn)As/n - GaAs$ spin Esaki diode. *Applied Physics Letters*, 101(21):212402, 2012.

[81] K. V. Kavokin. Anisotropic exchange interaction of localized conduction-band electrons in semiconductors. *Phys. Rev. B*, 64:075305, Jul 2001.

[82] Ian Appelbaum, Biqin Huang, and Douwe J. Monsma. Electronic measurement and control of spin transport in silicon. *Nature*, 447(7142):295–298, 05 2007.

[83] G. Kioseoglou, A. T. Hanbicki, R. Goswami, O. M. J. van t Erve, C. H. Li, G. Spanos, P. E. Thompson, and B. T. Jonker. Electrical spin injection into Si: A comparison between Fe/Si Schottky and Fe/Al_2O_3 tunnel contacts. *Applied Physics Letters*, 94(12):122106, 2009.

[84] A. A. Kiselev and K. W. Kim. Progressive suppression of spin relaxation in two-dimensional channels of finite width. *Phys. Rev. B*, 61:13115–13120, May 2000.

[85] A. G. Mal'shukov and K. A. Chao. Waveguide diffusion modes and slowdown of $D'yakonov - Perel'$ spin relaxation in narrow two-dimensional semiconductor channels. *Phys. Rev. B*, 61:R2413–R2416, Jan 2000.

[86] A. W. Holleitner, V. Sih, R. C. Myers, A. C. Gossard, and D. D. Awschalom. Suppression of spin relaxation in submicron InGaAs wires. *Phys. Rev. Lett.*, 97:036805, Jul 2006.

[87] Ashish Kumar, Md Akram, Satya Gopal Dinda, Bahniman Ghosh, et al. Spin relaxation in silicon nanowires. *Journal of Computational and Theoretical Nanoscience*, 9(12):2068–2073, 2012.

[88] Antoine Lavoisier, Jöns Jacob Berzelius, and Thomas Thomson. Silicon history. *History*, 2(8):4.

[89] Simon M Sze and Kwok K Ng. *Physics of semiconductor devices*. John wiley & sons, 2006.

[90] RI Dzhioev, KV Kavokin, VL Korenev, MV Lazarev, B Ya Meltser, MN Stepanova, BP Zakharchenya, D Gammon, and DS Katzer. Low-temperature spin relaxation in n-type GaAs. *Physical Review B*, 66(24):245204, 2002.

[91] X Lou, C Adelmann, M Furis, SA Crooker, CJ Palmstrøm, and PA Crowell. Electrical detection of spin accumulation at a ferromagnet-semiconductor interface. *Physical review letters*, 96(17):176603, 2006.

[92] R. S. Wagner and W. C. Ellis. Vaporliquidsolid mechanism of single crystal growth. *Applied Physics Letters*, 4(5):89–90, 1964.

[93] Gyu-Chul Yi. *Semiconductor nanostructures for optoelectronic devices: Processing, characterization and applications*. Springer Science & Business Media, 2012.

[94] Teng Liu, Richard Liang, Okenwa Okoli, and Mei Zhang. Fabrication of silicon nanowire on freestanding multiwalled carbon nanotubes by chemical vapor deposition. *Materials Letters*, 159:353 – 356, 2015.

[95] Daniel E. Perea, Eric R. Hemesath, Edwin J. Schwalbach, Jessica L. Lensch-Falk, Peter W. Voorhees, and Lincoln J. Lauhon. Direct measurement of dopant distribution in an individual vapour-liquid-solid nanowire. *Nature Nanotechnology*, 4(5):315–319, 05 2009.

[96] Ruth A. Schlitz, Daniel E. Perea, Jessica L. Lensch-Falk, Eric R. Hemesath, and Lincoln J. Lauhon. Correlating dopant distributions and electrical properties of boron-doped silicon nanowires. *Applied Physics Letters*, 95(16):162101, 2009.

[97] Robert C O'Handley. *Modern magnetic materials: principles and applications*. Wiley, 2000.

[98] Jun Yu, Ulrich Rüdiger, Luc Thomas, Stuart SP Parkin, and Andrew D Kent. Micromagnetics of mesoscopic epitaxial (110) Fe elements with nanoshaped ends. *Journal of Applied Physics*, 85(8):5501–5503, 1999.

[99] J Aumentado and V Chandrasekhar. Magnetoresistance of single-domain ferromagnetic particles. *Applied Physics Letters*, 74(13):1898–1900, 1999.

[100] Yung-Chen Lin, Yu Chen, Alexandros Shailos, and Yu Huang. Detection of spin polarized carrier in silicon nanowire with single crystal mnsi as magnetic contacts. *Nano Letters*, 10(6):2281–2287, 2010. PMID: 20499889.

[101] A. T. Hanbicki, O. M. J. van 't Erve, R. Magno, G. Kioseoglou, C. H. Li, B. T. Jonker, G. Itskos, R. Mallory, M. Yasar, and A. Petrou. Analysis of the transport process providing spin injection through an Fe/AlGaAs Schottky barrier. *Applied Physics Letters*, 82(23):4092–4094, 2003.

[102] Oihana Txoperena, Yang Song, Lan Qing, Marco Gobbi, Luis E. Hueso, Hanan Dery, and Fèlix Casanova. Impurity-assisted tunneling magnetoresistance under a weak magnetic field. *Phys. Rev. Lett.*, 113:146601, Oct 2014.

[103] F Léonard, AA Talin, A Katzenmeyer, BS Swartzentruber, ST Picraux, E Toimil-Molares, JG Cederberg, X Wang, SD Hersee, and A Rishinaramangalum. Electronic transport in nanowires: from injection-limited to space-charge-limited behavior. In *Nanoepitaxy: Homo- and Heterogeneous Synthesis, Characterization, and Device Integration of Nanomaterials*, volume 7406, page 74060G. International Society for Optics and Photonics, 2009.

[104] François Léonard and A Alec Talin. Electrical contacts to one-and two-dimensional nanomaterials. *Nature Nanotechnology*, 6(12):773, 2011.

[105] Zhihong Chen, Joerg Appenzeller, Joachim Knoch, Yu-ming Lin, and Phaedon Avouris. The role of metal- nanotube contact in the performance of carbon nanotube field-effect transistors. *Nano Letters*, 5(7):1497–1502, 2005.

[106] Raymond T Tung. Recent advances in Schottky barrier concepts. *Materials Science and Engineering: R: Reports*, 35(1-3):1–138, 2001.

[107] AM Rodrigues. Extraction of Schottky diode parameters from current-voltage data for a chemical-vapor-deposited diamond/silicon structure over a wide temperature range. *Journal of Applied Physics*, 103(8):083708, 2008.

[108] Jorge L. Barreda, Timothy D. Keiper, Mei Zhang, and Peng Xiong. Multiple Schottky barrier-limited field-effect transistors on a single silicon nanowire with an intrinsic doping gradient. *ACS Applied Materials & Interfaces*, 9(13):12046–12053, 2017. PMID: 28274114.

[109] Athanasios N Chantis and Darryl L Smith. Theory of electrical spin-detection at a ferromagnet/semiconductor interface. *Physical Review B*, 78(23):235317, 2008.

[110] S. A. Crooker, E. S. Garlid, A. N. Chantis, D. L. Smith, K. S. M. Reddy, Q. O. Hu, T. Kondo, C. J. Palmstrøm, and P. A. Crowell. Bias-controlled sensitivity of ferromagnet/semiconductor electrical spin detectors. *Phys. Rev. B*, 80:041305, Jul 2009.

[111] Junichi Shiogai, Mariusz Ciorga, Martin Utz, Dieter Schuh, Makoto Kohda, Dominique Bougeard, Tsutomu Nojima, Junsaku Nitta, and Dieter Weiss. Giant enhancement of spin detection sensitivity in (Ga, Mn) As/GaAs Esaki diodes. *Physical Review B*, 89(8):081307, 2014.

[112] TA Peterson, SJ Patel, CC Geppert, KD Christie, A Rath, D Pennachio, ME Flatté, PM Voyles, CJ Palmstrøm, and PA Crowell. Spin injection and detection up to room temperature in Heusler alloy/n-GaAs spin valves. *Physical Review B*, 94(23):235309, 2016.

[113] SJ Van Der Molen, N Tombros, and BJ Van Wees. Magneto-Coulomb effect in spin-valve devices. *Physical Review B*, 73(22):220406, 2006.

[114] David D Awschalom and Nitin Samarth. Optical manipulation, transport and storage of spin coherence in semiconductors. In *Semiconductor Spintronics and Quantum Computation*, pages 147–193. Springer, 2002.

[115] M Zaffalon and BJ Van Wees. Zero-dimensional spin accumulation and spin dynamics in a mesoscopic metal island. *Physical Review Letters*, 91(18):186601, 2003.

[116] T Kimura, J Hamrle, and Y Otani. Estimation of spin-diffusion length from the magnitude of spin-current absorption: Multiterminal ferromagnetic/nonferromagnetic hybrid structures. *Physical Review B*, 72(1):014461, 2005.

[117] Nikolaos Tombros, Csaba Jozsa, Mihaita Popinciuc, Harry T Jonkman, and Bart J Van Wees. Electronic spin transport and spin precession in single graphene layers at room temperature. *Nature*, 448(7153):571, 2007.

[118] M Furis, DL Smith, S Kos, ES Garlid, KSM Reddy, CJ Palmstrøm, PA Crowell, and SA Crooker. Local hanle-effect studies of spin drift and diffusion in n: GaAs epilayers and spin-transport devices. *New Journal of Physics*, 9(9):347, 2007.

[119] Joon-Ill Kim. *Spin Transport and Nanomagnetism in Semiconductor Heterostructures*. PhD thesis, Florida State University, 2016.

[120] Jennifer Misuraca, Joon-Il Kim, Jun Lu, Kangkang Meng, Lin Chen, Xuezhe Yu, Jianhua Zhao, Peng Xiong, and Stephan von Molnár. Bias current dependence of the spin lifetime in insulating $Al_{0.3}Ga_{0.7}As$. *Applied Physics Letters*, 104(8):082405, 2014.

[121] S Takahashi and S Maekawa. Spin injection and detection in magnetic nanostructures. *Physical Review B*, 67(5):052409, 2003.

[122] Saburo Takahashi and Sadamichi Maekawa. Spin current, spin accumulation and spin Hall effect. *Science and Technology of Advanced Materials*, 9(1):014105, 2008.

[123] T Kimura, J Hamrle, Y Otani, K Tsukagoshi, and Y Aoyagi. Effect of probe configuration on spin accumulation in lateral spin-valve structure. *Journal of Magnetism and Magnetic Materials*, 286:88–90, 2005.

[124] A. Einwanger, M. Ciorga, U. Wurstbauer, D. Schuh, W. Wegscheider, and D. Weiss. Tunneling anisotropic spin polarization in lateral $(Ga, Mn)As/GaAs$ spin Esaki diode devices. *Applied Physics Letters*, 95(15):152101, 2009.

[125] Ron Jansen. Silicon spintronics. *Nature Materials*, 11(5):400–408, 05 2012.

[126] Kun-Rok Jeon, Byoung-Chul Min, Il-Jae Shin, Chang-Yup Park, Hun-Sung Lee, Young-Hun Jo, and Sung-Chul Shin. Electrical spin accumulation with improved bias voltage dependence in a crystalline CoFe/MgO/Si system. *Applied Physics Letters*, 98(26):262102, 2011.

[127] S. O. Valenzuela, D. J. Monsma, C. M. Marcus, V. Narayanamurti, and M. Tinkham. Spin polarized tunneling at finite bias. *Phys. Rev. Lett.*, 94:196601, May 2005.

[128] BG Park, Tamalika Banerjee, JC Lodder, and Ritsert Jansen. Tunnel spin polarization versus energy for clean and doped Al_2O_3 barriers. *Physical Review Letters*, 99(21):217206, 2007.

[129] Y Ando, K Kasahara, K Yamane, Y Baba, Y Maeda, Y Hoshi, K Sawano, M Miyao, and K Hamaya. Bias current dependence of spin accumulation signals in a silicon channel detected by a Schottky tunnel contact. *Applied Physics Letters*, 99(1):012113, 2011.

[130] H. Jaffrès, J.-M. George, and A. Fert. Spin transport in multiterminal devices: Large spin signals in devices with confined geometry. *Phys. Rev. B*, 82:140408, Oct 2010.

[131] RJ Soulen, JM Byers, MS Osofsky, B Nadgorny, T Ambrose, SF Cheng, Pr R Broussard, CT Tanaka, J Nowak, JS Moodera, et al. Measuring the spin polarization of a metal with a superconducting point contact. *Science*, 282(5386):85–88, 1998.

[132] Jonathan E. Allen, Daniel E. Perea, Eric R. Hemesath, and Lincoln J. Lauhon. Nonuniform nanowire doping profiles revealed by quantitative scanning photocurrent microscopy. *Advanced Materials*, 21(30):3067–3072, 2009.

[133] DL Smith and PP Ruden. Spin-polarized tunneling through potential barriers at ferromagnetic metal/semiconductor Schottky contacts. *Physical Review B*, 78(12):125202, 2008.

[134] S Honda, H Itoh, J Inoue, H Kurebayashi, T Trypiniotis, CHW Barnes, A Hirohata, and JAC Bland. Spin polarization control through resonant states in an Fe/GaAs Schottky barrier. *Physical Review B*, 78(24):245316, 2008.

[135] Jagadeesh S Moodera and George Mathon. Spin polarized tunneling in ferromagnetic junctions. *Journal of Magnetism and Magnetic Materials*, 200(1-3):248–273, 1999.

[136] DJ Monsma and SSP Parkin. Spin polarization of tunneling current from ferromagnet/Al_2O_3 interfaces using copper-doped aluminum superconducting films. *Applied Physics Letters*, 77(5):720–722, 2000.

[137] II Mazin. How to define and calculate the degree of spin polarization in ferromagnets. *Physical Review Letters*, 83(7):1427, 1999.

[138] Mary Beth Stearns. Simple explanation of tunneling spin-polarization of Fe, Co, Ni and its alloys. *Journal of Magnetism and Magnetic Materials*, 5(2):167–171, 1977.

[139] SF Alvarado. Tunneling potential barrier dependence of electron spin polarization. *Physical Review Letters*, 75(3):513, 1995.

[140] M Münzenberg and JS Moodera. Superconductor-ferromagnet tunneling measurements indicate s p-spin and d-spin currents. *Physical Review B*, 70(6):060402, 2004.

[141] Alpha T N'diaye and Adrian Quesada. Spin-polarized low-energy electron microscopy (SPLEEM). *Characterization of Materials*, 2012.

[142] F. J. Jedema, M. S. Nijboer, A. T. Filip, and B. J. van Wees. Spin injection and spin accumulation in all-metal mesoscopic spin valves. *Phys. Rev. B*, 67:085319, Feb 2003.

[143] P Laczkowski, L Vila, V-D Nguyen, A Marty, J-P Attané, H Jaffrès, J-M George, and A Fert. Enhancement of the spin signal in permalloy/gold multiterminal nanodevices by lateral confinement. *Physical Review B*, 85(22):220404, 2012.

[144] Martin Oltscher, Franz Eberle, Thomas Kuczmik, Andreas Bayer, Dieter Schuh, Dominique Bougeard, Mariusz Ciorga, and Dieter Weiss. Gate-tunable large magnetoresistance in an all-semiconductor spin valve device. *Nature Communications*, 8(1):1807, 2017.

[145] Takayuki Tahara, Yuichiro Ando, Makoto Kameno, Hayato Koike, Kazuhito Tanaka, Shinji Miwa, Yoshishige Suzuki, Tomoyuki Sasaki, Tohru Oikawa, and Masashi Shiraishi. Observation of large spin accumulation voltages in nondegenerate Si spin devices due to spin drift effect: Experiments and theory. *Phys. Rev. B*, 93:214406, Jun 2016.

BIOGRAPHICAL SKETCH

Education

2013-2018: Ph. D. Physics, Florida State University

2011-2013: M. S. Physics, Florida State University

2005-2011: B. S. Physics, National and Kapodistrian University of Athens

Professional Experience

2012-2018: Graduate Research Assistant, Department of Physics, Florida State University

2011-2012: Teaching Assistant, Department of Physics, Florida State University

2005-2011: B. S. Physics, National and Kapodistrian University of Athens

Membership and Awards

American Physical Society (2012 - present)

Yung Li Wang Award, Florida State University (2018)

Novotny Graduate Award Fellowship, Florida State University (2016)

Presentations

Konstantinos Kountouriotis, J. Barreda, T. Keiper, M. Zhang, P. Xiong. "Systematic study of spin transport in Si nanowires with axial doping gradient in lateral spin valve configurations", Spin-TECH IX 2017, Fukuoka, Japan

Konstantinos Kountouriotis, J. Barreda, T. Keiper, M. Zhang, P. Xiong. "Systematic study of spin transport in Si nanowires with axial doping gradient", APS March Meeting 2017, New Orleans, LA

Konstantinos Kountouriotis, J. Barreda, T. Keiper, M. Zhang, P. Xiong. "Electrical spin injection and detection in Si nanowires with axial doping gradient", APS March Meeting 2016, Baltimore, MD

Publications

Konstantinos Kountouriotis, J. Barreda, T. Keiper, M. Zhang, P. Xiong. "Electrical spin injection and detection in silicon nanowires with axial doping gradient" (submitted)

Joon-Il Kim, K. Kountouriotis, T. Liu, S. von Molnar, P. Xiong, J. Lu, X.Z. Yu, J. H. Zhao. "Comparison of 3T and 4T Hanle measurements of spin accumulation in the persistent photoconductor $Al_{0.3}Ga_{0.7}As : Si$ (in preparation)

Zhao Yuan, C.Zhou, Y. Tian, Y. Shu, J. Messier, J.C. Wang, L.J. van de Burgt, K. Kountouriotis, Y. Xin, E. Holt, K. Schanze, R. Clark, T. Siegrist, B. Ma. "One-dimensional organic lead halide perovskites with efficient bluish white-light emission", Nat. Commun., **8**, 14051 (2017)